

High Temperature High Bandwidth Fiber Optic Pressure Sensors

Juncheng Xu

Dissertation submitted to the Faculty of
Virginia Polytechnic Institute and State University
in partial fulfillment of the requirements for the degree of

Doctor of Philosophy
In
Electrical Engineering

Advisory Committee

Anbo Wang, Chair

Ira Jacobs

Ahmad Safaai-Jazi

Yilu Liu

Gary R. Pickrell

Guy J Indebetouw

December 15th, 2005

Blacksburg, Virginia

Key words: diaphragm, dynamic pressure, Fabry-Perot, high temperature, optical fiber,
pressure sensor, acoustic sensor, fused silica

High Temperature High Bandwidth Fiber Optic Pressure Sensors

Juncheng Xu

(Abstract)

Pressure measurements are required in various industrial applications, including extremely harsh environments such as turbine engines, power plants and material-processing systems. Conventional sensors are often difficult to apply due to the high temperatures, highly corrosive agents or electromagnetic interference (EMI) noise that may be present in those environments. Fiber optic pressure sensors have been developed for years and proved themselves successfully in such harsh environments. Especially, diaphragm based fiber optic pressure sensors have been shown to possess advantages of high sensitivity, wide bandwidth, high operation temperature, immunity to EMI, lightweight and long life.

Static and dynamic pressure measurements at various locations of a gas turbine engine are highly desirable to improve its operation and reliability. However, the operating environment, in which temperatures may exceed 600 °C and pressures may reach 100 psi (690 kPa) with about 1 psi (6.9kPa) variation, is a great challenge to currently available sensors. To meet these requirements, a novel type of fiber optic engine pressure sensor has been developed. This pressure sensor functions as a diaphragm based extrinsic Fabry-Pérot interferometric sensor. One of the unique features of this sensor is the all silica structure, allowing a much higher operating temperature to be achieved with an extremely low temperature dependence. In addition, the flexible nature of the sensor design such as wide sensitivity selection, and passive or adaptive temperature compensation, makes the sensor suitable for a variety of applications

An automatically controlled CO₂ laser-based sensor fabrication system was developed and implemented. Several novel bonding methods were proposed and investigated to improve the sensor mechanical ruggedness and reduce its temperature dependence.

An engine sensor testing system was designed and instrumented. The system generates known static and dynamic pressures in a temperature-controlled environment, which was used to calibrate the sensor.

Several sensor signal demodulation schemes were used for different testing purposes including a white-light interferometry system, a tunable laser based component test system (CTS), and a self-calibrated interferometric-intensity based (SCIIB) system. All of these sensor systems are immune to light source power fluctuations, which offer high reliability and stability.

The fiber optic pressure sensor was tested in a F-109 turbofan engine. The testing results prove the sensor performance and the packaging ruggedization. Preliminary laboratory and field test results have shown great potential to meet not only the needs for reliable and precise pressure measurement of turbine engines but also for any other pressure measurements especially requiring high bandwidth and high temperature capability.

Acknowledgements

I would like to express my deep appreciation to Dr. Anbo Wang for serving as my advisor. It is impossible for me to finish my dissertation work without his patience, guidance and support. As a mentor and a friend, he continually and convincingly conveyed a spirit of adventure and an excitement in regard to research and scholarship during the past five years. With his encouragement, I will continue to work with confidence in my career.

I also would like to sincerely thank Dr. Gary R. Pickrell, Dr. Ira Jacobs, Dr. Ahmad Safaai-Jazi, Dr. Yilu Liu and Dr. Guy J. Indebetouw for serving on my committee and for their encouragements and valuable suggestions to improve the quality of the work presented here. I am also grateful to Kristie L Cooper for her great help in the past several years. I would like to thank Jonus Ivasauskas of Prime Photonics, LC for designing the ferrule holding fixture and M. Gredell, Dan Thorsen, and Dr. Dr. Russll G. May, also of Prime Photonics, for useful discussions. My gratitude also goes to all of my colleagues and friends at Center for Photonics Technology (CPT), which has been shared as a home. Among them, special thanks goes to former CPTers, Dr. Bing Qi, Dr. Po Zhang, Dr. Zhiyong Wang, Dr. Jiangdong Deng, Dr. Hai Xiao, Dr. Wei Peng and Dr. Bing Yu who work with me since 2000, as well as current CPTers, Xingwei Wang, Yan Zhang, Yongxin Wang, Bo Dong, Ming Han, Xiaopei Chen, Yizheng Zhu, Zhengyu Huang, Fabian Shen, Zhuang Wang, Xin Zhao, Dawoo Kim, Evan Lally and Bassam Alfeeli, for their valuable suggestions and supports to my presented work and I also thank Debbie Collins, Kathy Acosta and Bill Cockey, they have made the CPT a place to work with great pleasure.

I also would like to thank Dr. Wing Ng, Aditya Ringshia and Hugh Hill of the Dept. of Mechanical Engineering of Virginia Tech and Mr. Frank Caldwell for providing the engine test facilities and technical support, and Dr. Bo Song for many helpful discussions.

Finally, any words cannot express the thanks I owe to my parents, who raised me, trust me and support me with their endless love; and also to my old sister, their love remind me that family is more important than any academic degrees.

Table of Contents

Chapter 1 Introduction	1
1.1 Motivation.....	1
1.2 Scope of the proposed research.....	3
Chapter 2 Literature Review and Research Background	4
2.1 Fundamentals of pressure sensing.....	4
2.2 Pressure measurement methods review	5
2.2.1 Liquid manometers	5
2.2.2 Mechanical pressure gauges with flexing elements.....	6
2.2.3 Conventional electronic pressure sensors	7
2.2.4 MEMS based pressure sensors	8
2.2.5 Fiber optic pressure sensors	11
2.2.5.1 Polarization-modulated pressure sensor.....	12
2.2.5.2 Wavelength-modulated pressure sensor.....	12
2.2.5.3 Intensity-based FOPS.....	13
2.2.5.4 Interferometry based FOPS	14
2.3 Fiber optic Fabry-Perot interferometer sensors	15
2.3.1 Intrinsic Fabry-Perot Interferometer Sensor	15
2.3.2 Extrinsic Fabry-Perot Interferometer Sensor	16
2.4 Progress of pressure measurement in turbine engines.....	17
2.4.1 Pressures in turbine engines	17
2.4.2 State of art of engine pressure measurement.....	18
2.4.3 Fiber optic engine pressure sensors	18
Chapter 3 Principles of operation of the diaphragm-based EFPI sensors.....	22
3.1 Sensor system configuration.....	22
3.2 Sensor signal demodulation	25
3.2.1 Spectrum phase trace method.....	25
3.2.2 Interferometric-intensity trace method	26
3.3 Diaphragm mechanical analysis.....	28
3.3.1 Diaphragm deflection under pressure	29

3.3.2 Diaphragm frequency response	32
3.3.3 Stress Analysis.....	41
3.3.4 Single mode EFPI sensor	42
Chapter 4 Fabrication of the Diaphragm Based Fiber Optic Sensors	44
4.1 Sensor material selection	44
4.1.1 Metals.....	44
4.1.2 Ceramics.....	45
4.1.3 Glass.....	45
4.2 Sensor fabrication requirements.....	47
4.3 Basic sensor fabrication system	47
4.4 Research for sensor bonding methods.....	48
4.4.1 Epoxy bonding.....	48
4.4.2 Glass solder/powder bonding	48
4.4.3 Direct bonding	49
4.4.4 Anodic bonding	50
4.4.5 Sol-gel bonding.....	50
4.5 Laser fusion bonding	51
4.5.1 Sensor parts preparation.....	52
4.5.2 Laser Bonding System	53
4.5.3 Fabrication process	56
4.5.4 Vacuum sealing techniques.....	60
4.6 Sensor packaging.....	61
Chapter 5 Sensor Signal Interrogation Systems	63
5.1 White light interferometry system.....	63
5.1.1 Signal demodulation	66
5.1.1.1 One-valley tracing method	66
5.1.1.2 Air-gap absolute measurement	67
5.1.1.3 High resolution absolute measurement	68
5.2 CTS based sensor signal interrogation system.....	70
5.3 SCIIB sensor interrogation system.....	72
5.3.1 Single mode fiber based SCIIB System.....	73

Chapter 6 Sensor Calibration and Sensor System Performance.....	78
6.1 Sensors' temperature dependence	78
6.2 Static pressure test.....	80
6.2.1 Static pressure testing system.....	80
6.2.2 Sensor static pressure response	80
6.2.3 Sensor response repeatability and diaphragm creep	81
6.3 Sensors' dynamic pressure test	86
6.3.1 Dynamic pressure measurement.....	86
6.3.2 Sensor frequency response	87
6.3.3 Simulation test	92
6.4 Engine sensor field test.....	94
6.5 Engine combustor simulation system.....	100
Chapter 7 Miniature Diaphragm Based Fiber Optic Sensor.....	102
7.1 Miniature sensor structure	102
7.2 Miniature sensor fabrication	103
7.3 Performance analysis and testing	106
Chapter 8 Summary and Suggestions for Future Work.....	111
8.1 Summary and conclusions	111
8.1.1 Sensor modeling and the principle of operation.....	111
8.1.2 Sensor fabrication	112
8.1.3 Signal interrogation systems	112
8.1.4 Sensor testing.....	113
8.2 Summary of Contributions.....	114
8.3 Suggestions for Future work.....	114
Reference	116
List of Related Publications, Patents, and Presentations.....	121
Appendix: Visual Basic Programs for High Speed Sensor Data Acquisition	125
Vita	128

Table of Figures

Fig. 2.1 Illustration of an EFPI fiber optic sensor	16
Fig. 3.1 Schematic of fiber optic sensor system	22
Fig. 3.2 Illustration of an EFPI fiber optic sensor	22
Fig. 3.3 Reflections in an EFPI cavity	23
Fig. 3.4 Transmission as a function of phase in Fabry-Perot interferometer	24
Fig. 3.5 Reflection as a function of phase in Fabry-Perot interferometer	25
Fig. 3.6 Air-gap change induced spectrum shift.....	26
Fig. 3.7 Illustration of interference fringes versus sensor air-gap.	26
Fig. 3.8 Illustration of a linear operating range of the sensor response curve.....	28
Fig. 3.9 Structure model for the diaphragm	29
Fig. 3.10 Deflection curve of the diaphragm under pressure	30
Fig. 3.11 Simulation of the diaphragm deflection by using Matlab	30
Fig. 3.12 Required diaphragm thickness vs. Maximum pressure (0-10kpsi).....	31
Fig. 3.13 Required diaphragm thickness vs. Maximum pressure (0-500psi).....	31
Fig. 3.14 Theoretical sensitivities of the sensor for different diaphragm radius values. ..	32
Fig. 3.15 Theoretical natural frequency of the sensor.....	33
Fig. 3.16 Sensor frequency response with fundamental mode	40
Fig. 3.17 Radial and tangential stresses of a round silica diaphragm	42
Fig. 4.1 Schematic of fiber optic sensor fabrication system.....	47
Fig. 4.2 Epoxy bonding in the fiber sensor fabrication.....	48
Fig. 4.3 A fiber was bonded with a ferrule by glass solder.....	49
Fig. 4.4 Bonding fiber with ferrule with sol-gel	51
Fig. 4.5 Transmittance of a fused silica glass plate	52
Fig. 4.6 Automated laser bonding pressure sensor fabrication system.....	53
Fig. 4.7 Schematic of the diaphragm to ferrule laser bonding	53
Fig. 4.8 Photo of the automated laser bonding pressure sensor fabrication system	54
Fig. 4.9 Photo of the sensor laser bonding fixture	54
Fig. 4.10 Structure of the optical fiber pressure sensor.....	55
Fig. 4.11 The diaphragm to ferrule end bond (top view under microscope).....	58

Fig. 4.12 Fiber and ferrule thermal bonding.....	58
Fig. 4.13 Thermal bonding between an optical fiber and a ferrule.....	58
Fig. 4.14 Photo of the fused bonding between an optical fiber and a ferrule.....	59
Fig. 4.15 Photo of the engine sensor.....	59
Fig. 4.16 Vacuum-sealed laser bonding sensor fabrication.....	60
Fig. 4.17 Temperature dependences of the sensor fabricated in air and vacuum.....	61
Fig. 4.18 Fiber optic pressure sensor packaging.....	62
Fig. 4.19 Photo of the packaged fiber optic pressure sensor.....	62
Fig. 5.1 The basic structure of the interferometer-based white light system.	63
Fig. 5.2 Schematic of the white light system box.....	64
Fig. 5.3 LED and spectrometer based fiber optic white light system.....	65
Fig. 5.4 Fringes from a sensor connected to the single mode white light.....	65
Fig. 5.5 Fringes from a sensor connected to the multi-mode white light.....	66
Fig. 5.6 Schematic of the CTS based sensor interrogation system.....	70
Fig. 5.7 Photo of the sensor interrogation system.....	70
Fig. 5.8 Sensor signals from CTS (air-gap $\approx 31\mu\text{m}$).....	71
Fig. 5.9 Sensor signals from CTS (air-gap $\approx 25\mu\text{m}$).....	72
Fig. 5.10 Schematic of SCIIB fiber optic sensor interrogation system.....	73
Fig. 5.11 Schematic of the single-mode SCIIB sensor system box.....	74
Fig. 5.12 Photograph of the developed single-mode SCIIB sensor system.....	75
Fig. 5.13 The spectrum profile of the LED light source.....	75
Fig. 5.14 Narrowband output as a function of F-P cavity length d.....	76
Fig. 5.15 Broadband output as a function of F-P cavity length.....	76
Fig. 5.16 Ratio of narrowband to broadband as a function of F-P cavity length d.....	76
Fig. 6.1 Sensor temperature dependence from 25 °C to 700°C at atmospheric pressure.	79
Fig. 6.2 Schematic of the controlled pressure testing system.....	80
Fig. 6.3 Sensor pressure response at 25 °C and 700 °C.....	81
Fig. 6.4 Air-gap change caused by diaphragm creep under constant pressure (100psi) at 700°C.....	82
Fig. 6.5 The creep strain of a silicate glass.....	82
Fig. 6.6 Diaphragm creep and recovery (700 °C).....	83

Fig. 6.7 Temperature dependence of the viscosity of some glasses (a) fused silica, (b) aluminosilicate, (c) borosilicate, (d) soda-lime-silica, (e) lead borate.	84
Fig. 6.8 Radial strain estimation from the diaphragm small deflection	84
Fig. 6.9 Diaphragm deflection creep rate at high temperature	85
Fig. 6.10 Pressure Response at 400°C	85
Fig. 6.11 Pressure Response at 500°C	86
Fig. 6.12 Pressure Response at 600°C	86
Fig. 6.13 Static pressure response of the diaphragm-ferrule based pressure sensor.....	87
Fig. 6.14 Experimental setup for the sensor frequency response measurement.....	88
Fig. 6.15 Time domain response and its Fourier transform captured by the oscilloscope	89
Fig. 6.16 The sensor dynamic pressure test setup.....	90
Fig. 6.17 The engine sensor response by Q-point tuning.....	91
Fig. 6.18 The engine sensor dynamic pressure response (25 °C).....	91
Fig. 6.19 The engine sensor dynamic pressure response (600 °C).....	92
Fig. 6.20 Test sensor's dynamic response near an AC axial fan	93
Fig. 6.21 Sensor output of AC axial fan test	93
Fig. 6.22 Sketch of F-109 turbofan engine.....	94
Fig. 6.23 Engine pressure sensor installation	94
Fig. 6.24 Illustration of the sensor installation.	95
Fig. 6.25 F-109 turbofan engine	95
Fig. 6.26 Engine pressure sensor installation (side view)	96
Fig. 6.27 Flush mount holes in the aluminum ring of inlet.....	96
Fig. 6.28 Sensor signal processing and data acquisition devices	97
Fig. 6.29 Fiber sensor and Kulite sensor signals in time domain.	98
Fig. 6.30 Fiber sensor and Kulite sensor signals in frequency domain.....	99
Fig. 6.31 Schematic of the high temperature dynamic pressure test system.....	100
Fig. 7.1 Miniature diaphragm based fiber optic pressure sensor.....	103
Fig. 7.2 Micrograph of the miniature sensor	103
Fig. 7.3 Fabrication of the miniature diaphragm	105
Fig. 7.4 Fiber to tubing bonding	105

Fig. 7.5 Theoretical pressure sensitivities of the sensor with several diaphragm diameters.
..... 107

Fig. 7.6 Sensor static pressure response (15-50psi) at room temperature..... 107

Fig. 7.7 Theoretical natural frequency of the sensor for varying diaphragm diameters. 108

Fig. 7.8 Sensor dynamic pressure (acoustic wave) response at room temperature 109

Fig. 7.9 Sensor temperature dependence at room pressure 110

Chapter 1 Introduction

1.1 Motivation

Pressure measurement is an essential technology in many industry applications, for example, pressure monitoring in oil storage tanks [1] and vacuum level control in chambers [2]. Some applications such as gas turbine engines [3] and oil wells [4] involve harsh environments. Acquiring accurate pressure measurements in these harsh environments has always challenged the available measurement technology. The motivation of this research is to meet the recent increasing needs for optical fiber pressure sensors capable of operating accurately and reliably in these harsh environments, especially in turbine engines.

Gas turbine engines employed in civilian and military aircraft consume large amounts of jet fuel daily, and the energy consumption attributed to this industry is increasing. Under increasing demand by engine users, manufacturers are extending operating envelopes of gas turbine engines to their limits to achieve higher thrust, better efficiency, lower emissions, improved reliability and longer engine life. The industry consensus is that these goals can be realized by strategic measurements at various locations in an engine for design optimization and real-time diagnosis during service [5]. However, the operating environment within the engine, characterized strong EMI and high temperature, pressure, and turbulence, shortens the lifetimes of currently available sensors.

The following gives a brief description of some of these measurement needs. The failure of turbine blades has been a major problem to both engine designers and users. This long existing problem is partially due to a lack of information about the mechanical behavior of high-RPM blades at elevated temperatures and pressures. Pressure and temperature measurements in compressor and turbine sections are highly

desirable to determine blade load distribution. For the fan blades, temperatures can vary from -40 to 100°C with a pressure on the order of 30psi. However, for the turbine vanes and blades, the temperatures can exceed 500°C and the pressure can be well above 100psi. The first 10% of the boundary layer of the gas flow path along the engine walls contributes to the generation of turbulence, which may produce instabilities in the downstream gas flow. Pressure and temperature measurement is thus of great importance as the first step toward turbulence monitoring and control. Once in place, the sensor relays information to a control system that can automatically adjust the engine for smoother operation, which will improve the engine operational performance and reliability.

The widely used semiconductor pressure sensors have several major drawbacks. These include a limited maximum operating temperature of 482°C , poor reliability at high temperatures, severe sensitivity to temperature changes, and susceptibility to electromagnetic interference.

Compared with conventional electronic sensors, fiber optic sensors have many advantages including small size, light weight, high sensitivity, large bandwidth, high reliability, immunity to electromagnetic interference and anti-corrosion and absence of a spark source hazard for flammable environments. Fiber optic sensors can also survive at much higher temperatures than conventional pressure sensors [6].

The basic operating principle of an extrinsic Fabry-Pérot interferometric (EFPI) [7, 8] enables the development of sensors that can operate in the harsh conditions associated with turbine engines and other aerospace propulsion applications, where the flow environment is dominated by high-frequency pressure caused by combustion instabilities, blade passing effects, and other unsteady aerodynamic phenomena. Both static and dynamic pressures exist in turbine engines, which must be measured by one sensor. Diaphragm-based Fabry-Perot Interferometric (DFPI) fiber optic pressure sensors are capable of measuring static and dynamic pressure simultaneously.

However, the existing (DFPI) sensors can only work below 500°C because of the sensing materials or bonding methods utilized [9-13].

In this research, novel diaphragm-based fiber optic high temperature pressure sensors based on extrinsic Fabry-Pérot interferometric technology were developed and tested for pressure measurement in turbine engines.

1.2 Scope of the proposed research

The major objective was to develop a robust fiber optic pressure sensor (FOPS) technology for harsh environmental sensing applications, e.g. detection of pressures in turbine engines. The research work of in this dissertation is focused on three issues:

- 1) Develop an innovative sensor scheme with high sensitivity, high bandwidth and high operating temperature capability to meet the requirements of turbine engine applications.
- 2) Develop the FOPS probe fabrication techniques and fabrication system to minimize the temperature cross-sensitivity of the sensor and ensure fabrication repeatability.
- 3) Design and implement a sensor testing and simulation system to evaluate the sensor performance and to calibrate the sensor.

More detailed background information and pressure sensing technology review will be presented in chapter 2. The principle of the diaphragm-based pressure sensor is described in Chapter 3. Chapter 4 presents the sensor fabrication techniques. The sensor instrumentation system and signal demodulations are presented in Chapter 5. The sensor calibration, performance and field test results are reported in Chapter 6. Chapter 7 will describe a miniature diaphragm based pressure sensor and Chapter 8 will give a summary and list some future work.

Chapter 2 Literature Review and Research Background

2.1 Fundamentals of pressure sensing

Pressure is defined as the force per unit area, which is a derived quantity and as such has no primary standard. Development of pressure standards is therefore based on the primary quantities of mass and length.

Table 2.1 shows some typical pressure sensing applications. There are a variety of units used in pressure measurement and the following conversion factors should help in dealing with the various units:

$$1 \text{ psi} = 51.714 \text{ mmHg} = 6.8946 \text{ kPa}$$

$$1 \text{ bar} = 14.504 \text{ psi}$$

$$1 \text{ atm.} = 14.696 \text{ psi}$$

Basically, there are two types of pressure measurement sensors, absolute and differential pressure sensors, which are distinguished as follows:

Absolute pressure sensor:

As the rear side of the sensing element is not accessible, pressure can only be applied on the front side of the sensor. To achieve an absolute pressure signal, the reference pressure is set to vacuum.

Differential pressure sensor:

The rear side of the sensing element is accessible. Pressure can be applied to both sides of the sensing element, and the difference in these pressures is measured. If atmospheric pressure is taken as the reference pressure, the sensor works as a pressure gauge.

Table. 2.1 Pressure sensing characteristics in some typical applications

	Static Pressure	Dynamic Pressure (Acoustic)
Air	Turbine engine: up to 500psi Vacuum chamber: 0~14.7psi	Turbine engine: ~1psi @ 0.5~10KHz Microphone: 0.01~20 Pa @ 20~20kHz
Hydraulic	Oil well: up to 20000psi Deep sea: up to 14700psi	Partial discharge: ~0.01psi @ 30~300kHz Blood pressure: ~100mmHg @ ~1Hz

2.2 Pressure measurement methods review

In general, there are two basic approaches to measuring pressure, either directly, by determining the force applied to a known area, or indirectly, by determining some effect of an applied pressure. The simplest direct method is balancing an unknown pressure against the pressure produced by a column of liquid of known density (manometric techniques). The second method uses an elastic member of known area as the sensing element on which pressure acts and the resultant stress or strain is then measured to calculate the actual pressure value [14].

2.2.1 Liquid manometers

The manometer is one of the oldest devices for pressure measurement. It uses the hydrostatic balance principle where a pressure is measured by the height of a liquid that it supports. A typical example is the mercury manometer, which uses mercury as the fluid medium. In fact, mercury manometers are so popular that the height of mercury column has been adopted as a unit for pressure measurement, especially in medical applications. (1 mmHg = 133.322 Pa). Manometers have the advantages of simplicity and visibility. However, they have the drawback of large temperature dependences. The effect of temperature on the density of the fluid used in the

manometer can introduce errors to pressure measurement. Because of this, manometers nowadays are rarely seen in field applications. However, liquid manometers are still widely used in laboratories and workshops where they are used as calibration standards.

2.2.2 Mechanical pressure gauges with flexing elements

Flexing elements can be used to measure pressure by measuring the motion of the flexible member caused by the pressure. The majority of early mechanical pressure gauges utilize a Bourdon tube, stacked diaphragms, or a bellows as their pressure sensing elements. The applied pressure causes a change in the shape of those flexible members and moves a pointer with respect to a scale.

Bourdon tubes can be made from a variety of elastic materials such as phosphor bronze, beryllium copper and stainless steel. A simple Bourdon tube usually has an oval cross-section and is bent into a circle with one end sealed (referred as the free end). When the unknown pressure enters through the fixed open end, the tube uncoils slightly and the amount of the deflection of the free end is thus directly proportional to the applied pressure.

Metallic diaphragms in pressure gauges are often made with corrugated surfaces to improve the sensitivity, linearity, and frequency response. The diaphragm is mounted to separate the pressure inlet and a cavity with a known pressure. When the unknown pressure acts on one side of the diaphragm, the diaphragm bends with a motion that is proportional to the pressure difference.

The performance of mechanical pressure gauge varies widely, not only as a result of their basic design and construction materials, but also because of the conditions under which they are used. The principal sources of error are hysteresis in the flexing elements, changes in sensitivity due to temperature changes, frictional effects, and backlash in the pointer mechanism. The typical accuracy of a mechanical pressure gauge is about 2% of the full scale though some delicate systems can reach an

accuracy as high as 0.1% of full scale [15]. Other drawbacks of the mechanical pressure gauge include the non-linear output and the large size.

2.2.3 Conventional electronic pressure sensors

In order to improve the sensitivity and resolution as well as to provide means for compensating for nonlinear effects and the ability to transmit data over considerable distance, electrical/electronic devices were later added for converting mechanical displacements into an electrical signal thereby creating a whole family of electronic pressure transducers. Many years of research and development of pressure measurement techniques have resulted in various pressure transducers including:

- Capacitive
- Differential transformer
- Inductive
- Force balance
- Piezoelectric
- Piezoresistive
- Potentiometric
- Vibrating wire or tube
- Strain gauges

In almost all these pressure transducers, the pressure signal is converted to the deflection or movement of the pressure-sensing element, and thereafter measured by different electronic sensing techniques. The performance of these pressure transducers is summarized in Table 2.2. As shown in the table, the transducers vary widely in performance and cost.

Table 2.2 Typical performances of electronic pressure transducers

Transducer type	Resolution	Range	Frequency response	Temperature dependence	Stability	Hysteresis
Capacitive	0.01%	Low	Variable	Large	Good	Small
Differential transformer	±0.5%	Low	1kHz	Moderate	Good	Small
Force balance	0.05%	Large	DC to 5Hz	Small	Excellent	Moderate
Inductive	±0.5%	Large	DC	Moderate	Good	Large
Piezoelectric	0.02%	2 to 1000 bar	10Hz to 100kHz	Moderate	Good	Small
Piezoresistive	0.01%	1 to 1000 bar	High	Large	Fair	Small
Potentiometric	1%	Low	Low	Large	Fair	Large
Strain gauges	1% to 0.05%	<500 bar	High	Large	Good	Low
Vibrating wire or tube	0.1%	Low	High	Large	Poor	Low

2.2.4 MEMS based pressure sensors

Successes in the semiconductor industry have brought the sensing community a new type of sensor based on microelectromechanical systems (MEMS) technology. These MEMS devices were initially manufactured using standard semiconductor processing along with orientation dependent (or anisotropic) wet chemical etching and wafer bonding [16]. Improvement in silicon etching technology has continued the trend to provide better methods for MEMS sensor fabrication. The P⁺/Si etch stop scheme used for controlling the thickness of the membrane was later replaced by electrochemical means [17]. More recently, the highly directional plasma etching technique was developed to achieve the fast etching rate and a high depth-to-width aspect ratio [18-20]. This new dry etching technique is based on high density sulfur hexafluoride and

oxygen plasma, which results from the combination of the reactant gases or alternating process of etching and protective polymer deposition. The process is orientation independent and has a high Si etching rate ($\geq 2 \mu\text{m}/\text{min}$) as compared to SiO_2 ($\leq 0.013 \mu\text{m}/\text{min}$) and photoresist ($\leq 0.026 \mu\text{m}/\text{min}$). In terms of sensor packaging techniques, the silicon to silicon bonding is now replacing anodic and glass frit bonding to avoid the detrimental effect caused by mismatch of thermal expansion coefficients between Si and glass.

MEMS based pressure sensors can be categorized into two different types, piezoresistive and capacitive, based on the two physical mechanisms used to convert mechanical motion to an electronic signal [21].

Ever since the piezoresistance effect (referred to as the physical phenomenon of resistance as a function of the applied strain or stress) in semiconductor materials was discovered [22, 23], it has been widely applied to manufacture pressure sensors [24]. The piezoresistive effect is the change in electrical resistivity that occurs with application of mechanical stress. Thus, piezoresistive transducers convert changes in external stress to proportional, measurable electrical signals. A piezoresistive pressure sensor is usually made by placing sensing resistors on the top of a silicon diaphragm. When the diaphragm is subject to the applied pressure, the resultant strain from the deflected diaphragm will change the resistance value of the sensing resistors. Readout of such sensors has largely been done by a Wheatstone bridge configuration, formed by two R_p^+ resistors (their resistance increases with pressure) and two R_p^- (their resistance decreases with pressure).

Capacitive sensors will generate an electrical signal as a result of the elastic deformation of a membrane. However, it is not the built-up stress in the membrane that causes the signal, but rather its displacement. The capacitive MEMS sensor is usually a parallel-plate capacitor formed between a sensing diaphragm and a substrate. The deflection of the diaphragm resulting from the applied pressure causes a change in the distance between these two plates and thus results in a change of capacitance as a

function of the applied pressure [25]. Through two electrical wires, the capacitor is connected to an electrical circuit, which converts the capacitance to either a voltage signal or a frequency signal as the sensor readout.

Most commercial MEMS pressure sensors to date use piezoresistive techniques. In general, the piezoresistive sensor has very good linearity due to the inherent linear resistance-pressure relation. Piezoresistive-type pressure sensors have been used widely and accurately in the measurement of dynamic pressure changes. However, a major problem associated with the piezoresistive pressure sensor is its inherent cross sensitivity to temperature. The influence of temperature on a piezoresistive pressure sensor can cause these sensors to drift about 100 Pa per day, which makes them deficient when it comes to a long-term measurement. Other drawbacks of the piezoresistive sensor include the large power consumption and the very strict requirement of placing the sensing resistors accurately to obtain maximal sensitivity. In contrast to the piezoresistive sensor, the capacitive sensor has a large nonlinearity because of the nonlinear function of the capacitance-pressure relation. On the other hand, the displacement-based measurement mechanism makes the capacitive sensor less sensitive to the temperature variation [26]. The introduction of a dummy reference pressure-insensitive capacitor in the same cavity further improved the temperature stability of the capacitive sensor [27]. It is well known that the capacitive detection principle is supreme concerning sensitivity and power consumption. However, since the electrical capacitances are normally very small, the electrical connections to the sensor are very sensitive to parasitics and noise. Therefore, it is desired to make the connections as short and well defined as possible, which makes the packaging of the sensor a big challenge.

MEMS-based sensors have the advantages of small size, high sensitivity, low cost, potential of large production, and batch fabrication process for a large production field. Although it is a quite natural idea to integrate electronic networks on the same chip where the sensing mechanism is located, this approach is far from natural from the fabrication technology viewpoint. Sensor fabrication requires dedicated processing

sequences that may conflict with the IC processing, impeding the merging of both devices. Often, the circuit processing will have to be performed at the beginning, and then the wafers are post processed in the micromachining foundry.

There are certain drawbacks that impede the large-scale application of MEMS-based sensors for harsh environmental sensing applications. First, MEMS pressure sensors with integrated electronics based on silicon materials are limited to operation at temperatures below 150°C [28]. In order to extend the temperature range of operation, other materials with high stability need to be used in the sensor construction [29]. However, the introduction of other materials makes the sensor packaging even more difficult and worsens the temperature cross sensitivity of the sensor due to the mismatch of the coefficients of thermal expansion (CTE). Second, the electromagnetic nature of the MEMS sensor renders them subject to electromagnetic interferences (EMI) when used in harsh environments.

2.2.5 Fiber optic pressure sensors

Fiber optic sensors can be used to measure pressure [30-32] and possess a number of inherent advantages [6] including (i) immunity to electromagnetic interference, (ii) wide range of potential measurands, (iii) high resolution, (iv) remote sensing capability, (v) high reliability and (vi) do not pose a spark source hazard for flammable environment applications. A variety of fiber optic pressure sensors (FOPS) have been developed and proven themselves in many applications.

The light transmitted through an optical fiber can be characterized by such parameters as intensity, wavelength, phase, and polarization. By detecting the change of these parameters resulting from the interaction between the optical fiber and the measurand, fiber optic sensors can be designed to measure a wide variety of physical and chemical parameters. Accordingly, fiber optic sensors can be categorized into four major groups including: intensity based fiber optic sensors, color modulated fiber optic sensors, phase modulated (or interferometric) fiber optic sensors, and polarization modulated

fiber optic sensors. More than three decades of extensive research in fiber optic sensor technologies has greatly enhanced the technical background of all the sensor categories, and the applications of each group of the sensors are expanding very rapidly.

2.2.5.1 Polarization-modulated pressure sensor

The mainstream of developed polarization-modulated fiber optic sensors are based on two different physical effects: the Faraday effect and the photoelastic effect. Sensors based on the Faraday effect are mainly used to measure electrical or magnetic field with the typical application of the measurement of the electrical current. On the other hand, photoelastic fiber sensors are naturally suitable for developing into pressure sensors because the photoelastic effect directly transfers the applied pressure into the change of the polarization property in the optical medium. Although silica glass fiber itself exhibits a very weak photoelastic effect, external optical crystals are often used as the sensing element for better control and more accurate measurement. The first fiber optic pressure sensor based on the photoelastic effect was introduced in 1982 by Spillman [33]. Since then, many photoelastic fiber sensors have been reported by different authors with their emphases on the development of clever methods to compensate for the optical power variation of the system [34]. With a very good self-compensation mechanism, an external photoelastic pressure sensor could achieve an accuracy of 0.2%. However, the self-compensation had to be constructed at the same location as the external sensing element, which made the sensor head very bulky and difficult to be protected in harsh environments.

2.2.5.2 Wavelength-modulated pressure sensor

The most popular wavelength-modulated fiber optic sensor has been the Fiber grating-based sensor ever since the first fiber grating was manufactured in 1989 through transverse UV exposure [1]. Fiber sensors based on both Bragg gratings and long period gratings have been developed for the measurement of temperature, strain and pressure [35]. By coating the grating region with specially designed elastic material or

encapsulating the grating into a glass bubble, fiber grating sensors have been used to measure hydrostatic pressure with a typical resolution of 0.5% [36, 37]. Fiber grating sensors have the advantages of immunity to the optical power loss variation of the optical network and the capability of multiplexing many sensors to share the same signal processing unit. However, the long-term reliability of the fiber grating sensors has been a concern due to the degradation of optical properties and mechanical strength when the grating is exposed to high temperature and high pressure environments [38]. Moreover, when used for pressure measurements, fiber grating sensors exhibit relatively large temperature dependence, which limits their scale of applications for harsh environmental sensing.

In summary, although optical fiber-based pressure sensors have the potential opportunity to replace the majority of conventional electronic pressure transducers in existence in today's sensor market because of their unique set of advantages that can't be offered by other technologies, technical difficulties still exist and delay this becoming a reality. The most common concerns about the practical applications of fiber optic pressure sensors include the stability issue and the cross-sensitivity among multiple environmental parameters. The fluctuation of source power and the change in fiber loss can easily introduce errors to the measurement results, which make most optical fiber-based sensors unstable. The fact that most fiber sensors are cross sensitive to temperature changes also makes it difficult to use fiber optic sensors to measure parameters other than temperature in many practical applications. In order to be able to apply fiber optic sensors to real applications, research must be performed to overcome these technical difficulties.

2.2.5.3 Intensity-based FOPS

In general, intensity-based FOPS are inherently simple and require only a modest signal processing complexity through a direct detection of the change in optical power either in transmission or reflection. A well-developed and successfully commercialized intensity-based sensor is the multimode optical fiber microbend

sensor, which bases its principle on the physical phenomenon that mechanical periodic microbends can cause the energy of the guided modes to be coupled to the radiation modes and consequently results in attenuation of the transmitted light. Pressure sensors can thus be constructed by designing the mechanical microbending device to transfer the applied pressure to the optical intensity change. Although microbend pressure sensors have been reported with very high resolution (typically better than 0.1%), the large hysteresis and the power fluctuation associated with the optical source and fiber loss limit their accuracy within a few percent of the full scale [39]. The large size of the mechanical microbending mechanism also makes the microbend fiber optic pressure sensor impractical in many sensing applications where the size of the sensor is restricted to a very small dimension.

2.2.5.4 Interferometry based FOPS

To date, four types of interferometric FOPSs have been investigated for the measurements of displacement, temperature, strain, pressure and acoustic signals. These are the Mach-Zehnder, Michelson, Fabry-Perot, and Sagnac interferometers. Among them, the first three interferometric sensors have been developed into pressure sensors while the Sagnac interferometer has been primarily used for gyroscopes.

Mach-Zehnder and Michelson interferometers are the two intrinsic fiber sensors that were investigated extensively for acoustic pressure detection in the early stage of fiber sensor development. For example, underwater hydrophones based on these two interferometers were reported to have very high resolution of 0.01% [39]. However, due to the very low level of photoelastic or stress-optic coefficients of the silica glass fibers, a very long length of sensing fiber is necessary to obtain the desirable sensitivity, which unavoidably makes the sensor thermally unstable. Another drawback associated with these two types of interferometric sensors is the polarization-fading problem, which refers to the interference fringe visibility as a function of the polarization status of the light transmitted inside the fibers. The temperature instability and the polarization fading problem both render the Mach-Zehnder and Michelson interferometric sensors unsuitable for the long-term

measurement of DC pressure signals where the sensor drift must be kept to a very small level.

2.3 Fiber optic Fabry-Perot interferometer sensors

The Fabry-Perot interferometer is a very useful tool for high precision measurement, optical spectrum analysis, optical wavelength filtering, and construction of lasers [40, 41]. It is a high resolution, high throughput optical spectrometer that works on the principle of constructive interference. The Fabry-Perot interferometer is a very simple device that is based on the interference of multiple beams [42]. It consists of two partially transmitting mirrors that form a reflective cavity. Incident light enters the Fabry-Perot cavity and experiences multiple reflections between the mirrors so that the light can produce multiple interferences.

According to the different behaviors of the incident light, fiber optic Fabry-Perot sensors can be classified into two types — extrinsic F-P sensors and intrinsic F-P sensors [43]. In extrinsic sensors, the light can be allowed to exit the fiber and be modulated in a separate zone before being relaunched into either the same or a different fiber. They form an interferometric cavity outside the fiber, and the fiber just acts as a medium to transmit light into and out of the Fabry-Perot cavity. In intrinsic sensors, the light can continue within the fiber and be modulated. A Fabry-Perot cavity is formed by a section of fiber with its two end faces cleaved or coated with reflective coatings.

2.3.1 Intrinsic Fabry-Perot Interferometer Sensor

In intrinsic sensors the fiber construction materials are deliberately chosen in order to give sensitivity to one or more parameters [43]. Often it is not cost effective to make highly specialized fibers for sensing applications; therefore intrinsic sensors may utilize readily available fiber in specialized configurations and in conjunction with sophisticated instrumentation.

Usually an Intrinsic Fabry-Perot Interferometer (IFPI) sensor is fabricated by splicing a section of special fiber with its two endfaces coated with reflective films to regular fibers. The interferometric superposition of multiple reflections at the two special fiber's end faces generates the output signal, which is a function of the F-P cavity length, the refractive index of the special fiber, and the reflectance of the coating. The change of the F-P cavity length or the refractive index of the special fiber can be detected by tracking the interference output (either through the reflection or the transmission). Various physical or chemical parameters such as temperature, pressure and strain can be measured with a high resolution using an IFPI sensor.

2.3.2 Extrinsic Fabry-Perot Interferometer Sensor

In extrinsic sensors the performance of the device should be independent of the fiber and depend only on the nature of the sensing element, hence it offers the flexibility to design the Fabry-Perot cavity to accommodate different applications. A typical EFPI sensor configuration is shown in Fig. 2.1. It consists of a cavity that is formed between an input optical fiber and a reflecting optical fiber. Although the two reflectors of forming the Fabry-Perot cavity can be the surfaces of any optical components, a very simple way to form an EFPI will be using the well-cleaved end faces of two fibers.

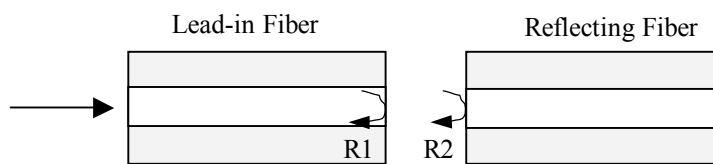


Fig. 2.1 Illustration of an EFPI fiber optic sensor

As shown in Fig. 2.1, the light from an optical source propagates along the input optical fiber to the Fabry-Perot cavity that is formed by the input optical fiber and the reflecting optical fiber. A fraction of this incident light $R1$, approximately 4%, is reflected at the end face of the input optical fiber backward the input optical fiber. The light transmitting out of the input optical fiber projects onto the fiber end face of the

reflecting optical fiber. The reflected light R2 from the reflecting optical fiber is partially recoupled into the input optical fiber.

Optical fiber Extrinsic Fabry-Perot interferometers (EFPI) have also been developed into pressure sensors [7]. Compared to the Mach-Zehnder and Michelson sensors, the EFPI sensor has advantages such as high sensitivity, small size, simple structure, polarization independence, and great design flexibility; EFPI fiber optic sensors are therefore attractive for many sensing applications. Moreover, because the optical fibers are packed very closely together, there is a potential advantage to minimize the temperature dependence of the sensor.

In summary, optical fiber interferometric sensors usually have the reputation of design flexibility of the sensing element, large dynamic range, and extremely high resolutions. However, due to the non-linear periodic nature of the interference signal, the accurate detection of the differential phase change of an interferometer becomes a real challenge. Very often, the complexity of the phase demodulation part of the interferometric sensor contributes the most to its high cost.

2.4 Progress of pressure measurement in turbine engines

2.4.1 Pressures in turbine engines

Gas turbine engines employed in civilian airplanes and military aircraft consume large amounts of jet fuel daily, and the energy consumption attributed to this industry is increasing. Under increasing demand by engine users, manufacturers are extending operating envelopes of gas turbine engines to their limits to achieve higher thrust, better efficiency, lower emissions, and improved reliability. The industry consensus is that these goals can be realized by strategic measurements at various locations in an engine for design optimization and real-time diagnosis during service [5]. However, the harsh operating environment within the engine, characterized strong EMI and high

temperature, pressure, and turbulence, shortens the lifetimes of currently available sensors.

The following gives a brief description of some of these measurement needs. The failure of turbine blades has been a major problem to both engine designers and users. This long existing problem is partially due to a lack of information about the mechanical behavior of high-RPM blades at elevated temperatures and pressures. Pressure and temperature measurements in compressor and turbine sections are highly desirable to determine blade load distribution. For the fan blades, temperatures can vary from -40 to 100°C with a pressure on the order of 30psi. However, for the turbine vanes and blades, the temperatures can exceed 500°C and the pressure can be well above 100psi. The first 10% of the boundary layer of the gas flow path along the engine walls contributes to the generation of turbulence, which may produce instabilities in the downstream gas flow. Pressure and temperature measurement is thus of great importance as the first step toward turbulence monitoring and control. Once in place, the sensor relays information to a control system that can automatically adjust the engine for smoother operation, which will improve the engine operational performance and reliability.

2.4.2 State of art of engine pressure measurement

The widely used semiconductor pressure sensors have several major drawbacks. These include a limited maximum operating temperature of 482°C , poor reliability at high temperatures, severe sensitivity to temperature changes, and susceptibility to electromagnetic interference.

2.4.3 Fiber optic engine pressure sensors

Fiber optic pressure sensors are capable of working in hostile environments such as turbine engines. Compared with hollow cylinder based pressure sensors for static pressure measurement [4, 8], diaphragm based configurations are more suitable for both static and dynamic pressure measurements [44, 45]. However, these diaphragm

based pressure sensors are still not suitable for applications above 500°C. Also, the large coefficient of thermal expansion (CTE) mismatch will cause severe stress between different materials used in sensor construction. This stress will degrade the sensor performance or lead to a failure. Even if the same material is used to fabricate the sensor elements, the bonding adhesive used, especially if epoxy-based, is still a major concern for the sensor's performance [10, 11]. For example, epoxy will exhibit a time-dependent viscoelastic dimensional change and will decompose at high temperatures. Also, the bonding adhesive having a different CTE from the sensor elements will cause a large temperature dependence in the pressure measurement or cause the sensor to fail. Although anodic bonding [12, 13] is adhesive free bonding, it cannot be used for bonding fused silica glass, which has a higher softening point and much lower CTE than other glass and is the most compatible material to silica optical fiber.

The goal of this research was to develop a new diaphragm based fiber optic EFPI engine pressure sensor, which has high sensitivity, high temperature capability, large bandwidth and low thermal-induced measurement error. Also, the sensor must be reliable and anticorrosion. In general, the fiber optic engine pressures have to satisfy several special requirements as explained below.

1. High temperature capability

High temperature is very often involved in many harsh environments. For example, temperatures in turbine engines can reach 500°C or much hotter depending upon which region of the turbine. The high temperature is the main reason that renders most electronic sensors inapplicable. Although optical fibers can sustain temperatures as high as 800°C before the dopants start to thermally diffuse appreciably, extra attention must be paid to the design and fabrication of the fiber sensor in order to maintain the desirable performance at such high temperature.

2. High pressure capability

Pressures as high as 500 psi can be encountered in turbine engines. In order to be able to survive in such high pressure environments, fiber optic pressure sensors must be designed and fabricated with enough mechanical strength and with their optical paths hermetically sealed to provide the necessary protection.

3. High Bandwidth

Dynamic pressures with frequency up to 50kHz exist in turbine engines. The pressure sensor must have very high frequency response.

4. Good thermal stability

Fiber optic pressure sensors designed for high temperature applications must be thermally stable or have the capability of compensating for temperature variations. Otherwise the temperature fluctuation of the environment can easily introduce large errors in the pressure measurement results.

5. Absolute measurement and self-calibration capability

Fiber optic pressure sensors with absolute readouts are much more attractive in applications for harsh environments because of their exemption from initialization and/or calibration when the power is switched on. In addition, the sensors are required to have self-calibration capability so that the fiber loss changes and the source power fluctuations can be fully compensated, or absolute measurement becomes meaningless.

6. Cost-effectiveness

As the market for fiber optic pressure sensors for harsh environment opens rapidly, the cost of the sensors and instrumentation is becoming a concern of increasing importance. In order to achieve successful commercialization, fiber optic pressure sensor systems must be robust as well as low cost. This requires that the complexity of the fiber sensor system must be kept to the minimum and the technique and process of fabricating sensor probes must have the potential of allowing mass production.

7. Installability

Fiber optic pressure sensors designed for harsh environment applications must be capable of remote operation and flexible enough for easy installation. This requires the sensor size to be small enough to fit in the limited space where the sensor will be located. Also, the sensor packaging must be compatible with the standard installation ports.

Chapter 3 Principles of operation of the diaphragm-based EFPI sensors

This chapter will describe the basic sensor system configuration; sensor mechanical analysis including diaphragm deflection, frequency response and stress distribution; and signal demodulation schemes including interference phase trace and intensity trace methods.

3.1 Sensor system configuration

The basic configuration of a single ended fiber optic sensor system is shown in Fig. 3.1. The light was coupled into the sensor through a 3dB 2x2 coupler and the reflected light was routed back through the same coupler to the detector for signal processing.

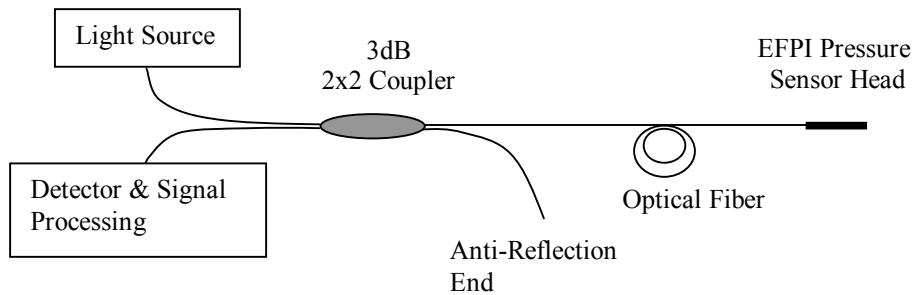


Fig. 3.1 Schematic of fiber optic sensor system

A schematic of a Fabry-Perot cavity between an optical fiber end face and a reflective mirror is shown in Fig. 3.2.

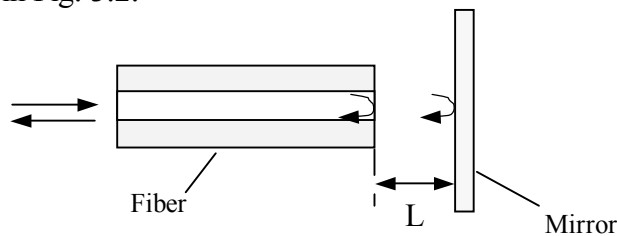


Fig. 3.2 Illustration of an EFPI fiber optic sensor

The light beam is reflected back and forth between the fiber end face and mirror, but at each reflection only a small fraction of the light is transmitted. The refractive index of the material is n . Assuming normal incidence, the Fresnel reflection coefficient r is given by [46]:

$$r = \frac{(n_1 - n_2)^2}{(n_1 + n_2)^2} \quad (3-1)$$

where n_1 and n_2 are the refractive indices of the two media forming the boundary. For silica glass/air interfaces, the reflectivity is about 4%. As shown in Fig. 3.3, the first two beams coupling back to the lead-in fiber have much stronger intensities than the higher order reflections; the optical signal modulation can be simplified as two-beam interference. The optical path difference (OPD) between the two beams is:

$$\Delta d = n2L \quad (3-2)$$

and the phase difference is given by

$$\phi = \frac{2\pi \cdot \Delta d}{\lambda} = \frac{4\pi \cdot n \cdot L}{\lambda} + \pi \quad (3-3)$$

where λ is the light wavelength in vacuum,
 n is the refractive index of air
 L is the F-P cavity length

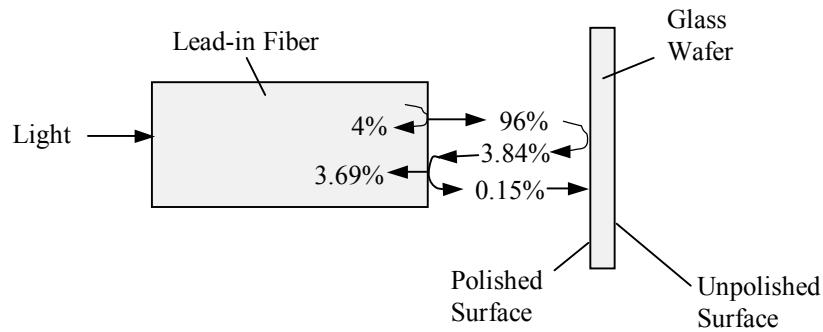


Fig. 3.3 Reflections in an EFPI cavity

If $\phi=N2\pi$ (N is an integer), all the transmitted light are in phase and they will interfere constructively. If $\phi=N\pi$, each pair of signals is out of phase and destructive interference will occur. If the plates are highly reflective, the intensity of the ray trapped in the cavity decreases little between reflections; the transmitted waves have almost the same amplitude and the result has almost zero intensity.

If the phase difference is $N\pi$, then the first transmitted light beam will interfere destructively with the 3rd, the 2nd with the 4th etc. At this point only waves with $\phi=2\pi$ can be transmitted. For mirrors with finite reflectivity, the transmitted intensity (I_t) can be given by [40]:

$$\frac{I_t}{I_i} = \frac{1}{1 + \left(\frac{2r}{1-r^2}\right)^2 \sin^2\left(\frac{\phi}{2}\right)} \quad (3-4)$$

where I_i is the incident intensity and r is the fraction of the amplitude of the wave that is reflected at each boundary. The factor $\left(\frac{2r}{1-r^2}\right)^2$ is sometimes referred to as the finesse. The larger the finesse, the sharper the peak around $\phi=2\pi$. The result is shown in Fig. 3.4.

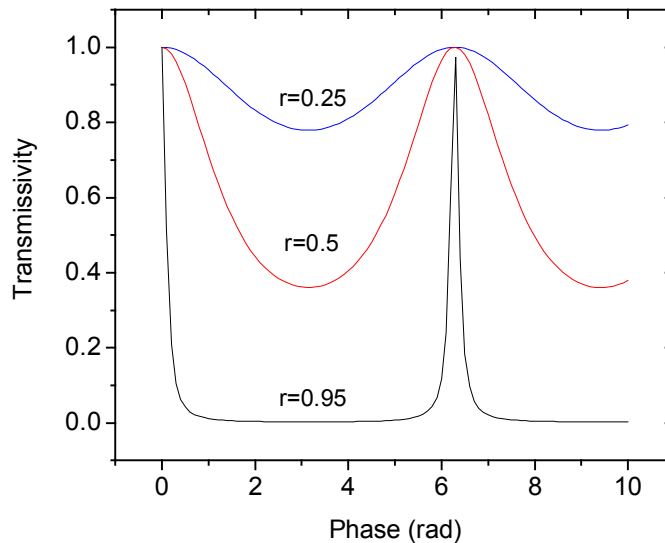


Fig. 3.4 Transmission as a function of phase in Fabry-Perot interferometer

Since EFPI sensors are usually used in single end mode as shown in Fig. 3.1, the reflection properties are more important, which are shown in Fig. 3.5.

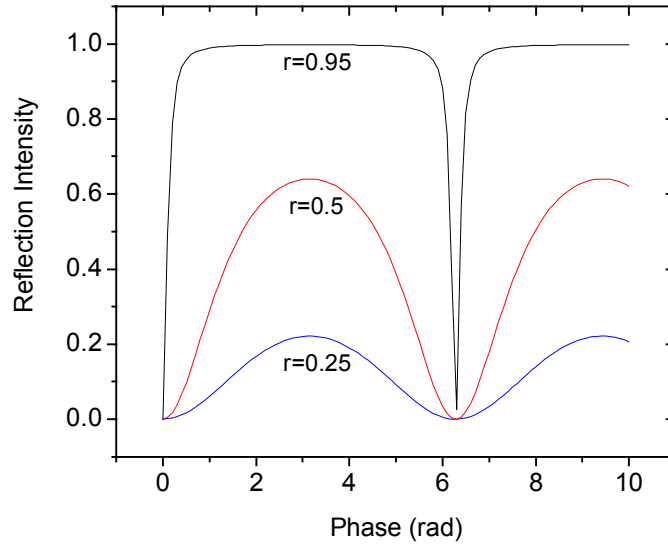


Fig. 3.5 Reflection as a function of phase in Fabry-Perot interferometer

3.2 Sensor signal demodulation

Two signal demodulation schemes were studied, one is spectrum phase trace algorithm [47], which has high resolution and large measurement range but slow response, the other is self-calibrated interferometric-intensity-based (SCIIB) method [8], which has large bandwidth, suitable for high frequency dynamic applications.

3.2.1 Spectrum phase trace method

When a wideband light source (such as a LED) or a wavelength tunable light source was used in sensor system, an interference signal was generated from the EFPI sensor head. The fringes are shown in Fig. 3.6.

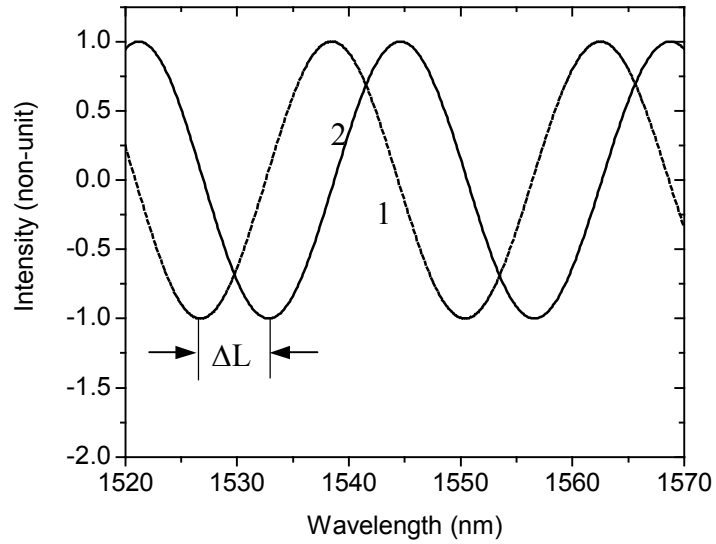


Fig. 3.6 Air-gap change induced spectrum shift.

3.2.2 Interferometric-intensity trace method

For an interferometric-intensity based pressure sensor, the intensity of the sensor output will change sinusoidally with the air-gap changes. In order to eliminate fringe direction ambiguity, the sensor can be designed such that it is operated within a linear range of one fringe as shown in Fig. 3.7.

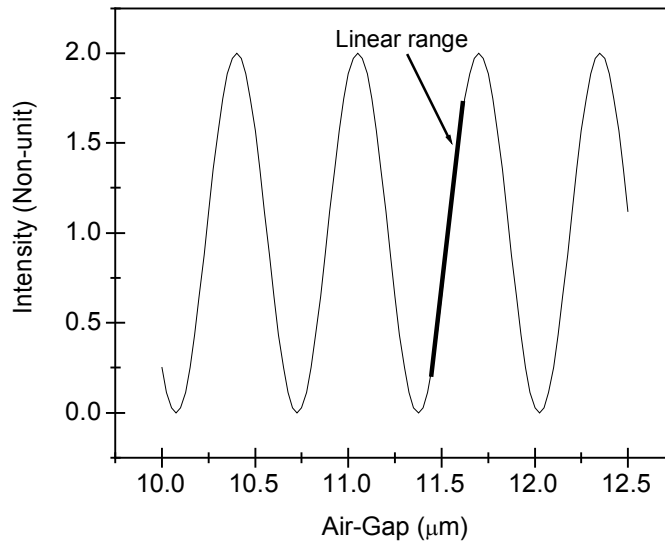


Fig. 3.7 Illustration of interference fringes versus sensor air-gap.

If the distance between the two end faces is less than the coherence length, L_c , of the optical source, the two reflections, R1 and R2, will produce interference fringes.

When an EFPI made of low-reflectivity mirrors is illuminated by a monochromatic light source, the response is a periodic function similar to two-beam interferometer which can be described by [43]

$$I = E_1^2 + E_2^2 + 2E_1E_2 \cos\left(\frac{4\pi nL}{\lambda}\right) \quad (3-5)$$

where E_1 and E_2 are the magnitudes of the electrical fields of the reflected light at two fiber ends, d is the length of the air gap of the Fabry-Perot cavity, λ is the wavelength, and n is the refractive index of the medium. When $E_1 \approx E_2$ and assuming $I_1 = E_1^2$, Eq. (3-5) can be simplified as:

$$I = 2E_1^2 \left(1 + \cos\left(\frac{4\pi n d}{\lambda}\right)\right) = 2I_1 \left(1 + \cos\left(\frac{4\pi n d}{\lambda}\right)\right) \quad (3-6)$$

According to Eq. (3-6), the interference signal from an EFPI is a function of the cavity length and refractive index of the medium inside the Fabry-Perot cavity. By detecting the change of the interference fringes, extrinsic Fabry-Perot interferometers can work as sensors to detect many physical parameters such as temperature [48, 49], strain [50, 51], pressure [32, 52], vibration [53], and flow [54, 55].

If an LED or fixed wavelength source with a narrow bandwidth is used as the light source of the F-P sensor, the initial air-gap control is very important. Depending upon the application requirements, in order to optimize the sensor's performance, it is necessary to set the initial air-gap value so that the initial operating point is at the beginning of the linear range or in the middle of it.

$$\phi = \frac{2\pi L}{\lambda} + \pi = \pi\left(\frac{2L}{\lambda} + 1\right) \quad (3-7)$$

$$\phi_{opt} = \frac{1}{2}(2k+1)\pi, \quad k \in N$$

For work point set in middle: $L_{ini} = \frac{2k-1}{8}\lambda_0$, $k \in N$ and λ_0 is in microns.

For work point set at the start: $L_{ini} =$, $k \in N$ and λ_0 is in microns.

For a sensor with good visibility, the sensor output is very sensitive to air-gap changes as shown in Fig. 3.8

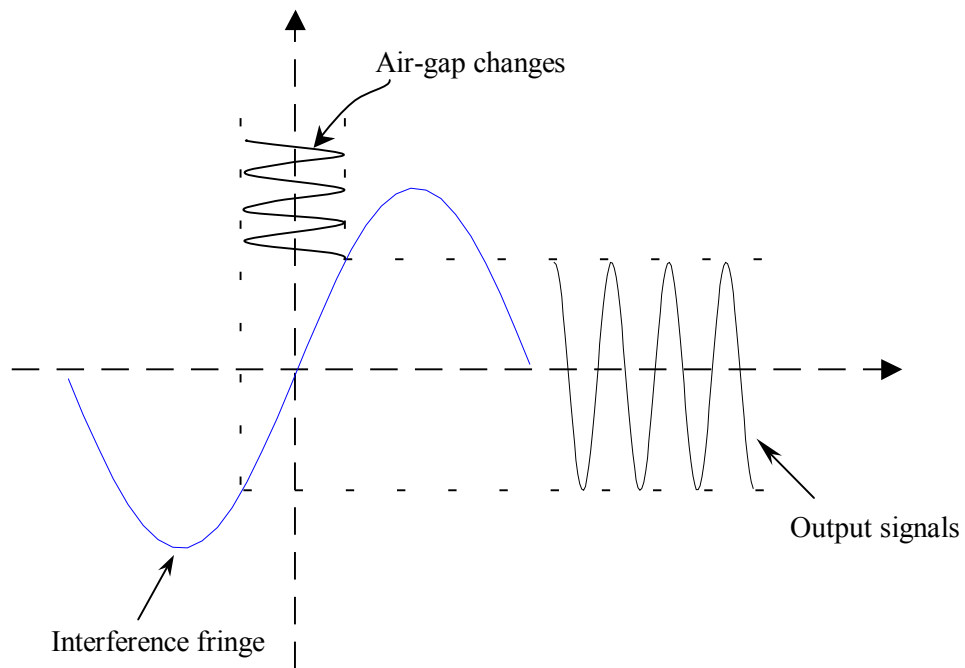


Fig. 3.8 Illustration of a linear operating range of the sensor response curve

3.3 Diaphragm mechanical analysis

Diaphragm mechanical analysis will focus on diaphragm deflection under static and dynamic pressure. The diaphragm deflection sensitivity and frequency response are the two most important parameters.

3.3.1 Diaphragm deflection under pressure

A round diaphragm clamped rigidly at its edges is shown in Fig. 3.9. The diaphragm will be deflected under a uniform pressure P . The out-of-plane deflection of the diaphragm y is a function of the pressure difference and the radial distance [56]:

$$y = \frac{3(1-\mu^2)P}{16Eh^3}(a^2 - r^2)^2 \quad (3-8)$$

where y = deflection

P = pressure

h = diaphragm thickness

a = effective diaphragm radius

E = Young's Modulus

r = radial distance

μ = Poisson's Ratio

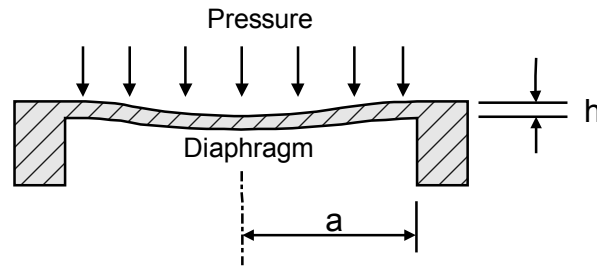


Fig. 3.9 Structure model for the diaphragm

Usually, we define the ratio between the deflection and the pressure difference as the diaphragm pressure sensitivity (Y). When the optical fiber is positioned to face the center of the diaphragm, only the center deflection y_c is of interest, and Y_c (for fused silica material at 25°C) is given by [57]

$$Y_c = 1.71 \times 10^{-8} \frac{a^4}{h^3} (\mu\text{m/psi}), \quad (3-9)$$

where r and h are in microns.

Deflection curve under pressure

$$y = \frac{3(1-\mu^2)P}{16Eh^3} a^4 \left[1 - \left(\frac{r}{a} \right)^2 \right]^2 = y_{\max} \left[1 - \left(\frac{r}{a} \right)^2 \right]^2 \quad (3-10)$$

For a circular diaphragm, the deflection varies from zero at the edges to the maximum value at its center as shown in Fig. 3.10. A 3D simulation performed by Matlab is shown in Fig. 3.11.

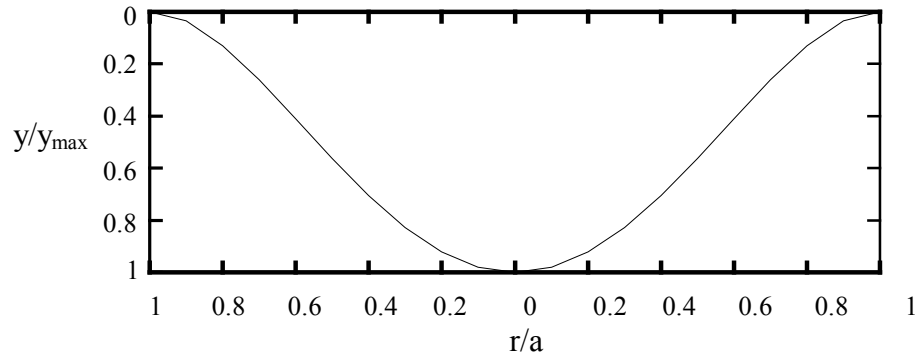


Fig. 3.10 Deflection curve of the diaphragm under pressure

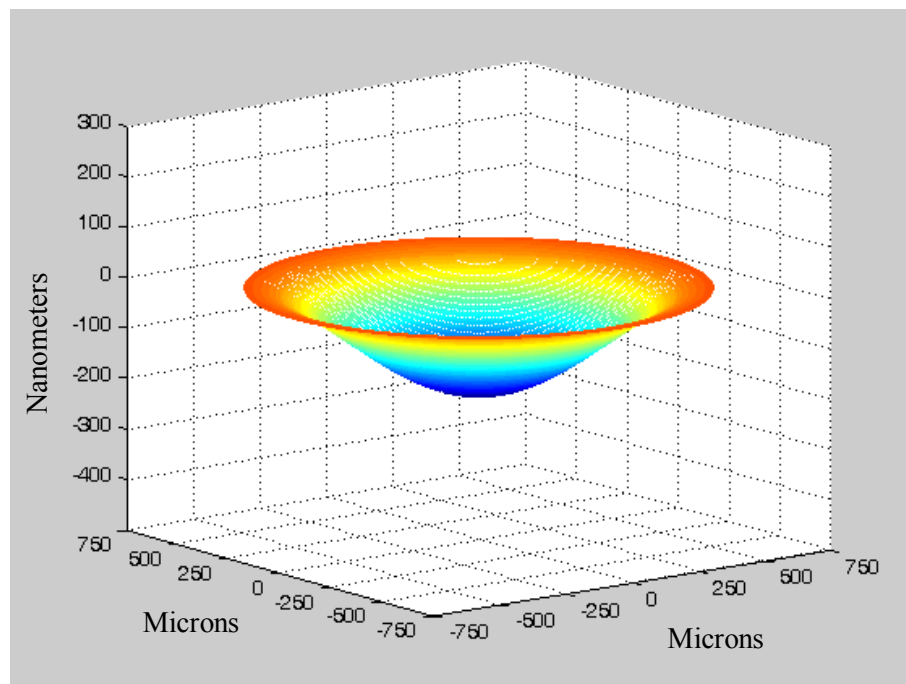


Fig. 3.11 Simulation of the diaphragm deflection by using Matlab

The equations discussed above are valid only when the deflection is no more than 30% of the thickness of the diaphragm [56], which means $y_{\max} < 0.3h$. The diaphragm diameter is generally determined by measurement requirements such as installation

spaces. Therefore, when the diaphragm diameter is selected and the pressure measurement range is known, the minimum thickness of the diaphragm is given by Eq. (3-11), which will lead to the highest sensitivity. Fig. 3.13 and Fig. 3.12 show the relation between h_{\min} and P_{\max} .

$$h_{\min} = r \left(5(1 - \mu^2) P_{\max} / 8E \right)^{\frac{1}{4}} \quad (3-11)$$

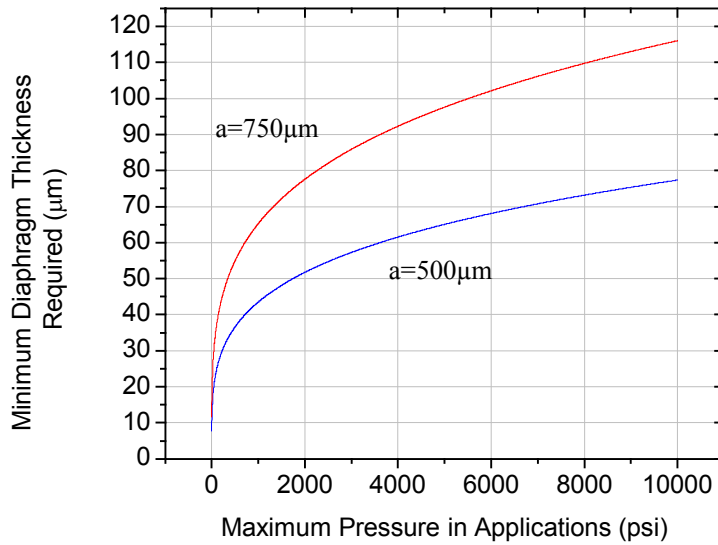


Fig. 3.12 Required diaphragm thickness vs. Maximum pressure (0-10kpsi)

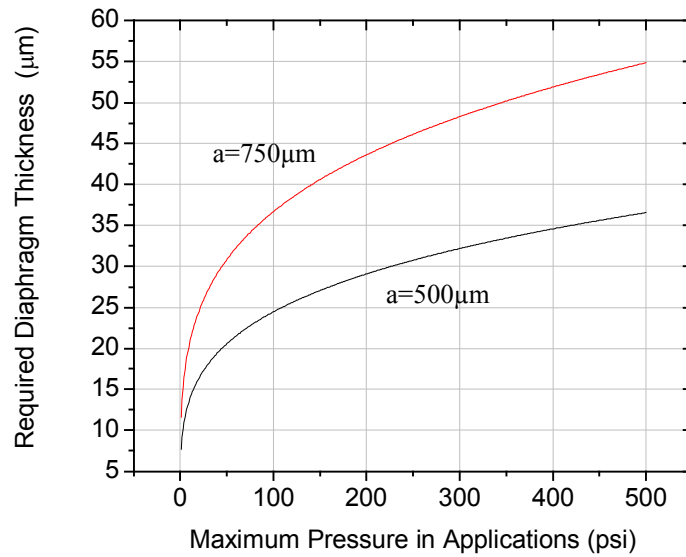


Fig. 3.13 Required diaphragm thickness vs. Maximum pressure (0-500psi)

The relationships between pressure sensitivity and r and h are illustrated in Fig. 3.14.

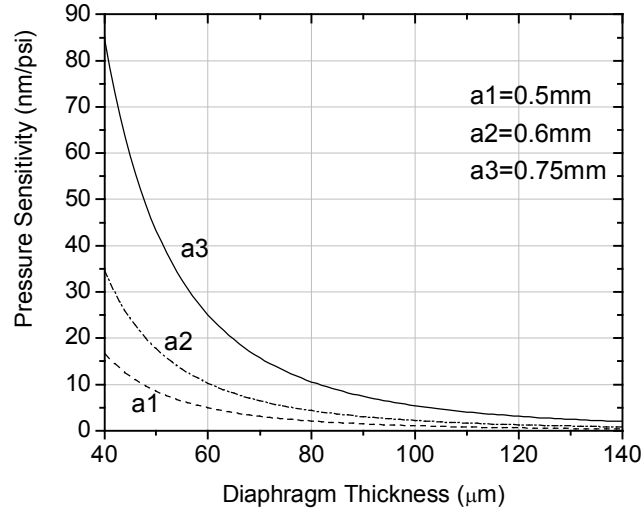


Fig. 3.14 Theoretical sensitivities of the sensor for different diaphragm radius values.

3.3.2 Diaphragm frequency response

In addition to the consideration of diaphragm sensitivity, diaphragm frequency response is another important issue. We define the diaphragm as a free vibrating circular plate clamped rigidly at the edge. Its natural frequency f_{mn} is expressed follows [56]:

$$f_{mn} = \frac{\alpha_{mn}}{4\pi} \sqrt{\frac{E}{3w(1-\mu^2)}} \left(\frac{h}{r^2} \right) \quad (3-12)$$

where α_{mn} is a constant related to the vibrating modes of the diaphragm

h is the thickness of the diaphragm

r is the effective diaphragm radius

w is mass density of the diaphragm material

μ is the Poisson's ratio

E is the Young's modulus of the diaphragm material

For the lowest natural frequency, $\alpha_{00} = 10.21$, and based on the properties of fused silica, the frequency response of the diaphragm can thus be calculated as follows [57]:

$$f_{00} = 2.742 \times 10^9 \frac{h}{r^2} \text{ (Hz)} \quad (3-13)$$

where h and r are in microns.

As indicated by Eq. (3-26), the sensor's frequency response in liquid is proportional to the thickness of the diaphragm and inversely proportional to the square of the effective diaphragm diameter. The relationships between frequency response and a and h are illustrated in Fig. 3.15.

In order to faithfully respond to these dynamic pressures, the sensor natural resonant frequency should be at least three to five times as high as the highest applied frequency. For example, to obtain a flat frequency response from DC to 50KHz, let $f_{00} > 250$ kHz. To obtain flat frequency response from DC to 150KHz, let $1000\text{kHz} > f_{00} > 500\text{kHz}$. The maximum usable frequency should be taken to be one fifth or one seventh of its natural frequency.

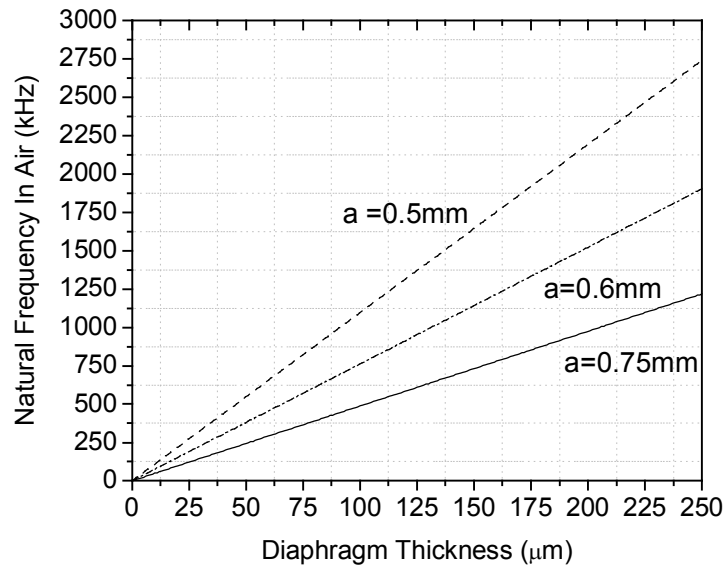


Fig. 3.15 Theoretical natural frequency of the sensor.

As indicated by Eq. (3-13) the sensor's frequency response is proportional to the thickness of the diaphragm and inversely proportional to the square of the effective diaphragm radius, which is in contradiction with the diaphragm sensitivity. Therefore, some tradeoff must be made in sensor design. We chose the diaphragm thickness $h=60\mu\text{m}$ and its effective radius $a=0.75\text{mm}$, so the calculated pressure sensitivity and natural resonant frequency are 25nm/psi and 292kHz, which meets the requirements.

Table 3.1. Typical properties of fused silica (25°C)

Parameter	Symbol	Value	Units
Density	ρ	2.2×10^3	kg/m^3
Young's Modulus	E	7.3×10^{10}	Pa
Poisson's Ratio	μ	0.17	—
Max. Tensile Stress	σ_m	$\sim 1.5 \times 10^9$	Pa
Coefficient of Thermal Expansion	α_T	$5.4\text{-}5.7 \times 10^{-6}$	$(^\circ\text{C})^{-1}$

Table 3.2 Values of constant α_{mn}

α_{mn}	n = 0	n = 1	n = 2
m = 0	10.21	21.22	34.84
m = 1	39.78	60.82	84.58
m = 2	88.90	120.12	153.76

For static pressure measurement, with a specified sensitivity, the larger diaphragm will lead a wider measurement range and a smaller stress.

For dynamic pressure measurement, the smaller the diaphragm, the higher the natural resonant frequency.

For measuring both of static and dynamic pressures, some tradeoffs must be made in sensor design. The following section will discuss the diaphragm dynamic properties in detail.

(1) Circular plate free vibration [58, 59]

Assuming there is no pressure on the surface of diaphragm, the equation of motion for free vibration is

$$D\nabla^2 y(r,\theta,t) + \rho h \frac{\partial^2 y(r,\theta,t)}{\partial t^2} = 0 \quad (3-14)$$

where h is thickness of plate (m), ρ stands for mass density, $y(r,\theta,t)$ is the displacement of vibrating diaphragm, ∇^2 is the operator $\nabla^2(*) = \frac{\partial^2(*)}{\partial r^2} + \frac{1}{r} \frac{\partial(*)}{\partial r} + \frac{1}{r^2} \frac{\partial^2(*)}{\partial \theta^2}$, and D is the flexural rigidity of the diaphragm defined by

$$D = \frac{Eh^3}{12(1-\mu^2)} \text{ (N/m}^2\text{)}. \quad (3-15)$$

where μ is the Poisson's ratio; E is the Young's modulus of the silica glass material.

Set $y(r,\theta,t) = Y(r,\theta)e^{j\omega t} = R(r)\Theta(\theta)e^{j\omega t}$, and $\lambda^4 = \frac{\rho h \omega^2}{D}$, the motion equation becomes:

$$\begin{aligned} \frac{d^2\Theta}{d\theta^2} + k^2\Theta &= 0 \\ \frac{d^2R}{dr^2} + \frac{1}{r} \frac{dR}{dr} + (\pm\lambda^2 - \frac{k^2}{r^2})R &= 0 \end{aligned} \quad (3-16)$$

For the first equation, we have the solution:

$$\Theta = A \cos(k\theta) + B \sin(k\theta) \quad k=0,1,2,3\dots \quad (3-17)$$

For the second equation, set $\varphi^2 = \pm\lambda r$ for $(\pm\lambda^2)$, and we get

$$\frac{d^2 R}{d\varphi^2} + \frac{1}{\varphi} \frac{dR}{d\varphi} + \left(1 - \frac{k^2}{\varphi^2}\right) R = 0 \quad (3-18)$$

The solution is Bessel functions. For $\varphi = \lambda r$, solution is Bessel functions of the first & second kind, $J_k(\varphi)$ and $I_k(\varphi)$; for $\varphi = j\lambda r$, the solution is modified Bessel functions of the first & second kind, $Y_k(\varphi)$ and $K_k(\varphi)$. So the total solution of the circular plate is,

$$R(\varphi) = C J_n(\varphi) + C' I_n(\varphi) + F Y_n(\varphi) + F' K_n(\varphi) \quad (3-19)$$

C , C' , F , and F' are constant for each solution components. For plate clamped at boundary, $F = F' = 0$, and

$$y(a, \theta, t) = 0$$

$$\frac{\partial y}{\partial r}(a, \theta, t) = 0$$

we have $R(a) = 0$ and $\frac{dR}{dr}(a) = 0$

$$\begin{bmatrix} J_n(\varphi) & I_n(\varphi) \\ \frac{dJ_n(\varphi)}{dr} & \frac{dI_n(\varphi)}{dr} \end{bmatrix} \begin{pmatrix} C \\ C' \end{pmatrix} = 0 \quad (3-20)$$

then

$$J_n(\varphi) \frac{dI_n(\varphi)}{dr} - \frac{dJ_n(\varphi)}{dr} I_n(\varphi) = 0 \quad (3-21)$$

Searching this equation for its roots λa , labeled successively $m=0,1,2,\dots$ for each $n=0,1,2,\dots$, gives the natural frequencies. Values of the roots $\varphi_{mn}=(\lambda a)_{mn}$ are collected in Table 3.3. The natural frequencies are related to these roots by

$$\omega_{mn} = \frac{\varphi_{mn}^2}{a^2} \sqrt{\frac{D}{\rho h}} \quad (3-22)$$

and the mode-shape can be expressed

$$Y(r, \theta) = A \left[J_n(\lambda r) - \frac{J_n(\lambda a)}{I_n(\lambda a)} I_n(\lambda r) \right] \cos n(\theta - \phi) \quad (3-23)$$

Table 3.3 Value of $\varphi_{mn}=(\lambda a)_{mn}$

m \ n	0	1	2	3
0	3.196	4.611	5.906	7.143
1	6.306	7.799	9.197	10.537
2	9.44	10.958	12.402	13.795
3	12.577	14.108	15.579	17.005

From the properties of fused silica shown in Table 3.1, the frequency response of the sensor can thus be calculated by combining Eq. (3-15) and (3-22) into the following

$$f_{mn} = 2.742 \times 10^9 \times \frac{\varphi_{mn}^2}{\varphi_{00}^2} \frac{h}{a^2} \text{ (Hz)} \quad (3-24)$$

where $\varphi_{mn}=(\lambda a)_{mn}$, h and a are in microns.

If a plate is immersed in a fluid, its natural frequencies may be considerably altered. In order to take the mass of the fluid into account for the fundamental mode of vibration, Eq. (3-22) should be replaced by,

$$\omega_{mn}^l = \frac{1}{\sqrt{1+\beta}} \omega_{mn} = C \omega_{mn} \quad (3-25)$$

in which

$$C = \frac{1}{\sqrt{1+\beta}}, \text{ and } \beta = 0.6689 \frac{\rho_1}{\rho} \frac{a}{h}$$

where (ρ_1/ρ) is the ration of mass density of the fluid to that of the material of the plate.

$$f_{mn}^l = C \times 2.742 \times 10^9 \times \frac{h}{a^2} \quad (3-26)$$

For example, considering a sensor with $a=1.4$ mm and $h=125$ μm immersed in water ($\rho_w=1.0 \times 10^3$ kg/m³) and transformer oil ($\rho_{oil} \sim 0.9 \times 10^3$ kg/m³), which have $C_w=0.48$ and $C_{oil}=0.50$. The frequency response of the sensor will be lowered to 0.48 and 0.50 times its original value in air, respectively.

(2) Forced vibration of the clamped circular diaphragm

According to the Eq. (3-8), when a circular plate with clamped edges is under uniformly static pressure, the maximum displacement (y_{\max}) is expressed as the following.

$$y_{\max} = \frac{3(1-\mu^2)P}{16Eh^3} \times a^4 \quad (3-27)$$

Considering a plate is under a load varying harmonically with time, the equation of motion is

$$D\nabla^2 y + \rho h \frac{\partial^2 y}{\partial t^2} + \nu \frac{\partial y}{\partial t} = p e^{i\omega t} \quad (3-28)$$

in which ν is the damping coefficient of the liquid, ω_f is the frequency of varying pressure, and p is the amplitude of varying pressure. Set

$$\omega^2 = \frac{D}{\rho h}, 2\xi = \frac{\nu}{\rho h}, p = \frac{P}{\rho h}$$

then the solution of Eq.(3-27) is

$$y = e^{-\xi t} (A' \sin \omega_f t + B' \cos \omega_f t) - \frac{2\omega_f p \xi}{(\omega_{mn}^2 - \omega_f^2)^2 + 4\omega_f^2 \xi^2} \cos(\omega_f t) + \frac{p(\omega^2 - \omega_f^2)}{(\omega_{mn}^2 - \omega_f^2)^2 + 4\omega_f^2 \xi^2} \sin(\omega_f t) \quad (3-29)$$

where $\omega_1^2 = \omega_{mn}^2 - \xi^2$, and ω_{mn} is the natural frequency defined by Eq. (3-22) in the air and Eq. (3-25) in the liquid.

It is obvious that the ω_l components will vanish after long enough time, so the response of plate will be harmonic with the frequency of acoustic pressure but lagging behind by a phase ϕ_k :

$$y = \Sigma \sin(\omega_f t - \phi_k), \quad (3-30)$$

where $\tan \phi_k = \frac{2\omega_f \xi}{\omega_{mn}^2 - \omega_f^2}$, and Σ is the intensity modulation factor that is defined as

$$\Sigma = \frac{p}{\sqrt{(\omega_{mn}^2 - \omega_f^2)^2 + 4\omega_f^2 \xi^2}}. \quad (3-31)$$

This means that the intensity will resonate at the natural vibration frequency of the diaphragm. We define Q_{mn} as the enhancement coefficient of each vibration mode,

$$Q_{mn} = \frac{\Sigma_{force}}{\Sigma_{no-force}} = \frac{\omega_{mn}^2}{\sqrt{(\omega_{mn}^2 - \omega_f^2)^2 + 4\omega_f^2 \xi^2}}. \quad (3-32)$$

Considering the maximum diaphragm displacement occurs when the frequency is 0 (static case), the vibration response of diaphragm at the central point is:

$$y_{mn}(\omega_f) = y_{\max} \times Q_{mn}(\omega_f) = \frac{3p(1-\mu^2)}{16Eh^3} a^4 \frac{\omega_{mn}^2}{\sqrt{(\omega_{mn}^2 - \omega_f^2)^2 + 4\omega_f^2 \xi^2}}. \quad (3-33)$$

Fig. 3.16 shows a typical sensor frequency response around its fundamental natural frequency with $\xi \approx 0$. In this case, the sensor has a diaphragm with 60 μ m in thickness, 1300 μ m in diameter. Its natural frequency in air is $f_{00} = 389$ kHz.

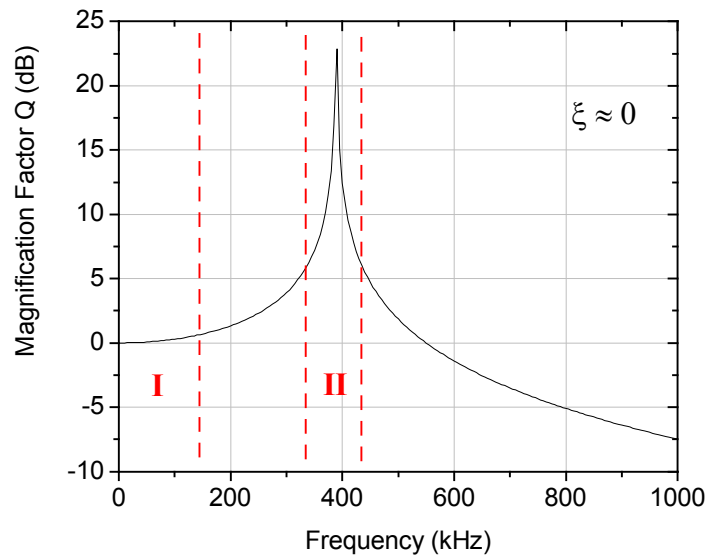


Fig. 3.16 Sensor frequency response with fundamental mode

In order to ensure the sensor operates in the linear range, where the vibration amplitude of diaphragm is proportional to the pressure of acoustic waves, the fundamental natural frequency of the sensor should be at least 3 times larger than the working frequency of acoustic pressure. This kind of sensor is called a broadband sensor, which works in Zone I shown in Fig. 3.16. In frequency Zone I, the frequency response of sensor would be maintained relative ‘flat’. Obviously, the intensity is enhanced more than 100 times around 389 kHz due to the resonance. Therefore, if a designed sensor has fundamental nature frequencies close to the frequency of detected acoustic wave, the sensor would provide ultra-high sensitivity, and be called a narrowband sensor. However, since the narrowband sensor works in the nonlinear range (Zone II) of the diaphragm vibration, it is not straightforward to quantitatively predict the acoustic intensity from the diaphragm deformation.

According to these results, we have several conclusions:

- 1) When the natural frequency is close to the acoustic frequency, the vibration will be magnified and the frequency response is no longer flat, but it is where a sensor with

very high sensitivity can be designed (narrowband sensor). The vibration can be expressed as:

$$y_{mn}(\omega_f) = \frac{3p(1-\mu^2)}{16Eh^3} a^4 \frac{\omega_{mn}^2}{2\omega_f \xi} \quad (3-34)$$

2) To maintain a flat sensor frequency response in the operating frequency range (broadband sensor), the fundamental natural frequency of the sensor should be at least 3 times the working frequency of dynamic acoustic pressure.

3.3.3 Stress Analysis

Stress analysis is useful for predicting the failure of a diaphragm under pressure. There are no stresses in the medial plane of the diaphragm at small deflections. But the bending stresses increase linearly over the thickness of the diaphragm to the outer surfaces where they reach their maximum values. Because the diaphragm is bent into a doubly curved surface, the stress analysis must take into account the radial and tangential stresses, which vary along the radius of the diaphragm. The stress-deflection relationship is shown in Eq. (3-35).

$$\sigma_{rm} = \pm \frac{3}{8} P \frac{a^2}{h^2} \left[(3 + \mu) \frac{r^2}{a^2} - (1 + \mu) \right] \quad (3-35)$$

The tangential stress at any radial distance may be calculated from the expression:

$$\sigma_{rm} = \pm \frac{3}{8} P \frac{a^2}{h^2} \left[(1 + 3\mu) \frac{r^2}{a^2} - (1 + \mu) \right] \quad (3-36)$$

The maximum value for the radial stress and tangential stress is at the edge and the center respectively as shown in Fig. 3.17. The maximum radial stress is at the edge and is:

$$\sigma_{r,m} = \pm \frac{3}{4} P \frac{r^2}{h^2} \quad (3-37)$$

Since $\mu < 1$, the maximum tangential stress is at the center ($r = 0$) and is

$$\sigma_{t,m} = \pm \frac{3}{8} (1 + \mu) P \frac{r^2}{h^2} \quad (3-38)$$

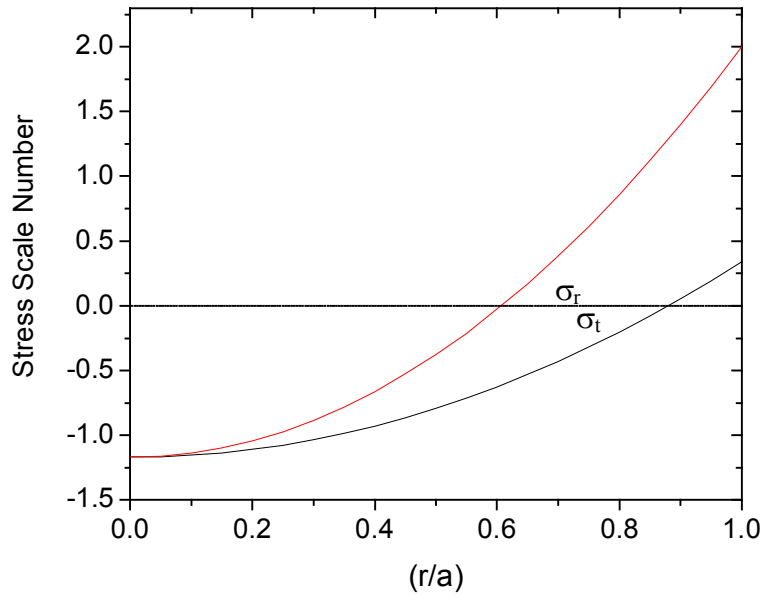


Fig. 3.17 Radial and tangential stresses of a round silica diaphragm

Based on the previous discussion, it is clear that for the same pressure sensitivity, the smaller the diaphragm the higher the stress.

3.3.4 Single mode EFPI sensor

In this research, we decided to fabricate a single mode diaphragm-based EFPI sensor. There are several reasons for us to use single mode fiber.

From the view of sensor fabrication, if a multimode fiber is used, there is more than one mode reflected from the diaphragm. If the mode reflected from the diaphragm

doesn't activate the original mode, the interference fringe visibility will decrease. This property makes the sensor fabrication more difficult. From the signal detection standpoint, for a SCIIB system, there is no big difference between the use of single mode and multimode fibers, but single mode fiber components, such as long wavelength filters, are more readily available because of the development of single mode fiber communications.

From the view of measurement capability, the light source for the single mode fiber system has a narrower spectral width. So the single mode fiber system has a greater coherence length, which can be seen from Eq. (3-39). This property provides much larger dynamic range for pressure testing.

$$L_c \approx \frac{\lambda_c^2}{\Delta\lambda} \quad (3-39)$$

where λ_c is the central wavelength of the source and $\Delta\lambda$ is the spectral width of the source.

For future practical use, single mode fiber as a transmission line has less transmission loss compared with multimode fiber. So the sensors made from single mode fiber can be used for long-distance sensing applications.

Chapter 4 Fabrication of the Diaphragm Based Fiber Optic Sensors

The sensor performance highly depends on its fabrication quality. The detailed research work on sensor fabrication will be described in this chapter.

4.1 Sensor material selection

Material selection is very important in sensor development. The sensor performance will greatly be affected by the material properties such as mechanical strength, coefficient of thermal expansion (CTE), melting or softening point, thermal conductivity etc. We here investigate several common materials including crystalline and noncrystalline materials.

4.1.1 Metals

Metals are widely used as sensing elements in sensor fabrication such as diaphragms, membranes and bellows. The most commonly used metals are aluminum, copper, stainless steel, and Kovar. Compared with ceramics and glasses, they are easier to machine and handle. Their properties are listed in Table. 4.1

Table. 4.1 Properties of several common metals

Properties Metals	Melting Point (°C)	CTE	Young's Modulus	Poisson's Ratio
Aluminum	660	$\sim 25 \times 10^{-6}$	68.9GPa	0.33
Copper	1083	$16 \sim 25 \times 10^{-6}$	110GPa	0.343
Stainless Steel	1371-1454	$9 \sim 20 \times 10^{-6}$	190~210GPa	0.27~0.3
Kovar	1450	$5.1 \sim 11 \times 10^{-6}$	138GPa	0.317

4.1.2 Ceramics

Common ceramics such as alumina, sapphire, zirconia and SiC are widely used in industrial applications especially for harsh environment with high temperature, high pressure or corrosion chemicals. However, they are generally expensive and hard to machine. Table 4.2 lists some of their properties.

Table 4.2 Properties of several common ceramics

Properties Ceramics	Melting Point (°C)	CTE	Young's Modulus	Poisson's Ratio	Thermal conductivity (Wm ⁻¹ K)	Thermal shock resistance
Alumina	2100	$\sim 8 \times 10^{-6}$	~ 300 Gpa	~ 0.22	25 at 20°C ~ 5.7 at 800(°C)	Good
Sapphire	2040	$\sim 8.4 \times 10^{-6}$	345GPa	0.29	0.04	Poor
Zirconia	2700	$\sim 10 \times 10^{-6}$	200~360GPa	0.23~0.3	2.0	Fair
SiC	~ 2700	4.0	410GPa	0.14	120	Excellent
Mullite	~ 1900	$\sim 5 \times 10^{-6}$	130GPa	~ 0.25	~ 5.0	Very Good

4.1.3 Glass

Common commercial glasses are products of melting of crystalline materials at elevated temperatures to produce liquids which have been subsequently been cooled to rigid solid without crystallization. Silica is the most important constituent in the glass composition. Most commonly used glasses are fused silica, fused quartz, borosilicate and soda lime. Compared to crystals, glass is easy to be manufactured with different sizes from thin optical fiber to large windshields. Table 4.3 lists some properties of these glasses.

Since metals and ceramics have much different CTEs than regular optical fibers, the thermal expansion mismatch will introduce high stresses that may lead to a sensor failure.

Table 4.3 Properties of several common glasses

Properties Glass	Softening Point (°C)	CTE (0-300°C)	Young's Modulus	Poisson's Ratio	Thermal conductivity (Wm ⁻¹ K)	Thermal shock resistance
Fused Silica	~1600	5.5×10^{-7}	73GPa	0.17	~1.4	Excellent
Fused Quartz	~1600	5.5×10^{-7}	73GPa	0.17	~1.4	Excellent
Borosilicate	~720	$3.3 \sim 5.0 \times 10^{-6}$	64GPa	0.20	~1.1	Good
Soda Lime	~690	9.3×10^{-6}	70GPa	0.22	~0.937	Poor

After the investigation of many materials, we decided to choose fused silica (fused quartz), the same material as telecommunications optical fiber to construct the sensing elements. More detailed properties of this material are presented here.

Fused Silica or Fused Quartz (Silicon Dioxide)

Fused silica is produced by melting high purity silica or crystal quartz at extremely high temperatures in an electric arc furnace or resistance furnace. It can be solidified and annealed without crystallizing due to its extremely high viscosity. However, it will devitrify at temperatures over 1100°C. Fused silica (or quartz) is an amorphous material, characterized by its extremely low coefficient of thermal expansion (CTE) and resistance to thermal shock. Its CTE is 1/34 that of copper and only 1/7 that of borosilicate glass. This makes the material particularly useful for optical flats, mirrors, furnace windows and critical optical applications, which require minimum sensitivity to thermal changes. We summary the advantages of fused silica or quartz here:

Key Properties:

Lowest coefficient of thermal expansion of any known material

High resistance to thermal shock

Low thermal conductivity

Excellent electrical insulation up to approximately 1000°C

Excellent resistance to corrosion from molten metals and glass

Low dielectric constant

Low dielectric loss

Good UV transparency

Easily machined to tight tolerances

Dissolves in hydrofluoric acid (HF) allowing wet etching

4.2 Sensor fabrication requirements

1. Hermetically bonding the diaphragm to the ferrule with high mechanical strength.
2. Hermetically bonding the fiber to the ferrule with good mechanical strength.
3. The sensor gauge length and cavity length must be controlled to precisely set the initial operating point and also realize the best thermal stability .
4. The fabrication process should be automatic or semiautomatic to achieve predictable and repeatable performance at a low cost.
5. The sensor probe needs to be packaged to improve its mechanical strength and is easily handled and installation in applications.

4.3 Basic sensor fabrication system

Fig. 4.1 shows the basic fiber sensor fabrication system, which can be divided into two subsystems, 1) Sensor bonding sub-system; 2) Sensor F-P cavity length and signal quality monitoring sub-system.

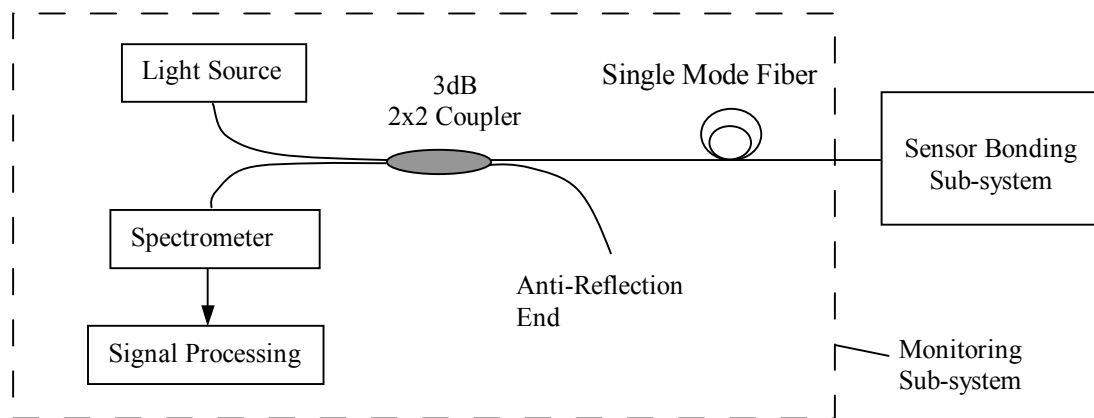


Fig. 4.1 Schematic of fiber optic sensor fabrication system.

4.4 Research for sensor bonding methods

A variety of bonding methods have been used in fiber optic sensor fabrication in the past two decades. In general, they are classified as adhesive bonding or interlayer free bonding. Several typical bonding techniques have been investigated.

4.4.1 Epoxy bonding

Epoxy is a widely used adhesive to bond parts together in fiber optic sensor fabrication [10, 11]. For a diaphragm-based pressure sensor, the wafer and the fiber must be hermetically bonded with the ferrule. We tried epoxy 907 (Miller-Stephenson) to bond the sensor as shown in Fig. 4.2. The ferrule and diaphragm must be fixed and the fiber was adjusted to obtain the desired air-gap before epoxy is applied. Since epoxy 907 needs about 2 hours to cure, this bonding process is time consuming. And the sensor repeatability is not good because the air-gap will change during the epoxy curing. In addition, epoxy undergoes viscoelastic creep and can not survive at high temperature, for instance, the service temperature of epoxy 907 is limited below 82°C).

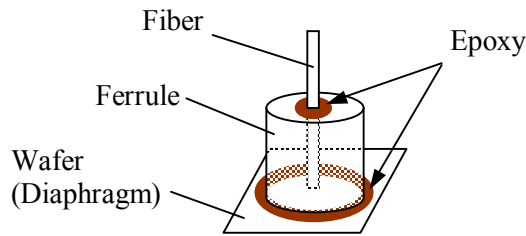


Fig. 4.2 Epoxy bonding in the fiber sensor fabrication

4.4.2 Glass solder/powder bonding

Glass solders are widely used in various hermetic seals, i.e., helium leak-proof, semiconductor packages [60-62]. The solder glass preform was baked at a temperature about 400°C and became liquid filling the bonding area and realizing a solid hermetic

seal when the temperature drops. A fiber to ferrule bond is shown in Fig. 4.3 Since the bonding temperature is relative low compared with the melting point of fused silica, no physical damage was observed to the fiber and ferrule.

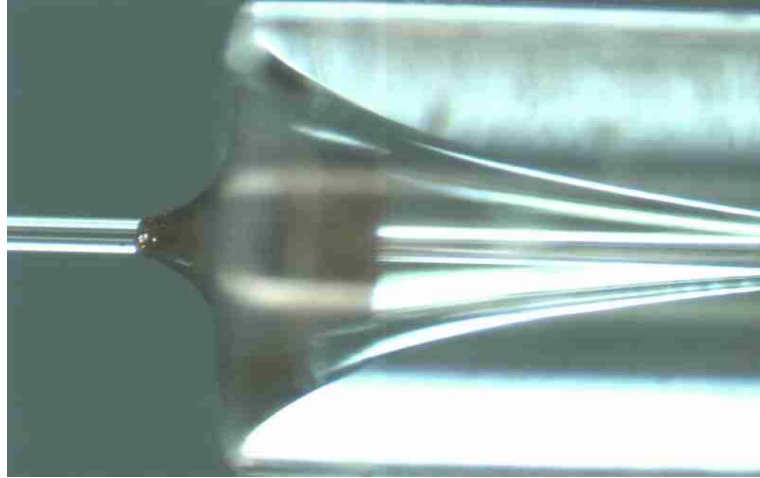


Fig. 4.3 A fiber was bonded with a ferrule by glass solder.

Although the bonding process is simple and fast, it has some drawbacks and limitations. Evidently, the low softening point of the solder glass limits its application below 400°C and the CTE mismatch between the solder glass and fused silica will introduce large stresses, which may lead to a failure. In addition, the diaphragm to ferrule bonding is difficult to accomplished by glass soldering method because the flowing solder can easily fill the sensor F-P cavity blocking the optical path.

4.4.3 Direct bonding

The direct-bond method [63] relies on forces that naturally attract surfaces together when they are very smooth and flat. A range of mechanisms has been proposed to explain this initial contact attractive force. It is well known that smooth metal surfaces, if atomically clean, will bond together. This process is often referred to as “cold welding” and is typically achieved by cleaning and bringing the metal surfaces into contact in a vacuum to maintain cleanliness. This bond usually relies on plastic deformation of the metal to bring the atoms in close contact. Most direct bonding

demonstrated for microstructures requires some surface treatment (e.g., hydration, oxygen plasma exposure) prior to contact to promote the surface attraction and bonding process. This is sometimes assisted by modest pressure to expel air from between the wafers and to initiate the contact. Bonding is usually followed by a thermal cycle, which increases the strength of the bond. The bonding is done by applying pressure at high temperature. In most cases room temperature bonding fails or results in a poor yield because of the wafer roughness. In one word, the direct bonding process is so expensive and time consuming that should be chosen only if other bonding methods are difficult to apply or do not meet the application requirements.

4.4.4 Anodic bonding

Anodic bonding is quite popular in making fiber sensors [12, 13] since it can bond sodium-rich glass to silicon or most metals with good adhesion strength. Also the process can be done moderate temperatures. However, it is well known that this process will introduce thermal stress due to mismatch of coefficients of thermal expansion between glass and silicon (or metal). Although anodic bonding is adhesive free bonding, it cannot be used for bonding fused silica glass, which has a higher softening point and much lower CTE than other glass and is the most compatible material to silica optical fiber.

4.4.5 Sol-gel bonding

A drop of sol-gel was put on the surface of the fiber and the fiber was inserted into the ferrule. When the air-gap adjustment was done, a CO₂ laser was used to heat the ferrule at low power for about 30 seconds, which solidified the sol-gel and bonded the fiber within the ferrule as shown in Fig. 4.4. Any other heating methods can be used to solidify the sol-gel such as a furnace or a hot plate. In general, since the heating time is short, the solidified sol-gel is porous as shown in Fig. 4.4. It is not easy to control the solidification of the sol-gel to realize a hermetic seal, which may involve pressurizing and vacuumizing. Therefore, the sol-gel bonding is typically just for fixation.

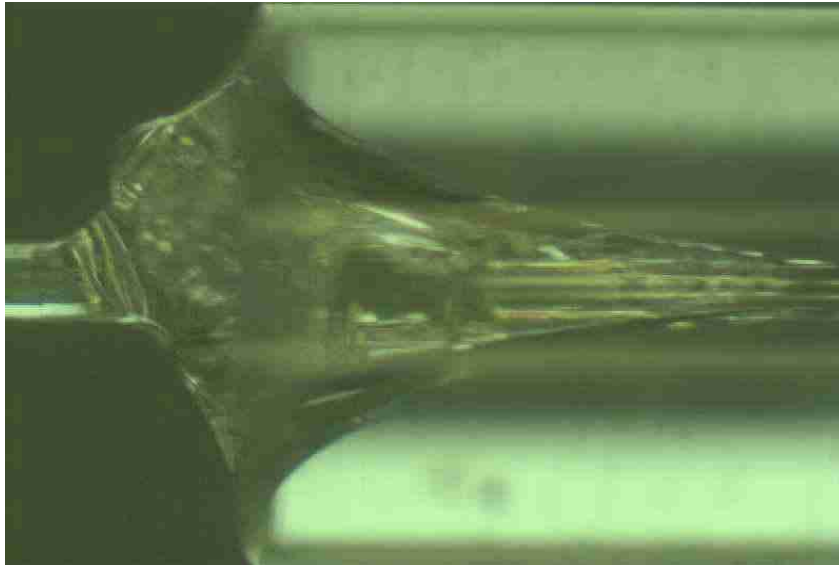


Fig. 4.4 Bonding fiber with ferrule with sol-gel

4.5 Laser fusion bonding

The best way to joint two parts is to bond them without introducing foreign materials, which will degrade the structure by thermal expansion stresses. Glass fusion is a common technique used in industry or art applications [52, 64]. However, in miniature fiber optic fabrication, thermal glass fusion bonding encountered tremendous technical problems due to the critical requirements. These include high quality diaphragm alignment and good surface reflectivity, which can be degraded or damaged easily during high temperature process. Also the light transmission inside the fiber should not change after the bonding.

We proposed and implemented a laser-induced fusion bonding method for fabricating the miniature diaphragm based fiber optic engine pressure sensor. We chose a CO₂ laser to thermally bond the sensor parts because the fused silica has a high absorption coefficient at 10.6 μm as shown in Fig. 4.5 [65].

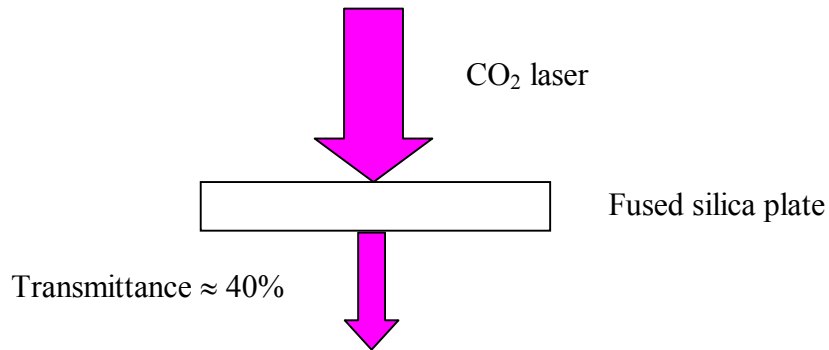


Fig. 4.5 Transmittance of a fused silica glass plate

4.5.1 Sensor parts preparation

Alignment Ferrules

In order to obtain good interference signals, the fiber and the diaphragm must be maintained in a good alignment. This requires that the inner diameter (I.D.) of the ferrule can only be slightly larger than the diameter of fiber cladding (125 μm). Therefore, we chose the inner diameter of the ferrule to be 127~129 μm . In order to provide a space for the bonding of the ferrule to the diaphragm, the outer diameter of the ferrule must be greater than 1mm. Therefore, we choose the outer diameter of the ferrule to be 1.8mm.

Diaphragm Wafer Preparation

A one-inch square commercially available single side (or double side) polished fused silica wafer (60~250 μm) was diced into 1.9mm square pieces. It is more expensive to dice the wafer into round pieces because regular wafer dicing machines can dice only by straight lines.

4.5.2 Laser Bonding System

Diagrams of the laser bonding system and sensor holding fixture are shown in Fig. 4.6 and Fig. 4.7. Photos of sensor fabrication system are shown in Fig. 4.8 and Fig. 4.9.

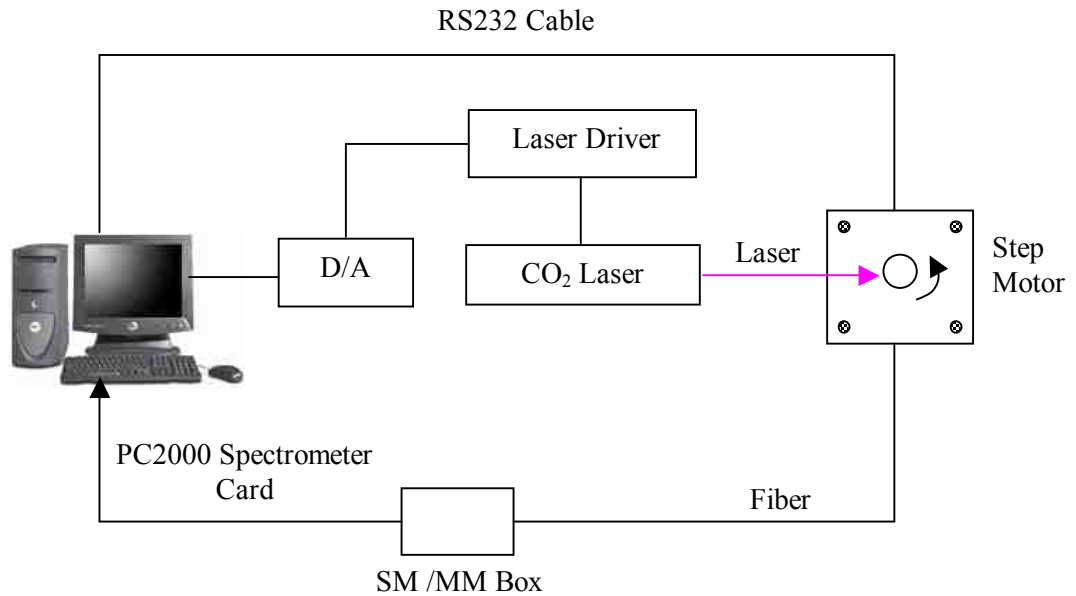


Fig. 4.6 Automated laser bonding pressure sensor fabrication system

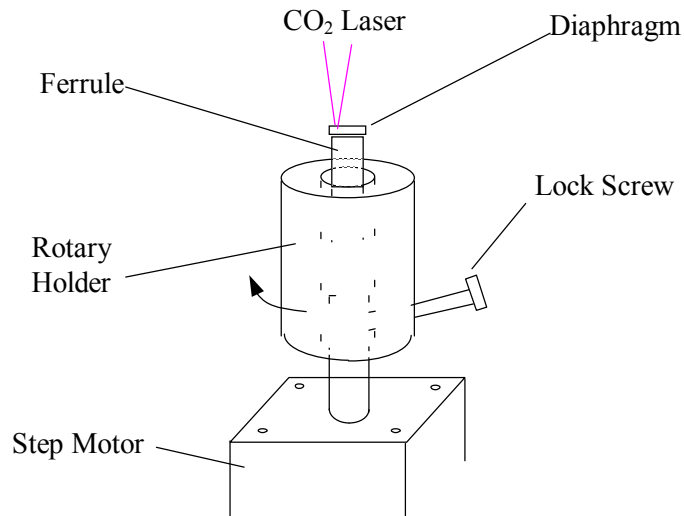


Fig. 4.7 Schematic of the diaphragm to ferrule laser bonding

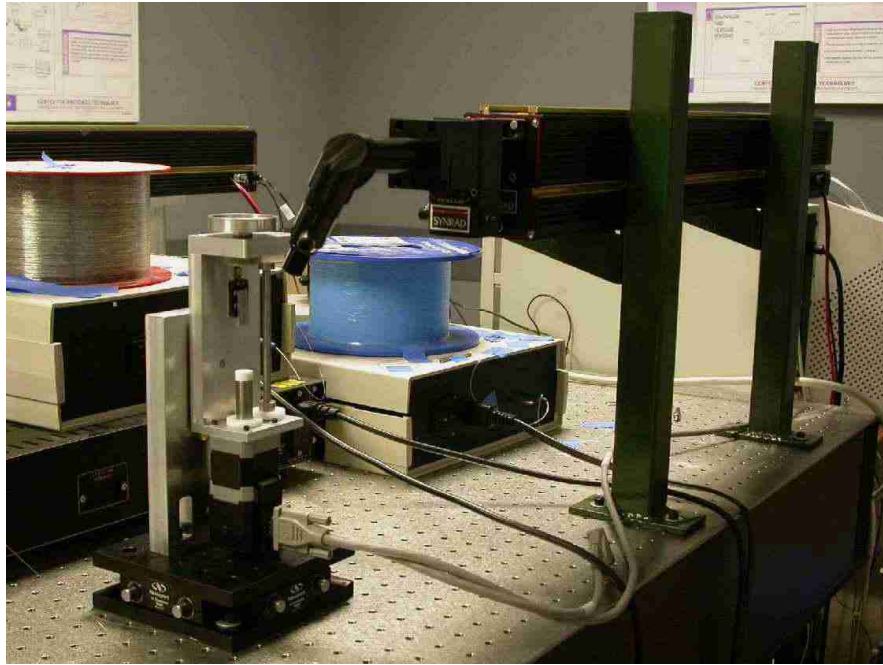


Fig. 4.8 Photo of the automated laser bonding pressure sensor fabrication system



Fig. 4.9 Photo of the sensor laser bonding fixture

High performance diaphragm based epoxy free pressure sensors can be fabricated by using the developed controlled laser thermal bonding technology and sensor fabrication system.

The diaphragm thickness range can be $50\mu\text{m}$ to $500\mu\text{m}$ and the circular bonding diameter can be set from 0.8mm up to several inches, which provides excellent flexibility in sensor system design and fabrication.

The structure of the pressure sensor is shown in Fig. 4.10. The length of the F-P cavity (air-gap) will decrease with deflection of the diaphragm as a result of the applied pressure. Light is injected into the optical fiber and reflected partially (4%) by the end face of the fiber and the inside surface of the diaphragm. Then the two reflections propagate back through the same fiber and generate interference fringes, which are demodulated to determine the air-gap thickness.

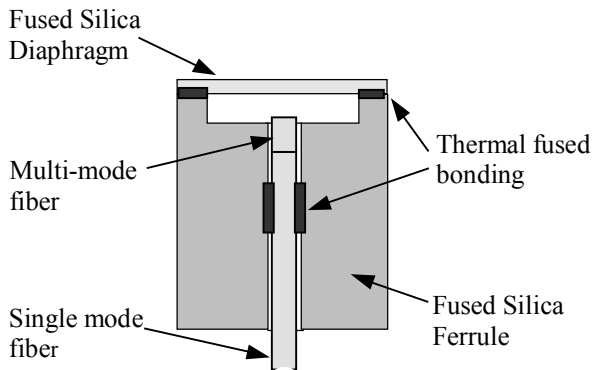


Fig. 4.10 Structure of the optical fiber pressure sensor.

The temperature dependence of the pressure sensors is the main factor contributing to pressure measurement errors. Therefore, designing the pressure sensor such that it has a minimum cross-sensitivity to temperature is an important consideration.

4.5.3 Fabrication process

A pit with a diameter of approximately 1.5mm was formed in one end of the 1.8mm O.D. silica glass ferrule by mechanically machining the ferrule. A 125 μ m thick silica wafer was attached to the ferrule top by a circular laser-induced thermal fusion hermetic bond. Since the wafer was heated locally by the laser at the edges, the wafer surface near the center was not affected, even when coated with a metal reflective film. The square shaped wafer was rounded after laser welding, which is tightly ruggedized and is convenient for installation. A single mode fiber spliced with a piece of multi-mode fiber was inserted in the central bore of the ferrule. Part of the cladding of the single mode fiber was fusion bonded with the ferrule to realize a hermetic seal. The multi-mode fiber (≈ 0.5 mm) and part of the single mode fiber (≈ 2 mm) were free to expand or shrink when the temperature changes. Both of the single mode and multi-mode fibers are made primarily of fused silica, which is the same material as that of the ferrule and diaphragm. Since no adhesive is used to bond the sensor parts, the sensor is expected to be reliable and can endure high temperature near the operational limit of the optical fiber itself. Also, this all-silica configuration will be resistant to corrosion. The multi-mode fiber has a higher CTE than both the SMF and the ferrule because of the higher doping level inside the fiber. When temperature increases, the multi-mode fiber expansion can compensate for the ferrule axial expansion. The splice between the SMF and the MMF will introduce an optical loss, but typically less than 0.1dB.

A CO₂ laser beam was focused on the interface between the diaphragm and the pit edge of the ferrule. The ferrule was held in a mechanical holder, which was driven by a servo motor (SilverMax 17, QuickSilver Controls, Inc.). The ferrule was rotated along its longitudinal axis while the laser was directed to the top of the ferrule on which the diaphragm was placed. In this manner, it was possible to realize circular laser induced fusion bonding of the diaphragm and the ferrule.

The optical fiber was inserted into the central bore of the ferrule to form a F-P cavity between the fiber end face and the inside surface of the diaphragm and was connected to a white light interferometer system. The cavity length (air-gap) was pre-adjusted by a one dimensional translation stage holding the fiber tail, and monitored on-line by the white light system. The laser beam was defocused and directed to the side of the rotating ferrule and fiber. The ferrule and fiber rotated clockwise and then counterclockwise alternatively, to avoid twisting the fiber tail. A portion of the air is driven out during the high temperature fusion bonding, such that after cooling, the sensor cavity experienced a partial vacuum. This reduced the temperature dependence significantly since the gases inside the cavity will expand as the temperature is increased, which in turn would cause the diaphragm to deflect outward. But the small amount of residual air that remained after bonding still caused a slight internal pressure increase when temperature was increased to 700°C, which introduced some measurement error. The bonding temperature was approximately equal to the softening point of the fused silica (~1600°C) [66], the heated air nearby expanded to create a partial vacuum in the cavity, which would decrease the temperature dependence of the sensor. In addition, once the diaphragm thickness and the ferrule pit are determined, the sensor's pressure response is highly repeatable. The fabrication process is relatively simple and only requires less than half an hour to complete.

We need to control the air-gap of the fiber sensor because of the following reasons:

- (1) The visibility is highly related with the air-gap length.
- (2) The initial operating point should be optimized to efficiently use the dynamic measurement range of the sensor system. For example, efficiently operated within a linear range of one fringe
- (3) Measurement precision will be affected by the initial air-gap value.

An alternative way to bond the fiber inside the ferrule is to use a high temperature flame to heat the ferrule and fiber to realize a hermetic seal, as shown in the diagram in Fig. 4.13 and the photo of the bonding in Fig. 4.14.



Fig. 4.11 The diaphragm to ferrule end bond (top view under microscope)

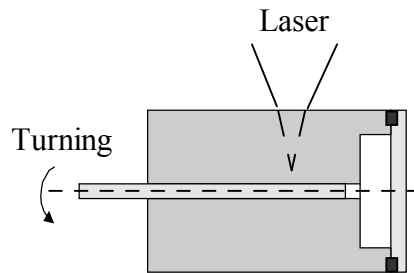


Fig. 4.12 Fiber and ferrule thermal bonding.

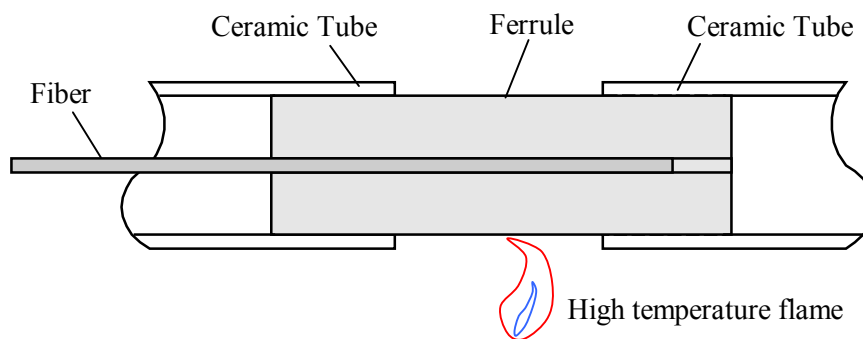


Fig. 4.13 Thermal bonding between an optical fiber and a ferrule.

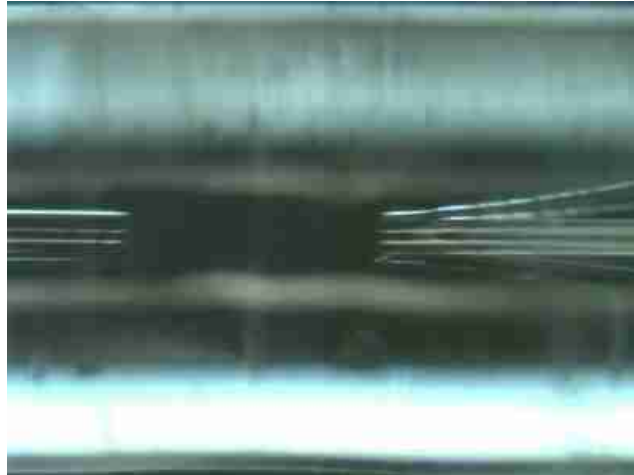


Fig. 4.14 Photo of the fused bonding between an optical fiber and a ferrule.

The sensor head is 8mm long and 1.8mm in diameter as shown in Fig. 4.15.

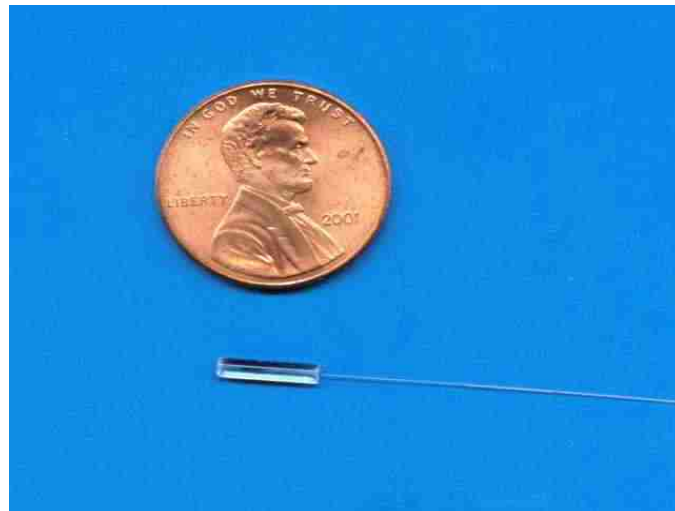


Fig. 4.15 Photo of the engine sensor

4.5.4 Vacuum sealing techniques

Vacuum-sealed techniques are widely used in pressure sensor assembling [67, 68]. As discussed in Chapter 4, the residual air pressure in the sensor cavity was estimated to be 3-6 psi at room temperature. For a sensor with sensitivity of 2.5nm/psi and a temperature change of 600°C, the thermal induced error is about 15-30nm. The case will become worse when a thinner diaphragm is used that is more sensitive to pressure changes. Therefore, the residual air problem is the main technical obstacle in making a high sensitivity pressure sensor with high accuracy.

A promising solution is to seal the sensor cavity in a vacuum chamber using the laser based vacuum sealing technique (LBVS). The schematic of the sensor fabrication is shown in Fig. 4.16. The laser window is a double side polished disc made of ZnSe, which is transparent to the CO₂ laser beam ($\lambda = 10.6 \mu\text{m}$). In practice, only one bonding process requires a vacuum. For example, the fiber to ferrule bonding can be done in air while the wafer to ferrule bonding is finished in vacuum.

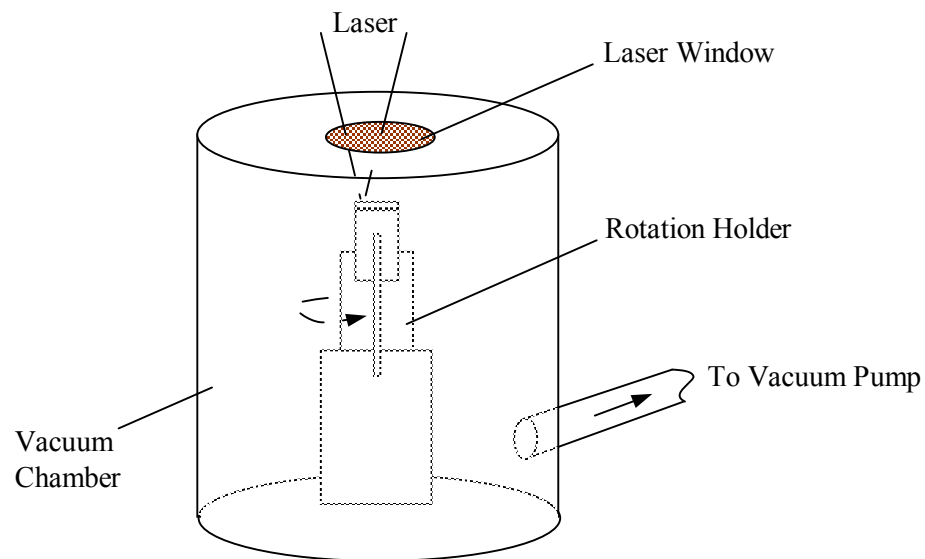


Fig. 4.16 Vacuum-sealed laser bonding sensor fabrication

Based on the experiment results shown in Fig. 4.17, the vacuum-sealed pressure sensor will reduce the temperature dependence by about 65%. For sensor with a thinner diaphragm, this will lead to a smaller temperature induced error in pressure measurement.

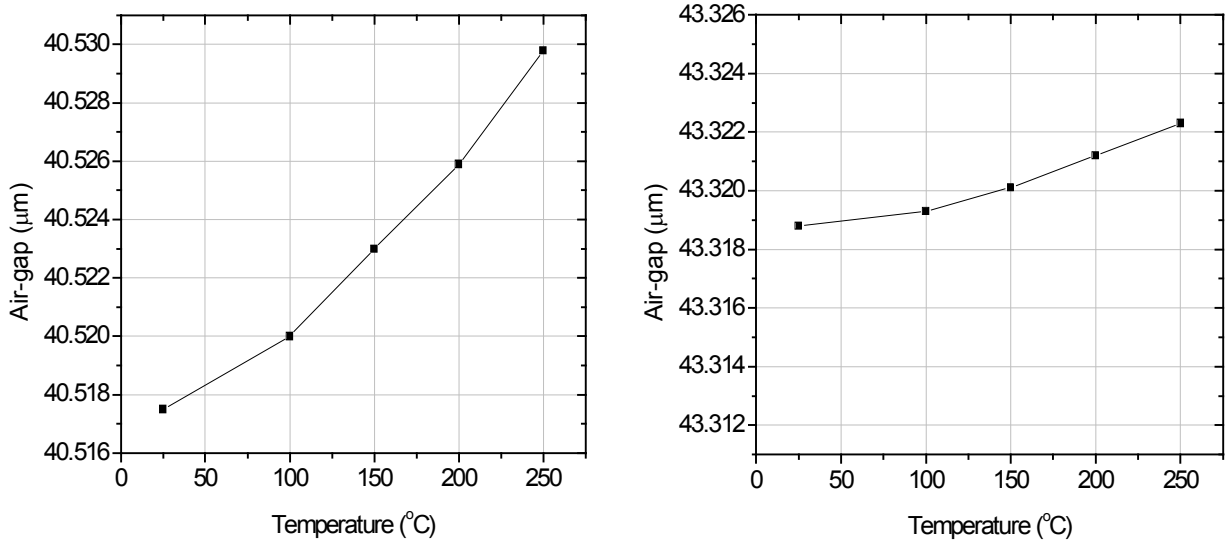


Fig. 4.17 Temperature dependences of the sensor fabricated in air and vacuum

4.6 Sensor packaging

The fiber optic sensor packaging plays an important role in real applications, especially for those in harsh environments. The packaging scheme will definitely influence the performance of sensors. Good packages will improve the sensor mechanical strength, make it easy to handle and install on testing ports; otherwise, the sensor will not work well or even cannot survive in the operating environment.

The sensor head and part of the optical fiber tail is packaged in a metal housing as shown in Fig. 4.18. A metal ferrule (140) with a 7mm long taper is knocked heavily into the stainless steel fitting (100) to make a tight fit. A piece of stainless steel tubing (130) is inserted into the fitting (100) from the other end and bonded with ceramic adhesive. The fiber sensor is composed of a glass ferrule (110) and an optical fiber

(120). The glass ferrule (110) is inserted into the metal ferrule (140) and bonded therein with ceramic adhesive and the fiber tail is bonded with the steel tubing by ceramic adhesive. This sensor packaging exhibited no failure during 2.5 hours of engine operation. The photo of the packaged sensor is shown in Fig. 4.19. The pressure sensor packaging is comparable to commercially available Kulite sensors, which allows the sensor to be easily installed in standard ports in engines.

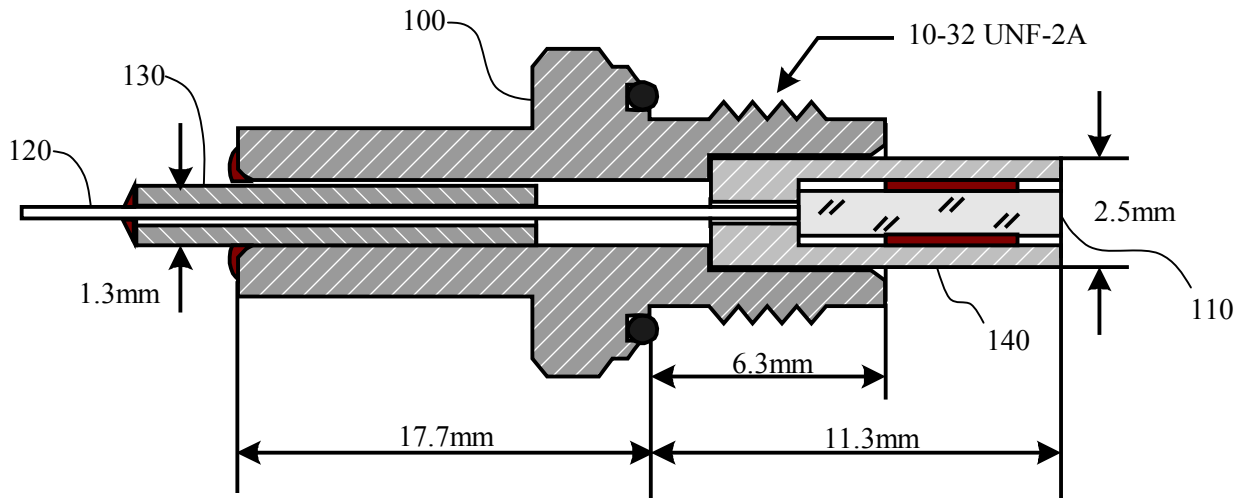


Fig. 4.18 Fiber optic pressure sensor packaging

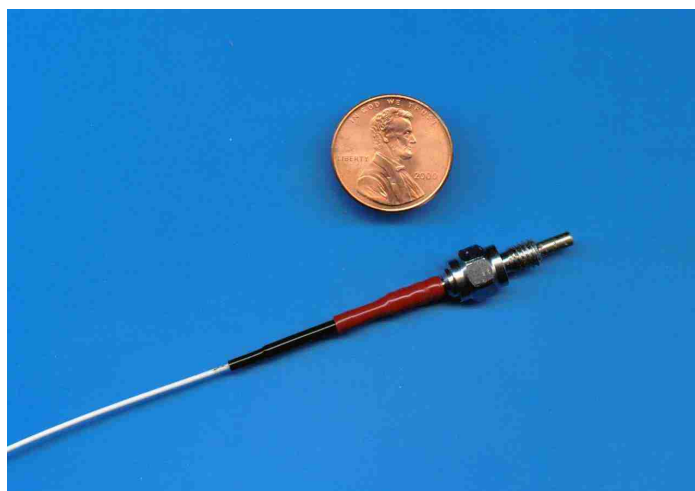


Fig. 4.19 Photo of the packaged fiber optic pressure sensor

Chapter 5 Sensor Signal Interrogation Systems

This chapter will describe the sensor signal interrogation systems, including the white-light interferometry system, Component Test system (CTS) and SCIIB system. The signal processing schemes will also be presented.

5.1 White light interferometry system

The basic structure of the spectrometer-based white light system is shown in Fig. 5.1.

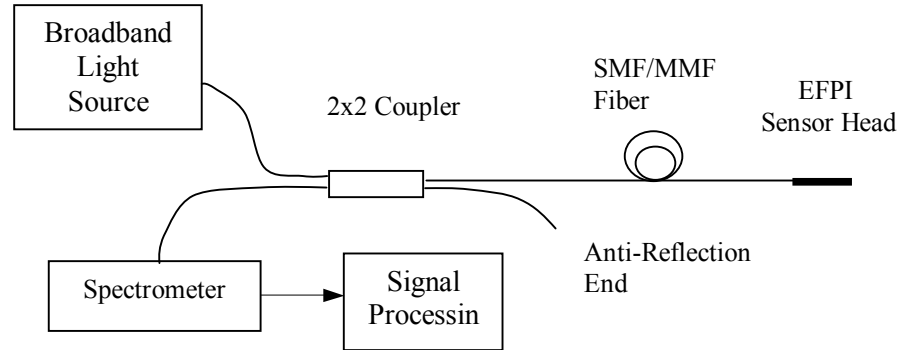


Fig. 5.1 The basic structure of the interferometer-based white light system.

The broadband light source used is an 850 nm LED with a 60 nm bandwidth. Through a 2×2 optical fiber coupler, the optical power output from the light source is launched into the connecting fiber and propagates to the EFPI sensor head. The light signal reflected from the sensor head travels back along the same fiber and is directed to the spectrometer (USB 2000, Ocean Optics) from the other port of the 2×2 coupler. Then, the measured spectrum is transferred to the PC for data processing.

To obtain an interference spectrum with high fringe visibility, the air-gap must be within half the coherence length of the light source used in the system. In this system, the coherence length is mainly dependent on the spectral resolution of the spectrometer, the Numerical Aperture (NA) of the optical fiber and the quality of the

EFPI sensor head. The interference spectrum measured by the spectrometer is given by:

$$I(\lambda) = 2I_s(\lambda) \cdot \left(1 + \gamma \cos\left(\frac{4\pi G}{\lambda} + \varphi_0\right) \right), \quad (5-1)$$

where $I_s(\lambda)$ is the spectral power distribution of the light source with wavelength λ , γ is the visibility of the interference spectrum, φ_0 is the arbitrary initial phase difference, and G is the air-gap, which is determined by the physical parameters (such as pressure or temperature) to be measured. Normalizing Eq. (5-1) with respect to the Gaussian spectrum of the light source, the normalized interference output can be expressed as

$$I_n(\lambda) = 2 \left(1 + \gamma \cos\left(\frac{4\pi G}{\lambda} + \varphi_0\right) \right). \quad (5-2)$$

The value of the air-gap G can be calculated from Eq. (5-2) and then be used to demodulate the physical parameter of interest. The configuration of the white-light system is shown in Fig. 5.2.

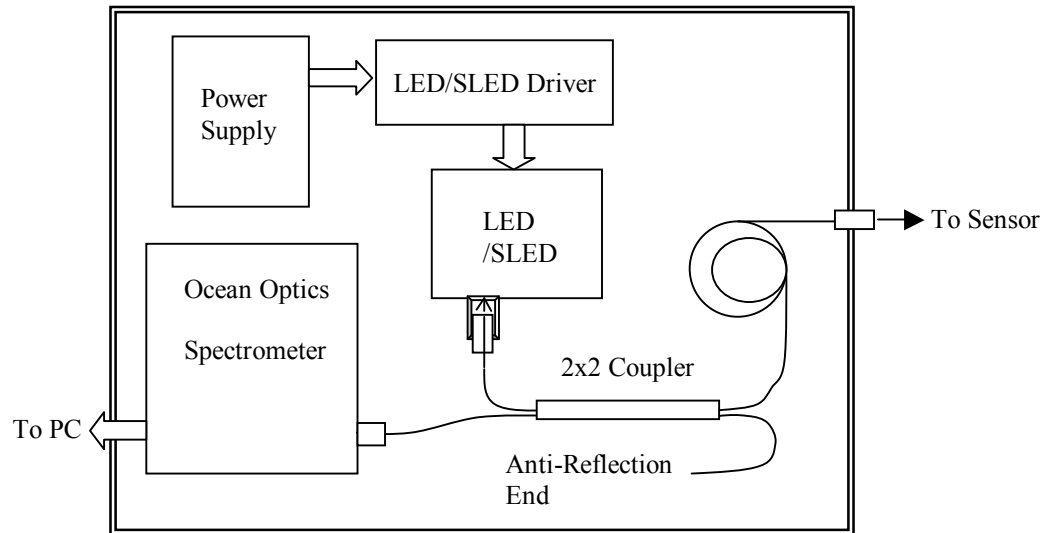


Fig. 5.2 Schematic of the white light system box

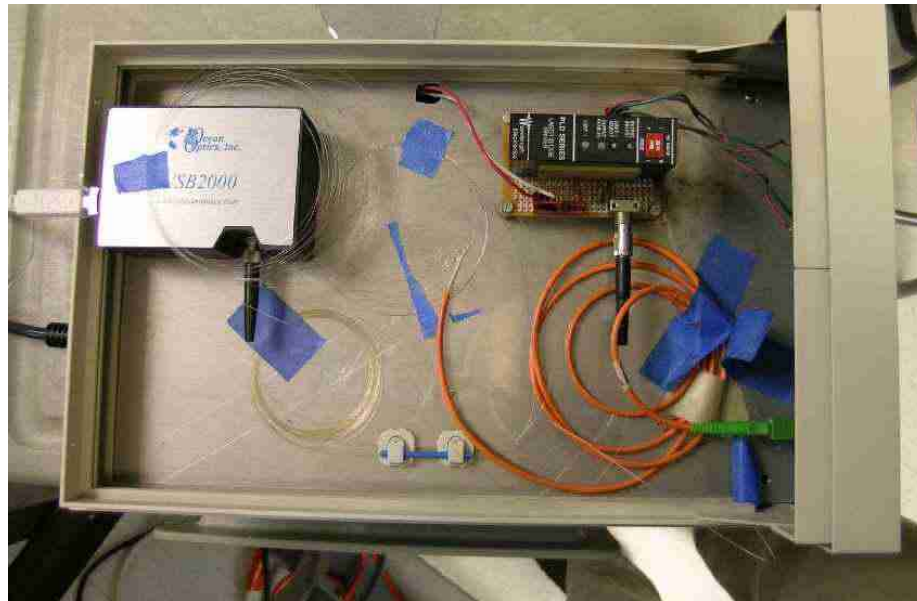


Fig. 5.3 LED and spectrometer based fiber optic white light system

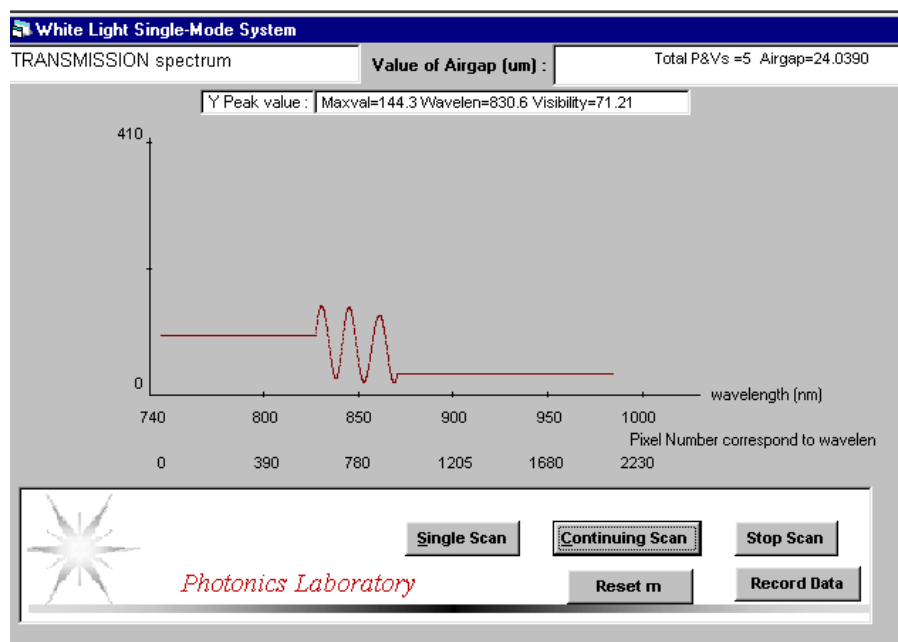


Fig. 5.4 Fringes from a sensor connected to the single mode white light

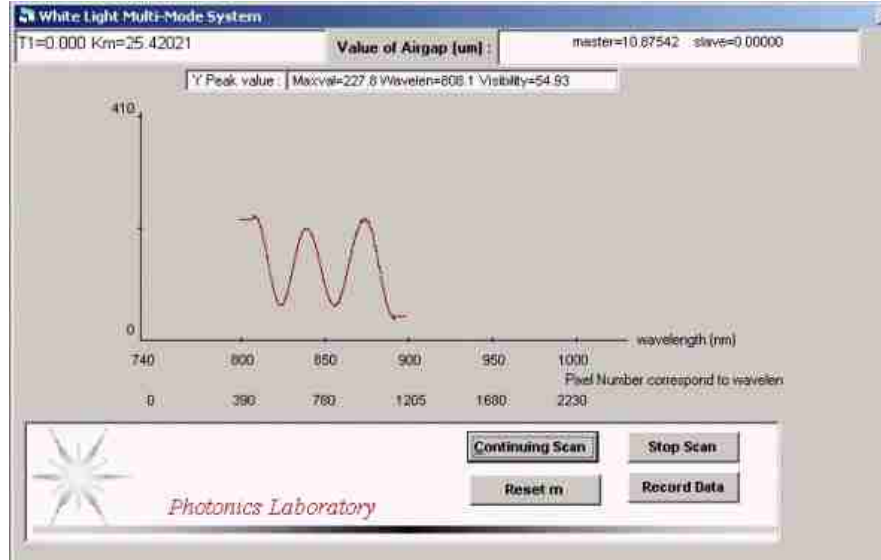


Fig. 5.5 Fringes from a sensor connected to the multi-mode white light

5.1.1 Signal demodulation

The air-gap can be measured with high resolution by fringe analysis [47]. The dynamic range of the measurement is large, which is from several microns to millimeters. The following paragraphs will discuss the method in detail.

5.1.1.1 One-valley tracing method

This technique [4, 47] is based on tracing a special point in the interference spectrum (such as a peak point or valley point). Then from the wavelength of this point, the value of the air gap can be demodulated. The wavelength λ_m of a peak point in the interference spectrum satisfies:

$$\frac{4\pi L}{\lambda_m} + \varphi_0 = m2\pi, \quad (5-3)$$

where the spectral order m is a nonnegative integer. Eq. (5-3) can be transformed into:

$$L = \frac{(m2\pi - \varphi_0)\lambda_m}{4\pi} = \frac{K_m}{2} \lambda_m \quad (5-4)$$

$$K_m = \frac{(2m\pi - \varphi_0)}{2\pi} = m - \frac{\varphi_0}{2\pi} \quad (5-5)$$

Obviously, for a given spectral order, the value of K_m is a constant. To solve the ambiguity problem and demodulate the air gap L from a special peak wavelength λ_m , K_m must be acquired first. Special techniques are needed to identify the interference order m . The resolution of the measurement is mainly dependent on the stability of spectrometer and the arithmetic used for finding the peak position. From Eq.(5-4) and (5-5), the relative error of this system can be described as

$$\left| \frac{\Delta L}{L} \right| \cong \left| \frac{\Delta \lambda}{\lambda} \right| \quad (5-6)$$

Here, $\Delta \lambda$ is the error of peak position. Normally, the spectral resolution, a parameter used to describe the ability of a spectrometer in separating two closely spaced peaks in a spectrum, is very important in spectroscopic applications. In our case, to resolve the peak position accurately, the critical factors are stability, the number of pixels of the CCD detector, and the signal to noise ratio. To improve the signal-to-noise ratio, a smoothing digital filter is used as the first step of the data processing. Then the rough peak position is found by searching the local maximum in the spectrum. In the final step, all the pixels within a suitable range from the rough peak will be used to calculate the accurate peak position. Using this method, the peak position can be determined very accurately even with a low-cost spectrometer.

5.1.1.2 Air-gap absolute measurement

Using two or more special points in the interference spectrum, it is easy to acquire the absolute value of air gap L . Suppose λ_1 and λ_2 are the wavelengths of two adjacent peak points in the interference spectrum, and their interference orders are m and $m+1$. From Eq. (5-3), we got:

$$\frac{4\pi L}{\lambda_2} + \varphi_0 = m2\pi, \text{ and } \frac{4\pi L}{\lambda_1} + \varphi_0 = (m+1)2\pi, \quad (5-7)$$

The air gap L can be demodulated from:

$$L = \frac{\lambda_1 \lambda_2}{2(\lambda_2 - \lambda_1)} \quad (5-8)$$

Obviously, this method overcomes the ambiguity problem. Yet, compared with the technique described in Sec. 5.1, the resolution of this method is much lower. From Eq. (5-8), the relative error is

$$\left| \frac{\Delta L}{L} \right| \cong \sqrt{2} \left| \frac{\lambda_2}{\lambda_2 - \lambda_1} \right| \left| \frac{\Delta \lambda_1}{\lambda_1} \right| \quad (5-9)$$

Comparing Eq. (5-9) and (5-6), the relative error was enlarged by a factor of $\sqrt{2}\lambda_2 / |\lambda_2 - \lambda_1|$. In our system, the central wavelength of the light source (LED) is 850 nm. In the normal operating range (corresponding to an air gap between 5 to 15 μm), this factor is about 15 to 50.

5.1.1.3 High resolution absolute measurement

To achieve both high resolution and absolute measurement, the approach of using wavelengths of two adjacent peak points in the interference spectrum to get a rough air-gap value from Eq. (5-8) (ambiguity problem is solved) was adopted. This rough air-gap value will be used to determine the interference order number m and a rough K'_m value for one of the two peak points [Eq. (5-4) and (5-5)]. Then, by using a calibrated K stored in the computer, an accurate K_m can be recovered from the rough K'_m . Using Eq. (5-4) and (5-5) again, the accurate air-gap value can be calculated from the accurate K_m and the peak wavelength (therefore, high resolution is achieved).

The technique used here to recover the accurate K_m from the rough K'_m value is presented as follows. In Eq. (5-4) and (5-5), although K_m is not an integer, for a given peak, it is a constant and for adjacent peaks, the difference in K_m is 1.

By calibration, the K_m value for a special peak (K_m^0) can be acquired and stored in the computer. During the process of measurement, when the rough K'_m value for one peak has been acquired, although we do not know the order m of this peak point, the difference between K_m and the stored K_m^0 should be an integral number. So, the

accurate K_m can be calculated by adding K_m^0 with the integer part in the difference between the rough K'_m and K_m^0 .

$$K_m = K_m^0 + \text{INT}(K'_m - K_m^0 + 0.5), \quad (5-10)$$

where function $\text{INT}(\)$ means to obtain the integral part. Another approach for recovering the accurate K_m value from the rough K'_m value is to calibrate K_m for all the peak points that will be used in the whole dynamic range and store them in the computer. During the process of measurement, when a rough K'_m value is acquired, the closest K_m stored in the computer will be chosen as the accurate K_m . Both approaches have been realized in Visual Basic, with the second one producing a more robust performance. There are other novel techniques that can solve the ambiguity problem without losing the high resolution [69-71]. In [72], Fourier transform spectroscopy (FTS) was used to demodulate the white light signal. The scanning of a reference path, which eliminates the ambiguity problem, was performed inside the FTS. Similar to other scanning based techniques, the dynamic range can be larger than the coherence length, as long as the path difference between the sample and reference paths is in the right range. However, this is achieved by sacrificing the robustness and simplicity of the system. In [71], a data processing method was used to solve the ambiguity problem.

To achieve high resolution, all the peaks in the interference spectrum were used to determine the length difference between the two beams of the interferometer. The error was minimized by using a least-square fitting approach. Obviously, the performance of this method is dependent on how many peaks can be acquired in the bandwidth of light source. In our case, in the operating range of the multimode sensor head, only two to five peaks can be resolved from the original interference spectrum. Therefore, this method is not suitable for our system.

5.2 CTS based sensor signal interrogation system.

As shown in Fig. 5.6, the tunable laser of a Component Test System (CTS, Micron Optics) was coupled into the sensor through a 2x2 coupler and the reflected light was routed back through the same coupler to the receiver of the CTS. A real time scan of the tunable laser produced the spectrum information from 1520 nm to 1570 nm with a 2.5 pm resolution, which can be considered as a swept white-light system. The phase trace method [47] was used to process the optical signal in order to demodulate the air-gap thickness. The CTS system exhibits an air-gap measurement resolution of $L \times 10^{-6}$, where L is the air-gap. For example, if the sensor air-gap is $30 \mu\text{m}$ then the system resolution is about 0.03nm.

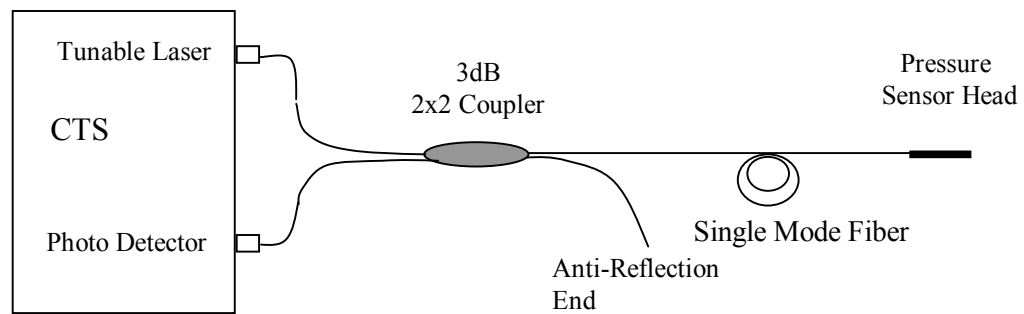


Fig. 5.6 Schematic of the CTS based sensor interrogation system



Fig. 5.7 Photo of the sensor interrogation system

5.2.1 Sensor signal from CTS

Compared with the white-light system, the CTS light source is a narrow band tunable laser. Since the laser tuning range is from 1520 to 1570nm, the signal demodulation schemes of white-light system are still applicable to sensors with air-gaps large enough that at least two valleys or peaks are shown within the bandwidth (Fig. 5.8). In fact, by pre-measuring the sensor air-gap with the 850nm white-light system, the CTS system can handle sensors with small air-gaps down to 15 μm , beyond which only relative measurement (Fig. 5.9) and calibration can be obtained. Since the number of sampling points on the CTS is fixed at 20,000, the fewer the number of valleys in the bandwidth, the higher resolution of the single valley trace method. Therefore, for most applications, the air-gap should be set to allow two or three valleys in the bandwidth window.

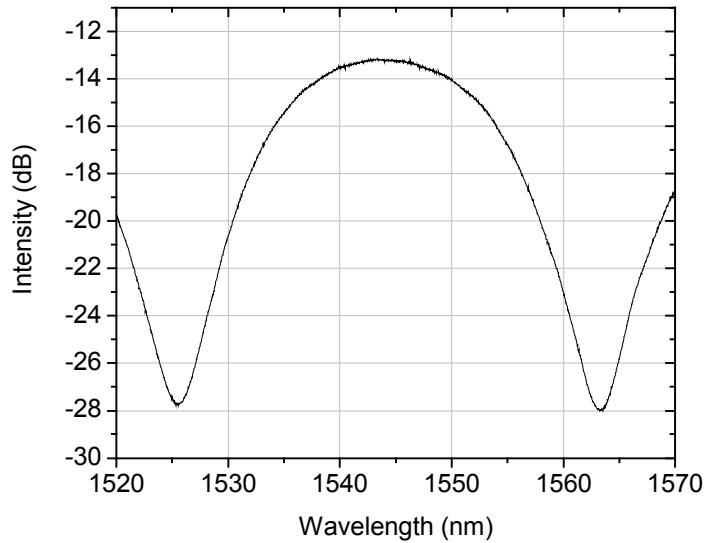


Fig. 5.8 Sensor signals from CTS (air-gap $\approx 31\mu\text{m}$)

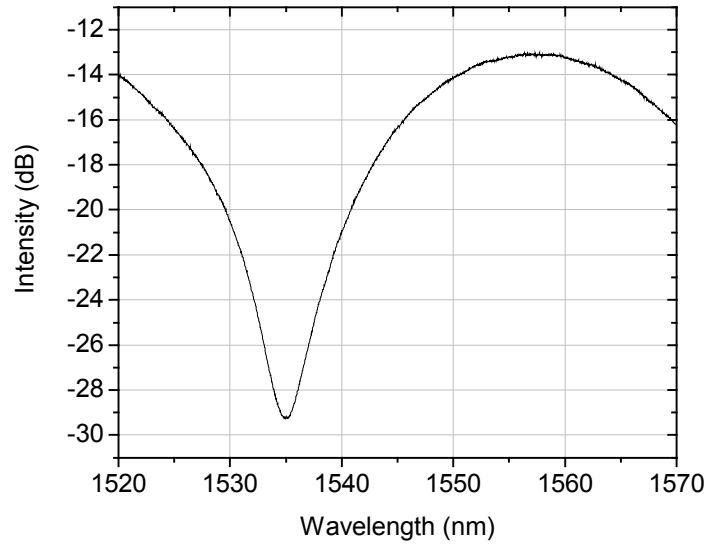


Fig. 5.9 Sensor signals from CTS (air-gap $\approx 25\mu\text{m}$)

5.3 SCIIB sensor interrogation system

When the pressure sensor is used to detect dynamic pressure or acoustic waves, the signal processing system must have enough bandwidth to faithfully demodulate the high frequency components. The typical dynamic pressures in a turbine engine are at frequencies of $\sim 10\text{kHz}$. However, the white-light system can detect dynamic signals up to 75Hz and the CTS can scan the whole spectrum with a maximum rate of only 5Hz , both of which are not capable of measuring the high frequency signals. To meet the measurement requirements, a self-calibrated interferometric-intensity-based (SCIIB) [8, 73] system was used to demodulate the high frequency sensor signals. A schematic of the SCIIB signal interrogation system is shown in Fig. 5.10.

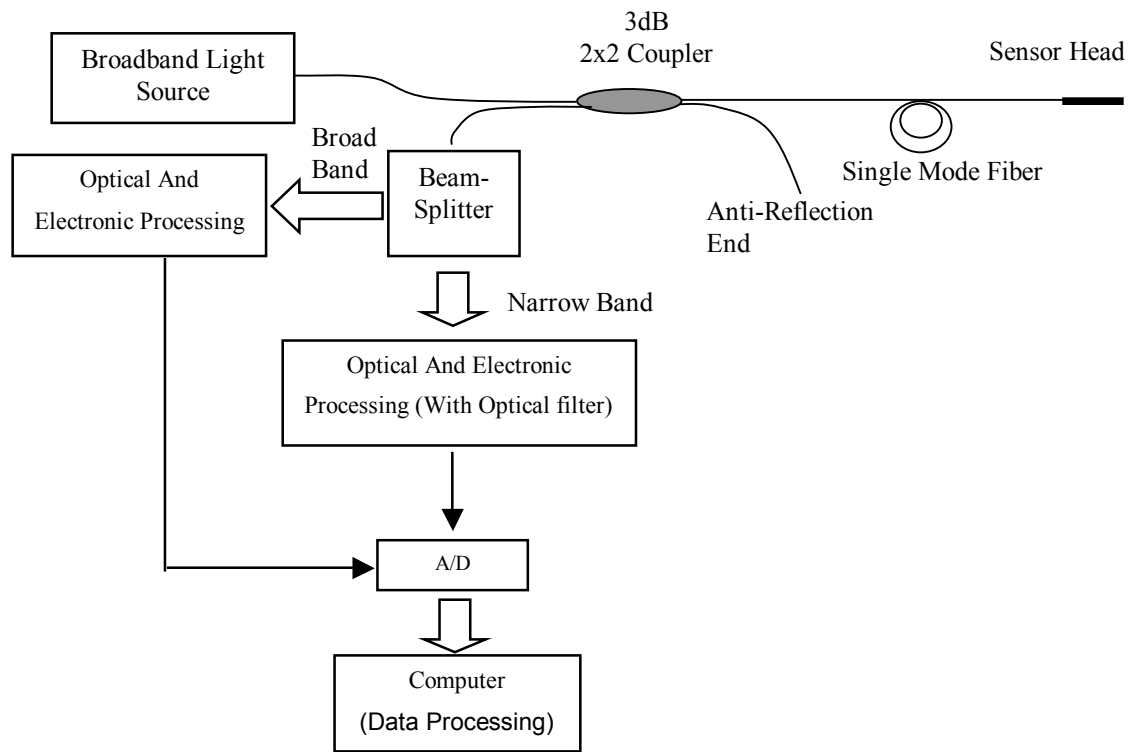


Fig. 5.10 Schematic of SCIIB fiber optic sensor interrogation system

5.3.1 Single mode fiber based SCIIB System

The schematic of the single-mode SCIIB sensor system is shown in Fig. 5.11, and the and a photograph of the system is shown in Fig. 5.12. The single-mode SCIIB system is designed to operate at a central wavelength of 1310 nm and to use single-mode fiber to transmit optical signals between the sensor probe and the signal-processing unit.

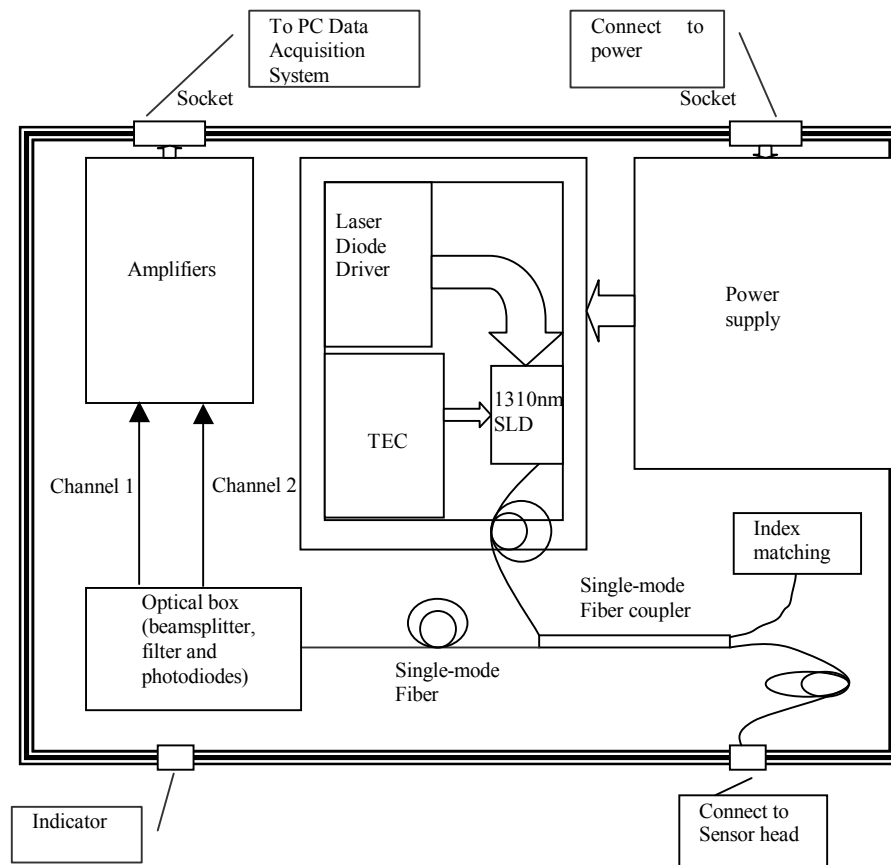


Fig. 5.11 Schematic of the single-mode SCIIB sensor system box

Single-mode fibers have very low optical attenuation to the transmitted light. The typical attenuation of single-mode fiber is about 0.3dB/km at a wavelength of 1300nm and 0.2dB/km at 1550nm. Therefore, light can be transmitted inside the single-mode fiber for a very long distance. However, due to the small core diameter of single-mode fibers, it is relatively difficult to couple the light efficiently from optical sources into the fiber. Also, low-noise detection of the light at 1300nm or 1550nm requires expensive InGaAs photodetectors. Therefore, the cost of single-mode fiber-based sensor systems is much higher compared to those made by multimode fibers. The single-mode fiber-based SCIIB sensor system is mainly designed for long distance applications, typically longer than one kilometer from the actual sensing region to the signal processing unit.



Fig. 5.12 Photograph of the developed single-mode SCIIB sensor system

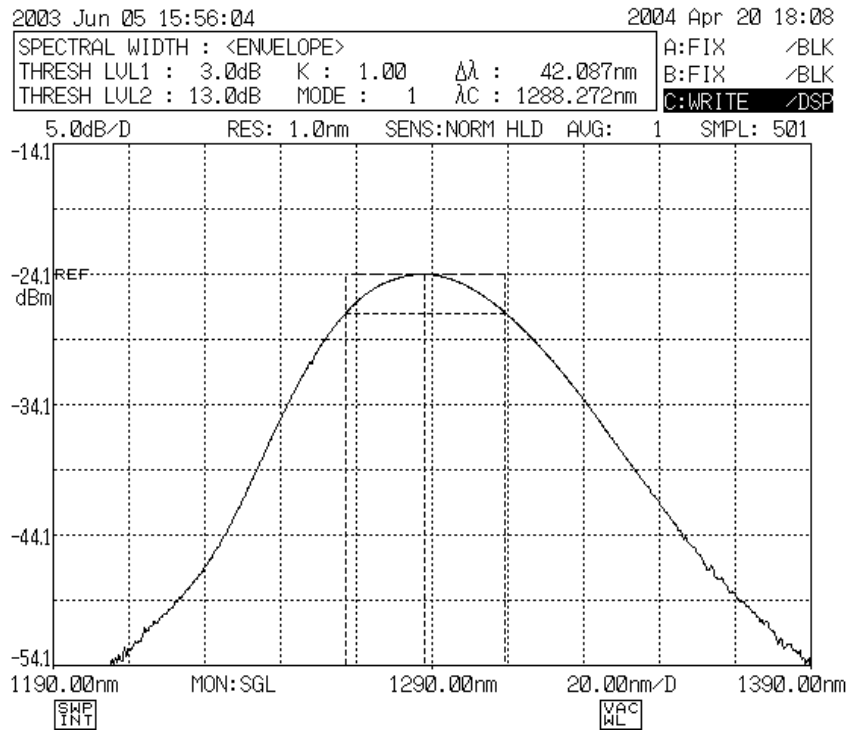


Fig. 5.13 The spectrum profile of the LED light source

The narrowband and broadband SCIIB signals have different coherent lengths according to Eq. (3-14). The following are simulation results of the narrowband output, the broadband output and the ratio of the narrowband to the broadband:

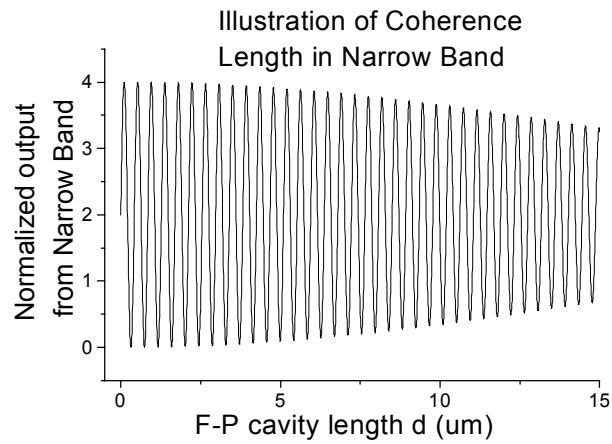


Fig. 5.14 Narrowband output as a function of F-P cavity length d

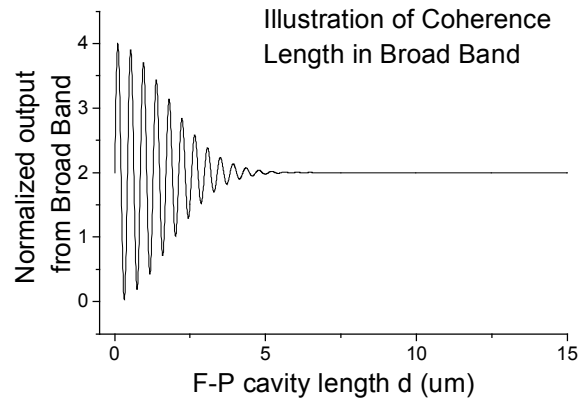


Fig. 5.15 Broadband output as a function of F-P cavity length

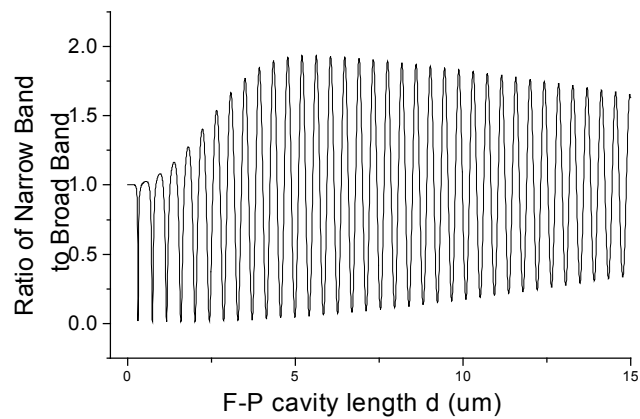


Fig. 5.16 Ratio of narrowband to broadband as a function of F-P cavity length d

From the view of the operation of the sensor system, the two channels' outputs are from the same optical source and experience the same transmission path. Thus they have almost the same behavior in terms of optical source's power fluctuation and fiber loss variations. The ratio of the two outputs is only a function of the Fabry-Perot cavity length; there is no influence from the light source, and thus it eliminates these two sources of errors from the final result of the measurement.

From Fig. 5.15, the visibility of broad band signals diminish and its intensity become flat when sensor air-gap is larger than $6\mu\text{m}$. In practice, we make sensors with air-gaps between $10\text{-}30\mu\text{m}$ to enable the intensity calibration while keeping good signal visibilities.

Chapter 6 Sensor Calibration and Sensor System Performance

This chapter will discuss the sensor calibration and sensor system performance. The sensor lab experiment and field test results will be presented.

6.1 Sensors' temperature dependence

To obtain good pressure measurement results, the pressure sensor should have low temperature dependence; otherwise, the thermal induced error will cause the measured pressure to be misinterpreted. However, all types of pressure sensors exhibit some temperature dependence, which has been a problem in pressure sensing technology for a long time. A variety of temperature compensation methods [32, 74] have been developed in the past two decades, which partly solved the problem, but they are not ideal because the temperature compensation makes the sensor system more complicated or more expensive.

The sensor described in this work is made of all-silica material, which has a much smaller CTE than other types of glass. The fused silica ferrule has a CTE of approximately $\alpha_h = 5.5 \times 10^{-7} / ^\circ\text{C}$. The single mode optical fiber used was a communication grade fiber (Corning SMF-28), with a CTE of $\alpha_s = 5.6 \times 10^{-7} / ^\circ\text{C}$, which is very close to that of the ferrule. The multi-mode fiber was Corning 50/125 μm fiber with a CTE of about $\alpha_m = 7.7 \times 10^{-7} / ^\circ\text{C}$. In general, the more germanium doping in the optical fiber, the higher the CTE. The thermal expansion difference of the ferrule and the fiber in the axial direction will lead to F-P cavity changes. Although these numbers are small, the sensor temperature dependence is still appreciable if the operating environment has a large temperature variation. In addition, the gases trapped inside the cavity will expand as the temperature is increased, which in turn would cause the diaphragm to deflect outward. The total temperature dependence of the sensor can be expressed as:

$$\frac{\Delta L}{\Delta T} = (\alpha_h - \alpha_m)L_m + (\alpha_h - \alpha_s)L_s + \alpha_h L + \frac{YP_r}{T_r} \quad (6-1)$$

where L is the air-gap thickness, L_m is the multi-mode fiber length and L_s is the single mode fiber length, Y is the sensor sensitivity (nm/psi), and P_r is the residual air pressure at temperature T_r . By optimizing these parameters, the sensor temperature dependence can be minimized for a specific temperature range over which the CTEs are valid.

The single mode pressure sensor was put in a furnace at atmospheric pressure. Temperature was increased from room temperature up to 700°C. The result is shown in Fig. 6.1. There maybe several factors that lead to the nonlinearity of the curve but the main reason was the CTE variations of the glass at different temperature [75].

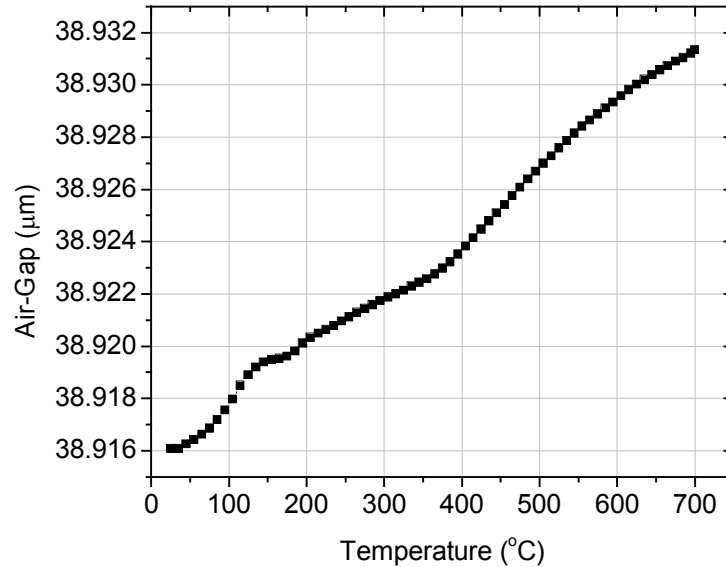


Fig. 6.1 Sensor temperature dependence from 25 °C to 700°C at atmospheric pressure.

The temperature dependence was approximately 0.022 nm/°C. This result is much better than those of sensors made by borosilicate frit bonding (4.06nm/°C) and epoxy bonding methods (50nm/°C). [59]

6.2 Static pressure test

6.2.1 Static pressure testing system

The schematic of the static pressure test system is shown in Fig. 6.2. The sensor head is sealed in a closed end ceramic tube with its fiber tail connected to the sensor interrogation system. The static pressure inside the ceramic tube is controlled by the pressure control system (Model 9035, Pressure Systems), which is connected to a compressed nitrogen gas tank. The pressure can be adjusted accurately from ambient pressure to 200 psig with 0.01% resolution.

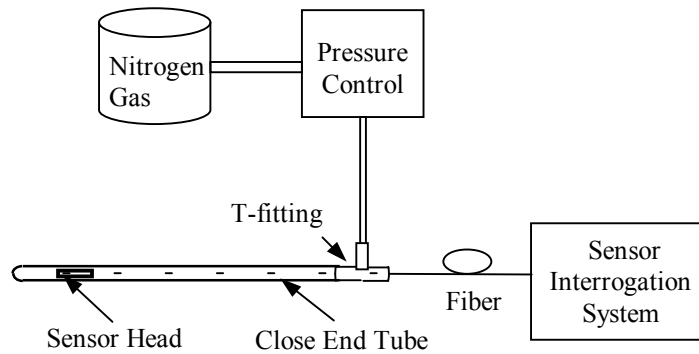


Fig. 6.2 Schematic of the controlled pressure testing system.

6.2.2 Sensor static pressure response

The sensor static pressure response is the essential characteristic to be evaluated before dynamic pressure testing. In particular, this test will verify the leakproofness of the sensor. The sensor pressure sensitivity can be derived from the results, which is the basic reference information for dynamic pressure test and thermal induced error estimation.

The static pressure response of a sensor with a 125 μ m thick diaphragm is shown in Fig. 6.3. The sensor showed a linear response to static pressure 0-200 psi at both room temperature and 700°C with only a slight shift. The sensor pressure sensitivity was

2.93 nm/psi and the sensor system had a resolution of 0.01 psi (68.9 Pa). The sensor pressure sensitivity is consistent with the theoretical prediction. Since the sensor temperature dependence is about 0.022 nm/°C, the thermal induced pressure measurement error is about 0.0075 psi/°C.

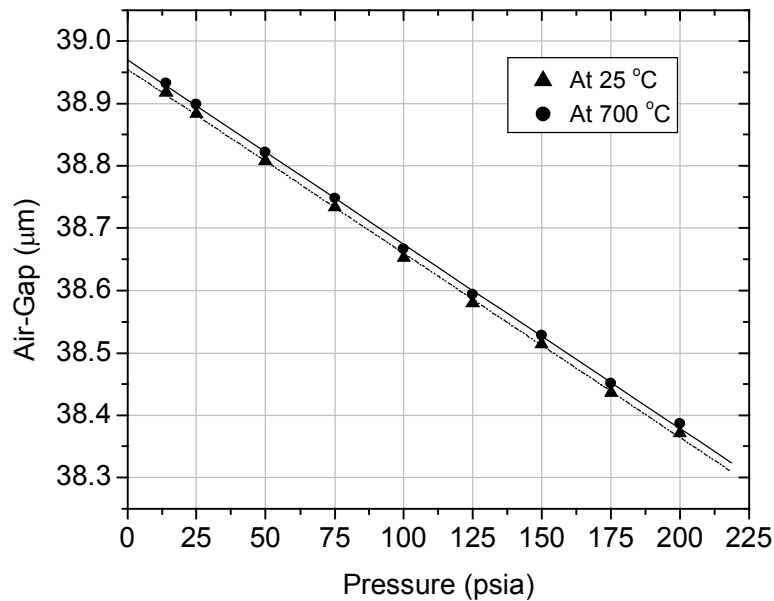


Fig. 6.3 Sensor pressure response at 25 °C and 700 °C.

6.2.3 Sensor response repeatability and diaphragm creep

The sensor response repeatability to pressure of great concern in high precision measurement applications. The diaphragm will deflect under pressure and recover with load released because fused silica glass has a good elasticity. However, it does creep at elevated temperatures even though it has a much higher viscosity compared with other glasses [64]. The viscosity characteristics of the silica glass are important to study its deformation when it is subjected to constant stress at constant temperature. A pressure sensor with 125 μm thick diaphragm was tested at 100 psi at 700°C for ten minutes and the results are shown in Fig. 6.4. The air-gap changed about 40nm during this period due to its deformation. Creep is the response of a refractory material to an applied stress.

Another sensor with a sensitivity of 2 nm/psi was tested for three rounds to evaluate its repeatability at 400°C, 500°C and 600°C as shown in Fig. 6.10-Fig. 6.12. The repeatability became worse when temperature increased.

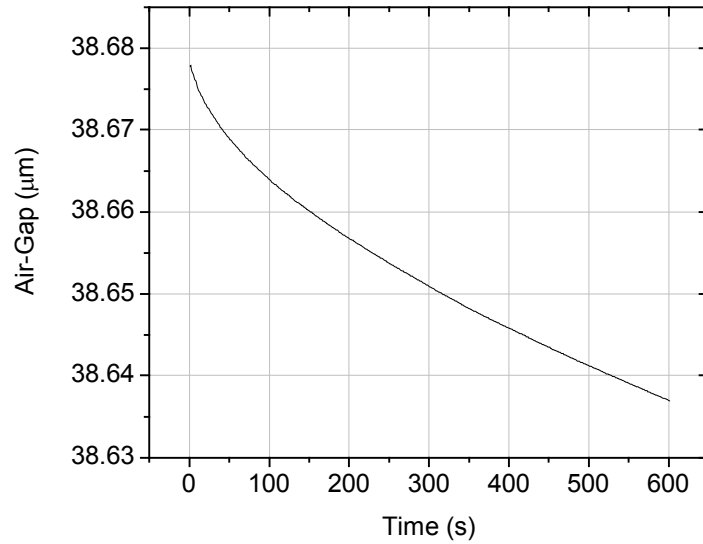


Fig. 6.4 Air-gap change caused by diaphragm creep under constant pressure (100psi) at 700°C

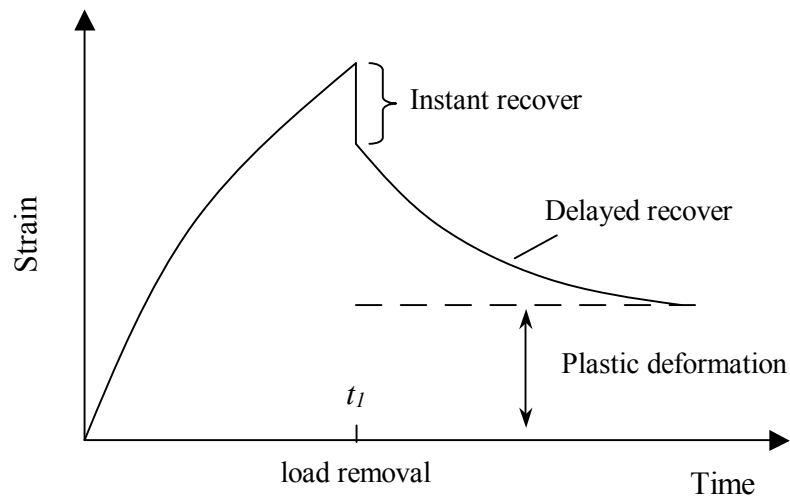


Fig. 6.5 The creep strain of a silicate glass

The creep and recovery phenomenon were observed in the experiment results shown in Fig. 6.6. The flow behavior of silica glass at high temperatures is Newtonian viscous in that the strain rate is related linearly to the applied stress. However, silica glass behaves like a linearly elastic solid at low temperatures, which is not true for metallic and organic glasses. Therefore, silica glass is a good choice in diaphragm material selection especially for applications requiring good repeatability.

Viscosity is a measure of a material's resistance to change in form, which can be regarded as a flow. With Newtonian viscosity, the rate of strain $\dot{\gamma}$ is proportional to the stress τ [76],

$$\dot{\gamma} = \tau / \eta \quad (6-2)$$

where η is the viscosity. For tensile deformation, this maybe expressed as

$$\dot{\varepsilon} = \sigma / 3\eta \quad (6-3)$$

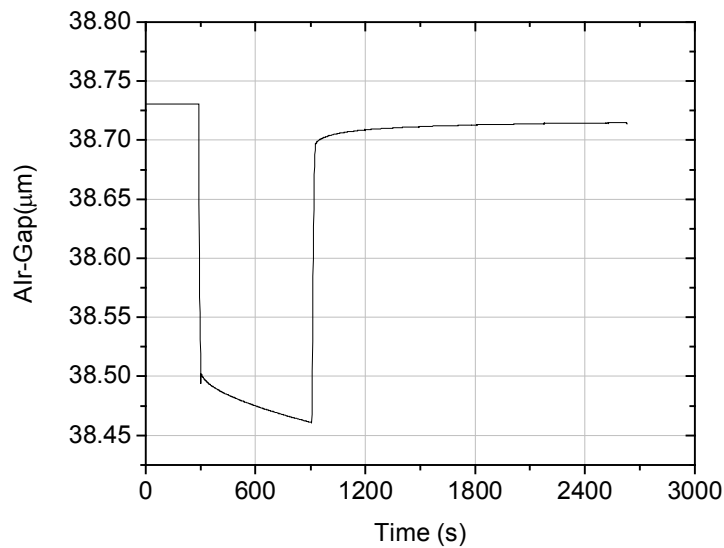


Fig. 6.6 Diaphragm creep and recovery (700 °C)

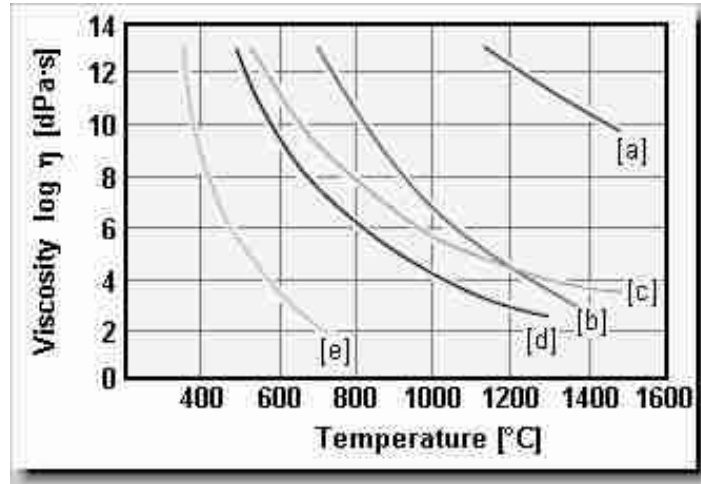


Fig. 6.7 Temperature dependence of the viscosity of some glasses
 (a) fused silica, (b) aluminosilicate, (c) borosilicate,
 (d) soda-lime-silica, (e) lead borate.

Fig. 6.8 shows the cross-section of the diaphragm deflection. To estimate the diaphragm strain in radial directions, the length of BC should be calculated. Since the triangle OAC is similar to triangle COB because of the small deflection. Set:

$$\begin{aligned}
 a &= \text{length of OA}, & \theta &= \angle \text{COB} \\
 y &= \text{length of OC} \\
 x &= \text{length of BC}
 \end{aligned}$$

Since $\theta = \angle \text{AOC}$ and $\tan \theta = \frac{y}{a}$,

then $x = y \sin \theta = \frac{y^2}{\sqrt{y^2 + a^2}}$. Therefore, the radial strain is

$$\epsilon_r = \frac{x}{a} = \frac{y^2}{a\sqrt{y^2 + a^2}} \quad (6-4)$$

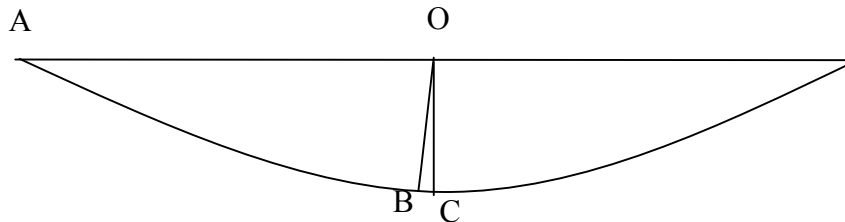


Fig. 6.8 Radial strain estimation from the diaphragm small deflection

The experimental creep rates of the diaphragm at different temperatures are shown in Fig. 6.9. For example, the deflection is about 39 nm during a 600s period at 700°C, thus the corresponding creep rate calculated as:

$$\dot{\varepsilon}_r = \frac{y^2}{ta\sqrt{y^2 + a^2}} = \frac{39^2}{600 \times 700000 \sqrt{39^2 + 700000}} = 5.17 \times 10^{-12} (s^{-1}) \quad (6-5)$$

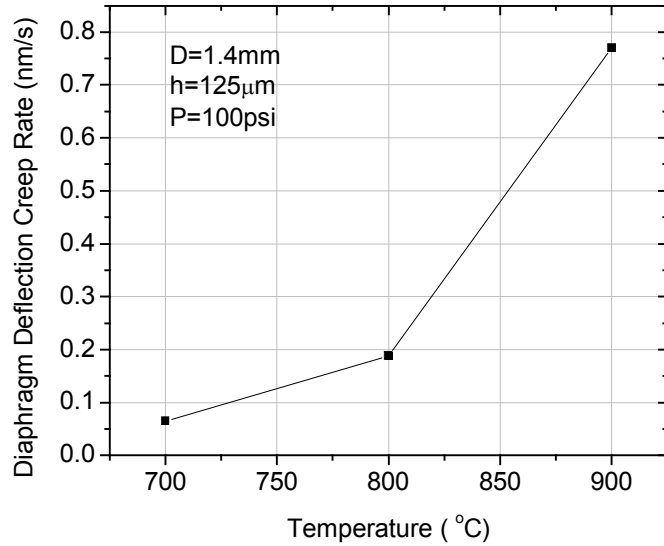


Fig. 6.9 Diaphragm deflection creep rate at high temperature

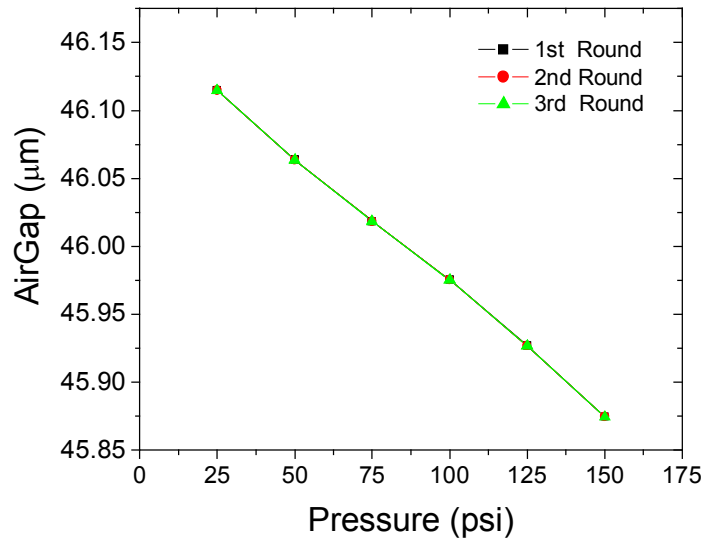


Fig. 6.10 Pressure Response at 400°C

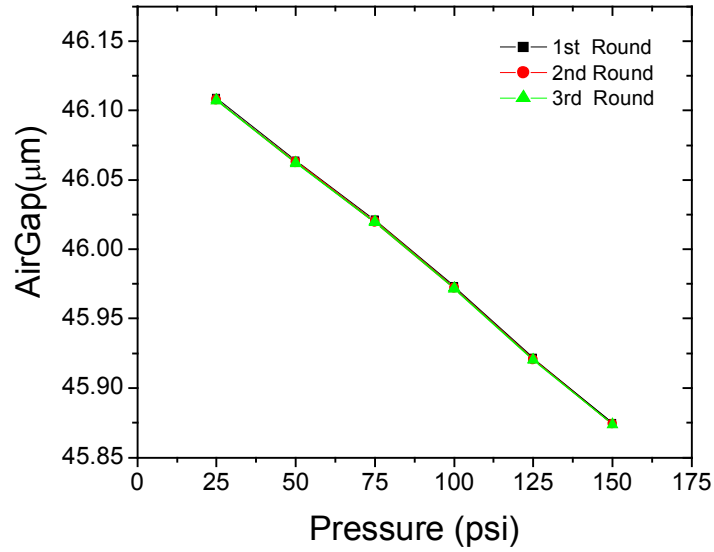


Fig. 6.11 Pressure Response at 500°C

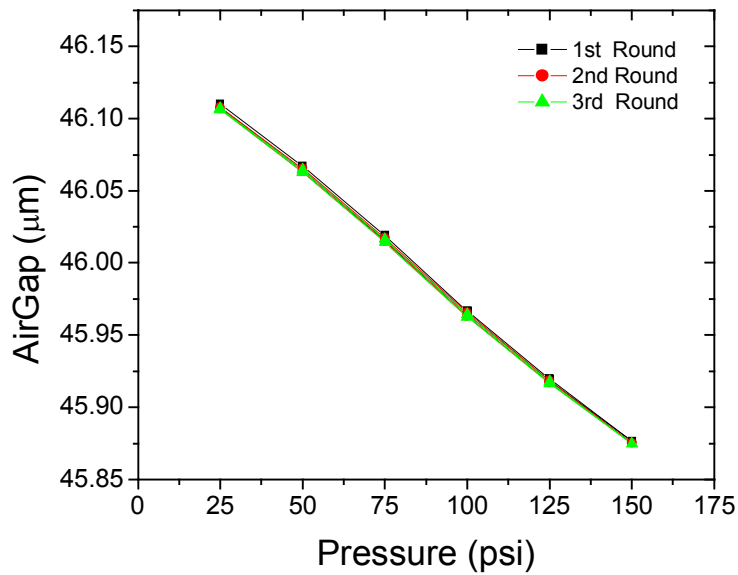


Fig. 6.12 Pressure Response at 600°C

6.3 Sensors' dynamic pressure test

6.3.1 Dynamic pressure measurement

The static pressure response of a pressure sensor with a 60μm thick diaphragm is shown in Fig. 6.13. The sensor pressure sensitivity is about 87mV/psi. Therefore, the

sensor system resolution is about 0.023 psi (159 Pa). To investigate the sensor response to dynamic pressure thoroughly, a dynamic pressure calibration will be needed, such as a shock tube testing. [12]

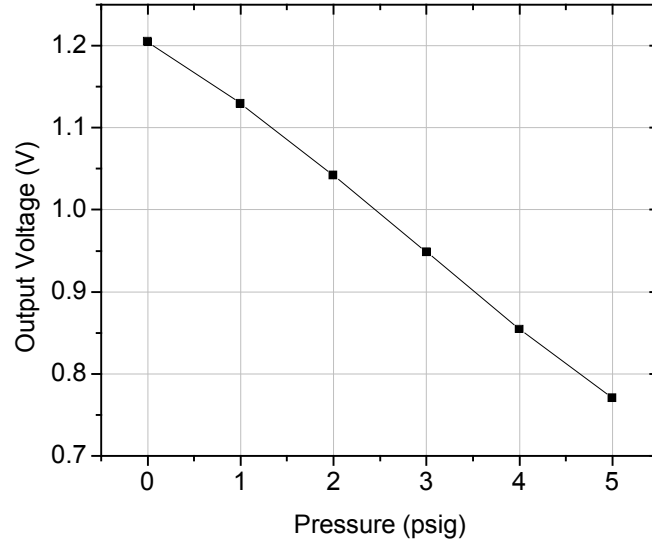


Fig. 6.13 Static pressure response of the diaphragm-ferrule based pressure sensor.

The CTS resolution is $\text{air-gap} \times 10^{-6}$. For example, if the air-gap is 30 μm , the resolution is 0.03 nm. The CTS scan rate is 5 Hz, which is not suitable for high frequency measurement. For this reason, an intensity trace based device such as SCIIB system is needed to demodulate the high frequency sensor signal in real-time.

6.3.2 Sensor frequency response

Some dynamic calibration methods have been reported [12, 77]. The basic principle is to use a pressure impulse to test the diaphragm response. Since a light beam can generate optical pressure, we use a 248 nm excimer laser (MPB MSX250) to generate very short light pulses, which will be radiated on the diaphragm. The laser beam is focused by a UV-graded spherical lens and irradiated on the surface of a diaphragm-based pressure sensor. A pressure pulse with 20 ns duration is generated by the radiation pressure of the light pulse due to the momentum transfer of photons. In experiment, we focused a laser pulse with energy of 20mJ to an area of 5 mm². The corresponding power density of the light pulse is

$$D = \frac{E}{S \cdot T} = \frac{20mJ}{5mm^2 \cdot 20ns} = 0.2 \times 10^{12} (W / m^2) \quad (6-6)$$

Then the radiation pressure is

$$P = \frac{\eta D}{V} = \frac{1 \times 0.2 \times 10^{12}}{3 \times 10^8} \approx 6.7 \times 10^2 (Pa) \quad (6-7)$$

where η is simply set to 1, which means that most of the light power is absorbed by the diaphragm of the sensor. For an optical fiber FP interferometric pressure sensor with a high sensitivity as described below, the radiation pressure in (6-7) is high enough to generate a significant optical path length change of the FP cavity.

The structure of the diaphragm-based pressure sensor and the setup of the experiment are shown in Fig. 6.14.

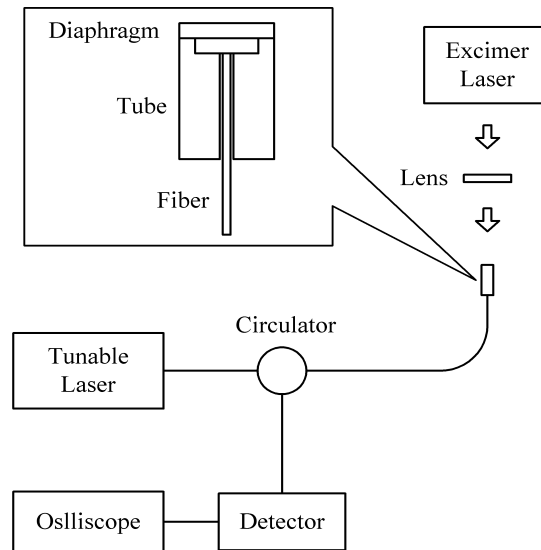


Fig. 6.14 Experimental setup for the sensor frequency response measurement

A continuous wave (CW) tunable laser was used as the light source of the optical fiber pressure sensor system. It was tuned to the quadrature of the FP interferometric pressure sensor so that maximum sensitivity could be obtained. Light from the tunable

laser was launched to the pressure sensor through an optical circulator. The reflected light from the sensor was coupled to a photodiode (PD) detector. An oscilloscope was used to monitor the output of the detector and capture the time domain response of the sensor when a radiation pressure pulse was applied to the sensor.

The time domain response of the sensor to a radiation pressure pulse and its Fourier transform are shown in Fig. 6.15. The top waveform is the time domain response of the sensor to the radiation pressure generated by the light pulse of the excimer laser. The bottom curve shows the Fourier transform result of the time domain waveform. The resonant frequency occurs at 400 kHz, where the intensity is about 20dB higher than the static response. The gain in frequency region lower than the resonant frequency is at least 15dB higher than that of the frequency band higher than the resonant frequency. This result is consistent with the theoretical prediction shown in Fig. 3.16. The volume of air trapped behind the diaphragm, which might act as a stiffening spring, results in a slight increase in frequency.

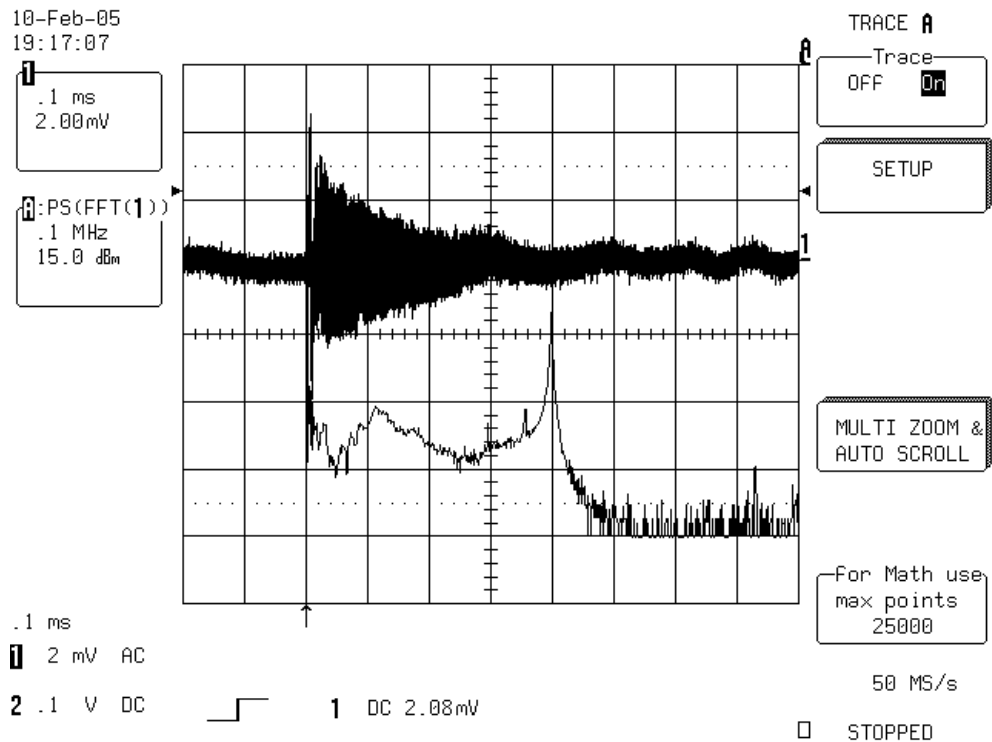


Fig. 6.15 Time domain response and its Fourier transform captured by the oscilloscope

To evaluate the sensor's dynamic performance, an acoustic wave generator was used as dynamic pressure source as shown in Fig. 6.16. A Q-point tuning device [78] was used to track the sensor working point, which must be set within the linear range. The sensor output changed along with the continuous Q-point tuning so linear output ranges and sensor visibility could be obtained. (see Fig. 6.17) The test results at room temperature and 600°C are shown respectively in Fig. 6.18 and Fig. 6.19, where the signals in time domain are on the top and its FFT at the bottom. By properly adjusting the Q point, the sensor dynamic responses at different temperatures are not much different. For the time domain, the sensor response is about 5 mV peak to peak with its FFT having a signal to noise ratio of about 18.8dB.

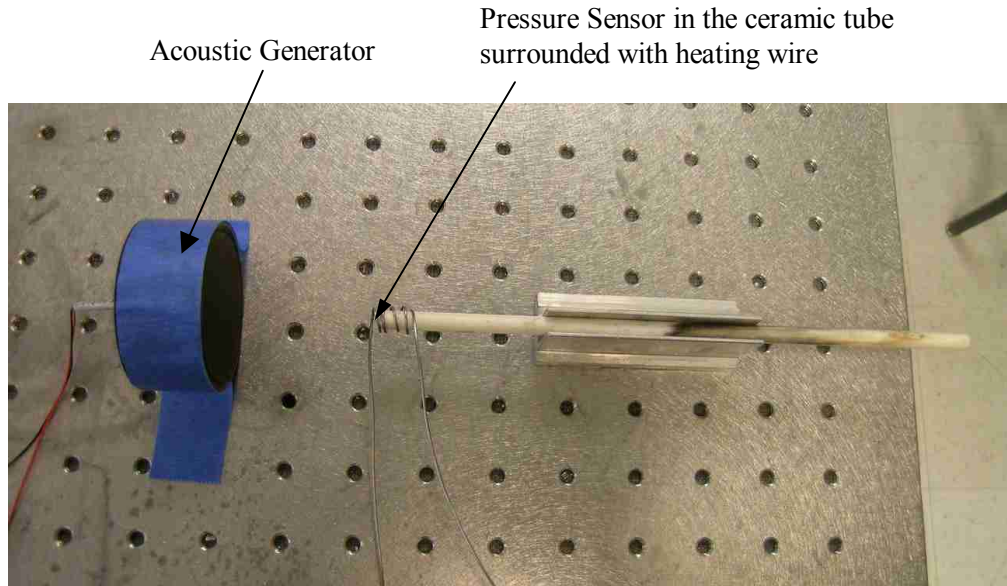


Fig. 6.16 The sensor dynamic pressure test setup

For the Q-point tuning response in Fig. 6.17, the maximum and minimum outputs are 3.4 V and 1 V respectively, so the sensor's visibility is 54.5% by the following equation

$$Visibility = \frac{I_{max} - I_{min}}{I_{max} + I_{min}} \times 100\% \quad (6-8)$$

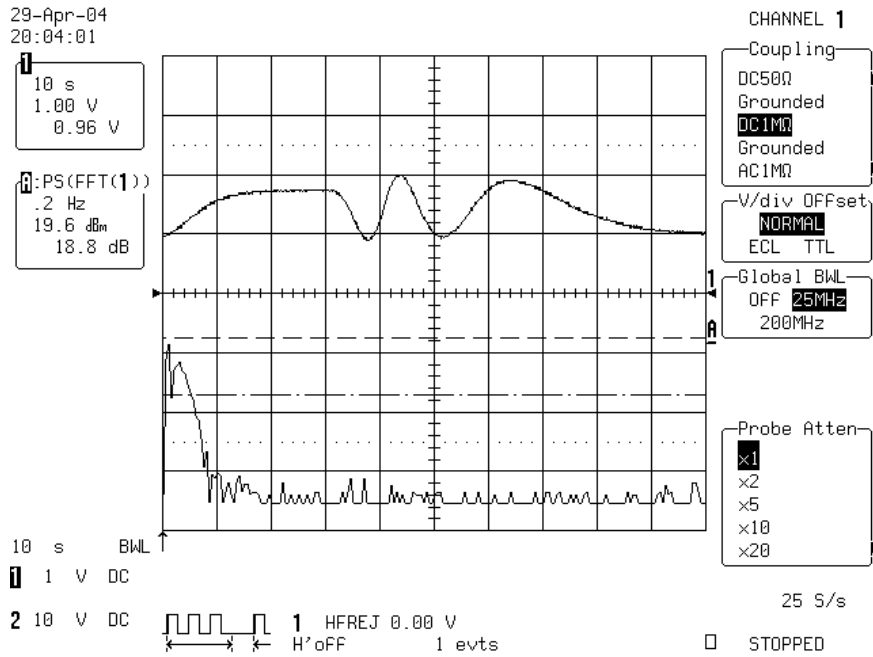


Fig. 6.17 The engine sensor response by Q-point tuning

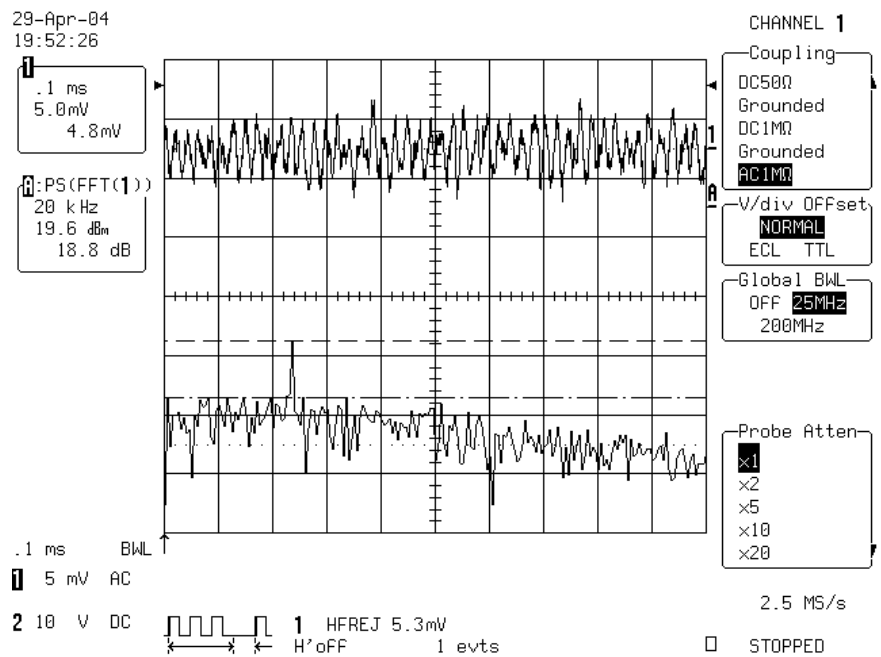


Fig. 6.18 The engine sensor dynamic pressure response (25 °C)

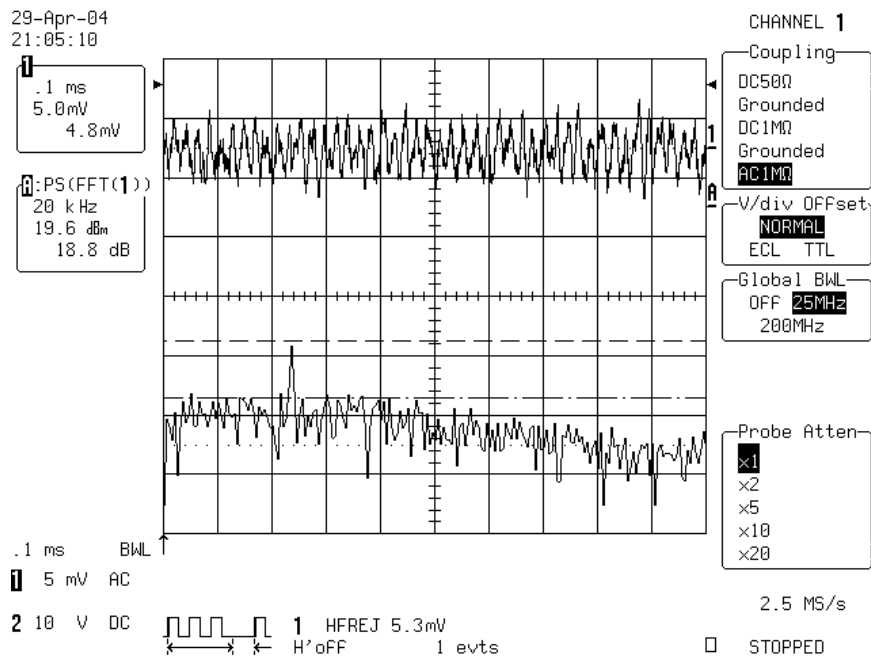


Fig. 6.19 The engine sensor dynamic pressure response (600 °C)

6.3.3 Simulation test

An AC axial fan was used to generate unsteady air pressure and the engine pressure sensor was flush mounted on the fan as shown in Fig. 6.20. The fan has three blades rotating at speed of 2500 revolutions per minute (RPM). The calculated dynamic pressure frequency should be:

$$f_{fan} = 3 \times 2500 / 60 = 125 \text{ (Hz)} \quad (6-9)$$

The sensor output signal was captured by an oscilloscope and displayed as Fig. 6.18. The experiment result is consistent with the theoretical prediction. Since the dynamic pressure is weak, the SNR of the sensor signal is low. However, this simple test not only verified the whole sensor system feasibility but also indicated that the sensor's sensitivity is high enough for detection of dynamic pressure near the fans of a real turbine engine.

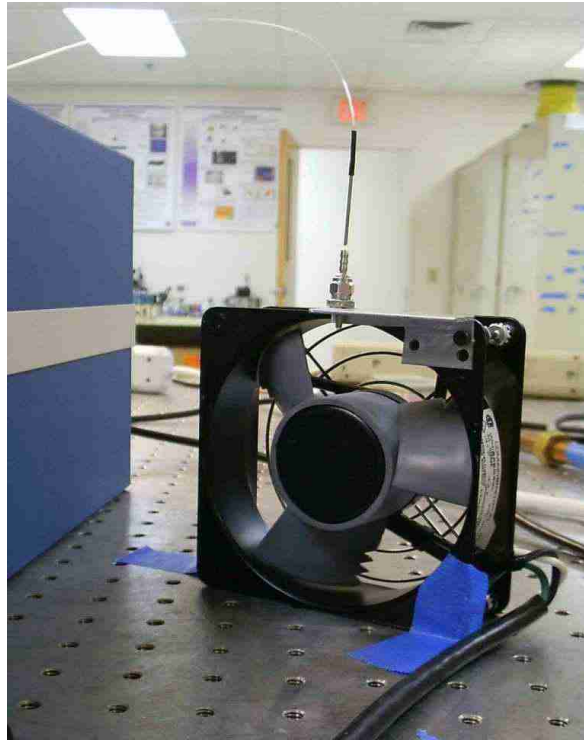


Fig. 6.20 Test sensor's dynamic response near an AC axial fan

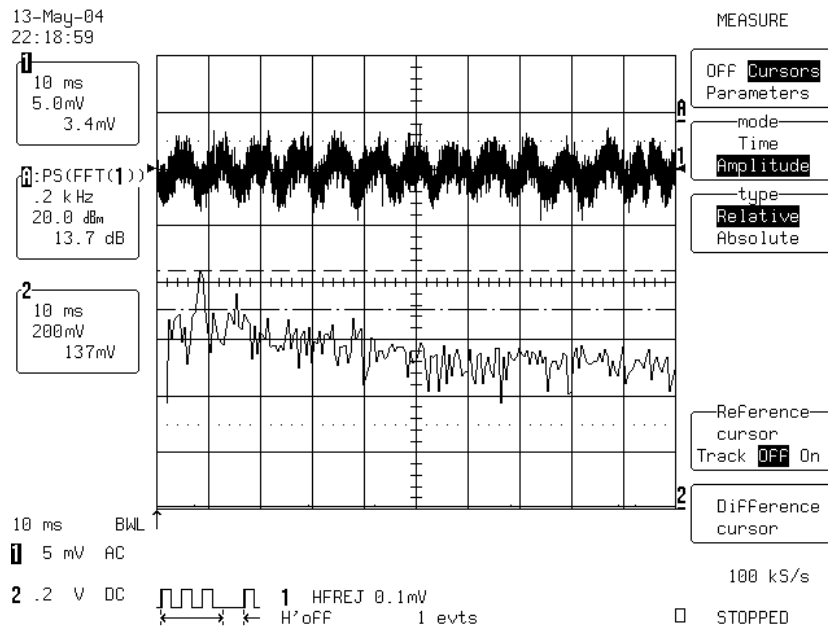


Fig. 6.21 Sensor output of AC axial fan test

6.4 Engine sensor field test

The turbine engine for the sensor field test in Blacksburg, Virginia, U.S., was a F-109 turbofan test engine [79] manufactured by Allied Signal. The fan consists of 30 blades and the pressure sensors were flush mounted on the in-let aluminum ring near the blades (see Fig. 6.23 –Fig. 6.18).

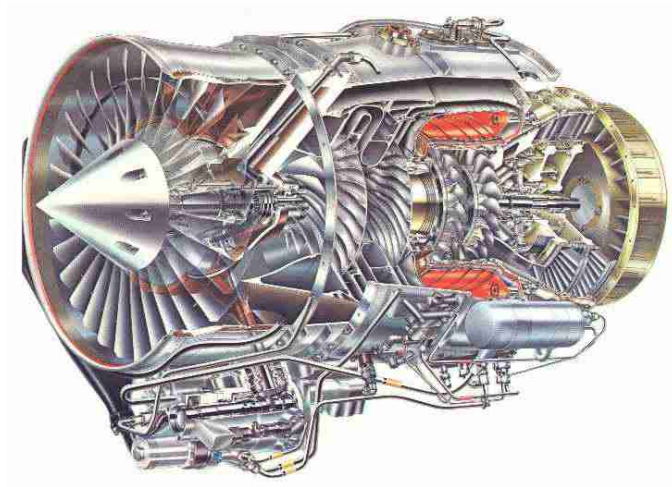


Fig. 6.22 Sketch of F-109 turbofan engine

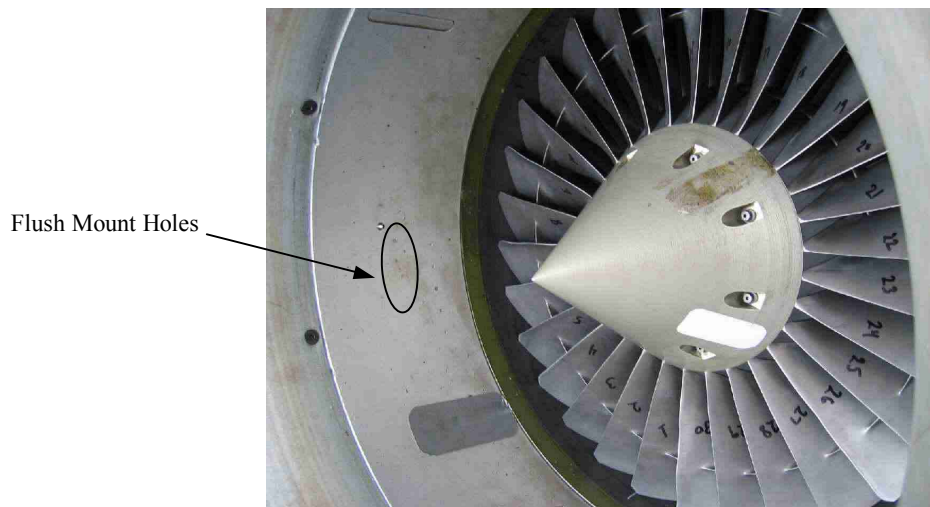


Fig. 6.23 Engine pressure sensor installation

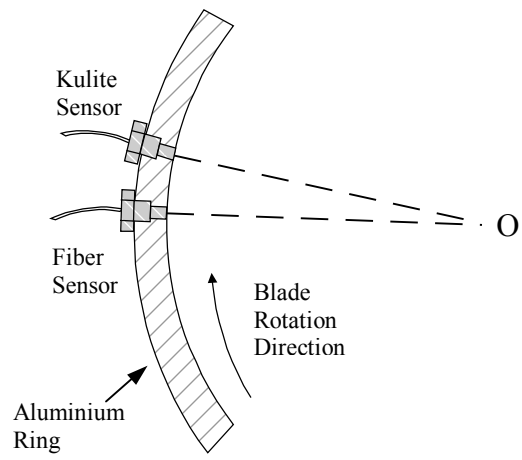


Fig. 6.24 Illustration of the sensor installation.



Fig. 6.25 F-109 turbofan engine



Fig. 6.26 Engine pressure sensor installation (side view)

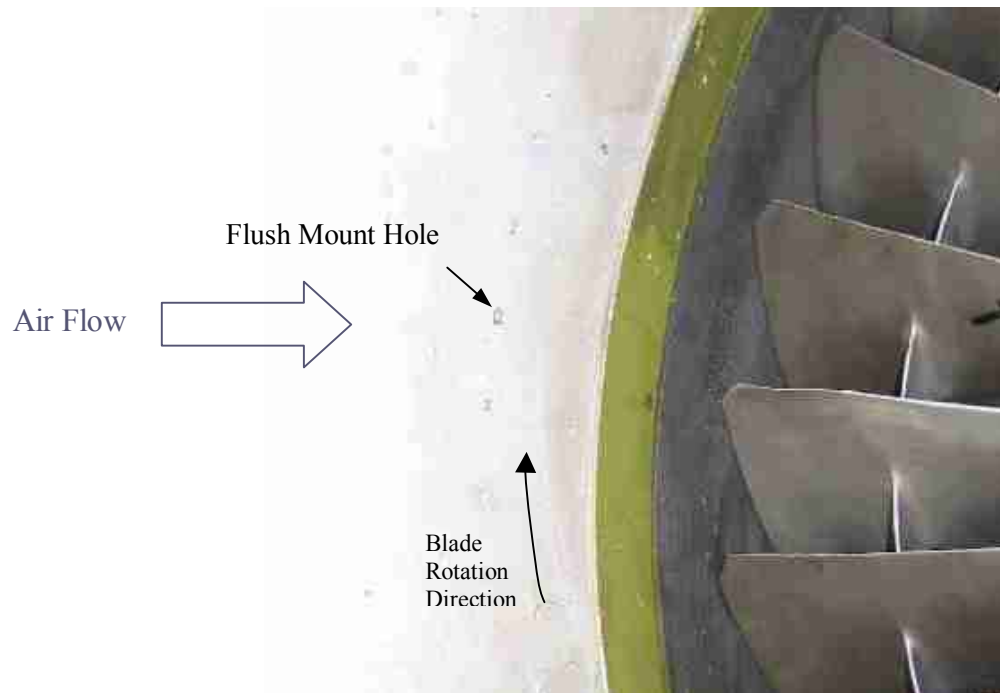


Fig. 6.27 Flush mount holes in the aluminum ring of inlet



Fig. 6.28 Sensor signal processing and data acquisition devices

The time domain and frequency domain signals for the diaphragm-ferrule based sensor and Kulite sensor are shown in Fig. 6.29 and Fig. 6.30 respectively. There was a phase difference (time delay) between the two signals due to the slightly different installation locations. According to the cross-correlation between the two signals, this delay is 0.058 ms. The time domain signals were processed using the Matlab FFT function to obtain the frequency data listed in Table 6.1.

The fundamental frequency at 5.93 kHz is due to the effect of the blades passing since the rotation speed of the fan with 30 blades is set to about 12000rpm. By precise calculation, the actual fan rotation speed is

$$5.93 \times 1000 \text{ Hz} \times 60 \text{ s} / 30 = 11860 (\text{rpm}).$$

According to the Kulite calibration data, the output of the sensor is 33.3 mV/psi. The peak to peak output at 5.93kHz was 22.7544mV, resulting in a dynamic pressure of:

$$P_{kulite} = \frac{22.7544mV}{33.3mV / psi} = 0.683psia .$$

Based on the diaphragm-ferrule fiber sensor calibration data, the sensor output is 87mV/psi. The peak to peak output at 5.93 kHz was 60.1268 mV, resulting in a dynamic pressure of:

$$P_{fiber} = \frac{60.1268mV}{87.0mV / psi} = 0.691psia .$$

This value is close to that of the reference Kulite sensor.

The field test result confirms that the fiber optic sensor design can function safely and reliably near the engine fan. During a field test of about two hours, the optical sensors' package was robust enough for the engine operation. In addition, the optical sensor is able to measure the acoustic pressure near the engine fan. Its performance is consistent with that of the commercial Kulite sensor. Further work will involve testing CPT's engine sensors at hot sections in the engine.

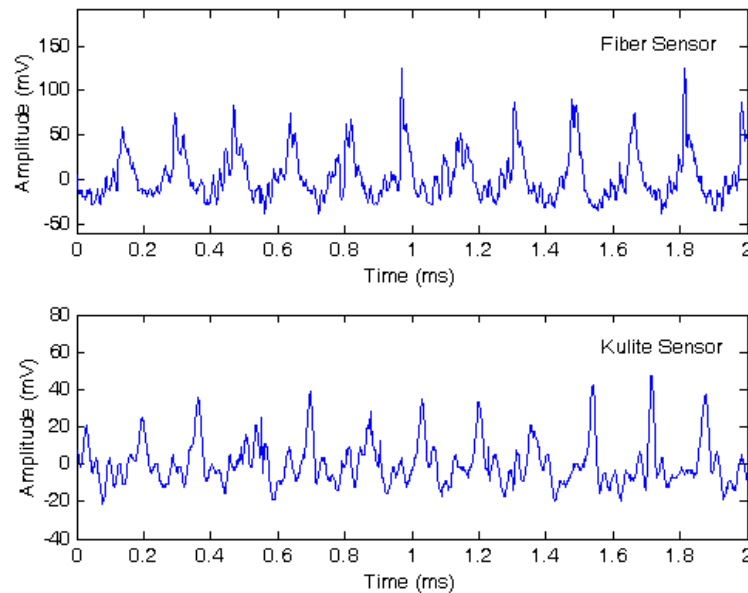


Fig. 6.29 Fiber sensor and Kulite sensor signals in time domain.

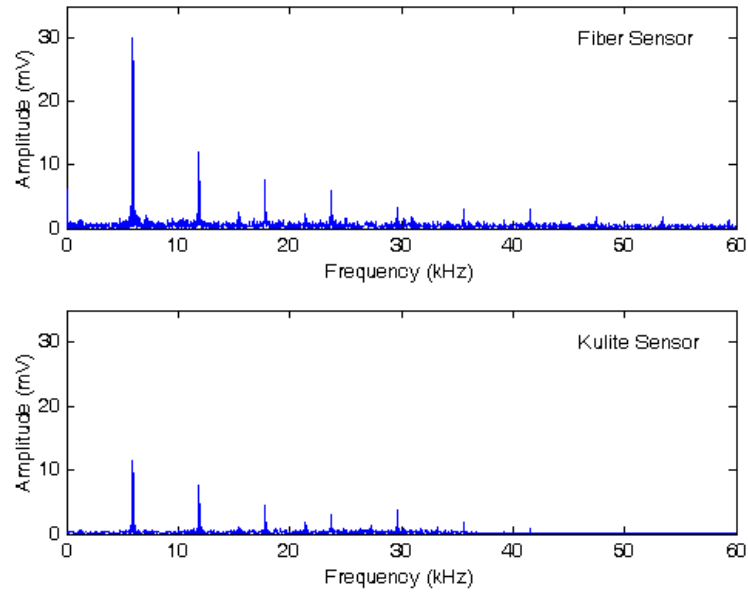


Fig. 6.30 Fiber sensor and Kulite sensor signals in frequency domain.

Table 6.1 Main frequencies measured by Kulite and diaphragm-ferrule based sensors.

	Frequency (KHz)		Amplitude (mV)	
	Diaphragm-Ferrule Sensor	Kulite Sensor	Fiber Sensor	Kulite Sensor
1	5.930	5.930	30.0634	11.3772
2	11.860	11.865	12.1294	7.4924
3	17.795	17.800	7.7381	4.5748
4	23.725	23.720	6.0433	2.9771
5	29.660	29.660	3.2610	3.7025
6	35.590	35.595	2.9957	1.8222

6.5 Engine combustor simulation system

Fig. 6.31 shows the schematic of the dynamic pressure test system. The dynamic pressure (ultrasonic wave) is generated by an ultrasonic air transducer purchased from APC Products, Inc. The transducer is sealed in an iron housing and faces the open end of a ceramic tube connected to the house. The other end of the ceramic tube connects to the pressure control system and the fiber optic sensor system through a T-fitting. All the connections to the housing and the ceramic tube are hermetically sealed by epoxy. The sensor is put into the central part of tube, which is heated by a furnace.

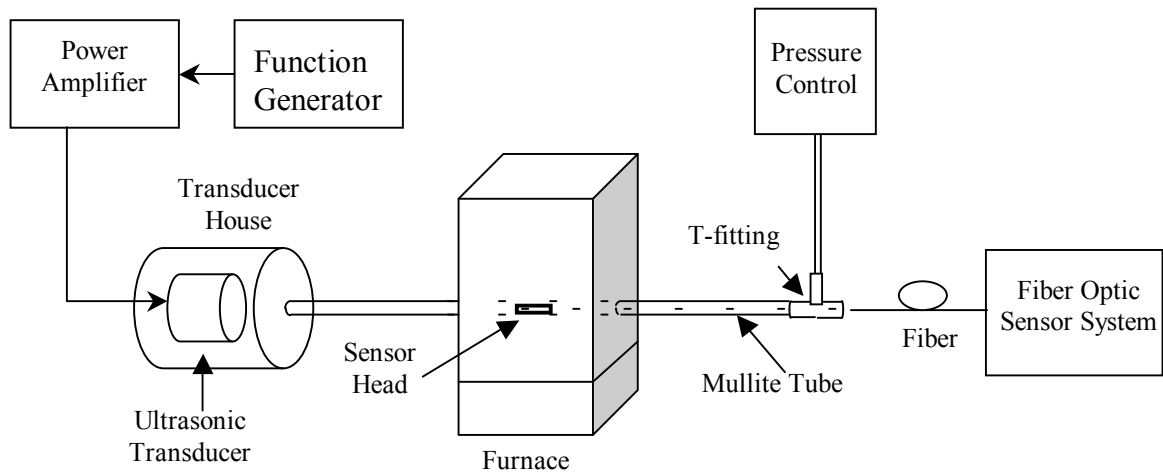


Fig. 6.31 Schematic of the high temperature dynamic pressure test system.

The signal from a function generator is amplified by a high voltage power amplifier (Model 7602, Krohn-Hite Corporation) before inputting to the air transducer. From the manufacturer's test report, at ambient pressure, the transducer can generate a sound pressure level of 140 dB (corresponding to a peak-to-peak pressure change 0.058 psi) at a one meter distance when a 47 kHz sinusoidal wave with 200 volts peak-to-peak is applied. The sound pressure increases as the background pressure is increased due to higher ultrasonic wave to air coupling efficiency at higher background pressure. The real sound pressure levels at the location of sensor and at different background pressures need to be calibrated.

The static background pressure inside the ceramic tube is controlled by the pressure control system (Model 9035, Pressure Systems), which is connected to a compressed nitrogen gas tank. The background pressure can be adjusted accurately from ambient pressure to 200 psi.

The ceramic tube is approximately 1.5 meter long and only the central part where the fiber optic sensor is placed is heated. The temperature in the heated area can be adjusted from room temperature to 1200°C by the furnace. The heated length is about 40 cm. All other units of the test system and the seals are contained in a safe low-temperature environment.

The specifications of our test system are listed here:

- Test temperature: up to 1200 °C;
- Test static background pressure: up to 200 psi;
- Test dynamic pressure: sound pressure more than 140 dB with a frequency of about 47 kHz.

In the preliminary sensor test, we found the sensor's signal is very weak if illuminated by a LED instead of a high power laser and the signal is also very sensitive to the alignment of the sensor in the ceramic tube. Moreover, the inside diameter of the ceramic tube is much smaller than the diameter of the acoustic wave generator, which results in a very poor coupling efficiency. Some considerable improvements of the simulation system are needed in the future.

Chapter 7 Miniature Diaphragm Based Fiber Optic Sensor

This chapter will describe a miniature diaphragm based fiber optic sensor including sensor structure design, sensor fabrication and performance evaluation.

7.1 Miniature sensor structure

Miniature fiber optic sensors attract more attention in applications where restricted space is a consideration, but they are more difficult to fabricate and handle. Moreover, compared with larger ones, they have some unavoidable limitations. First, since the effective diameter of the diaphragm, limited by the fiber itself, is very small, the diaphragm must be very thin to obtain a considerable sensitivity according to the diaphragm deflection model [56] (See Eq. (1)), which is a great challenge in sensor fabrication. Second, the F-P cavity (air-gap) length cannot be easily adjusted in fabrication. Third, they do not have temperature self-compensation capability. Although some microelectromechanical systems (MEMS) pressure sensors [10, 12, 80] with diameters of about a few hundred microns may overcome some of the drawbacks just mentioned, they will encounter high stress due to the coefficient of thermal expansion (CTE) mismatches among the elements made of different materials, which may lead to a failure.

A novel miniature diaphragm based pressure sensor was developed, which offers high sensitivity in combination with miniature size, greatly relaxed restrictions on diaphragm thickness, precise F-P cavity length control and self-temperature compensation capability. The sensor size can be chosen from 200 to 500 μm to meet different application requirements. In addition, the sensor's all-silica structure possesses many advantages including excellent reliability (without CTE mismatches), high temperature capability, corrosion resistance, electromagnetic interference (EMI) immunity and biocompatibility, making it suitable for both industrial and biomedical applications. The sensor structure is shown in Fig. 7.1. The length of the F-P cavity

(air-gap) will decrease with deflection of the diaphragm as a result of the applied pressure. Light is injected into the optical fiber and partially reflected (4%) by the end face of the fiber and the inside surface of the diaphragm. Then the two reflections propagate back through the same fiber and generate interference fringes, which are demodulated to determine the air-gap thickness.

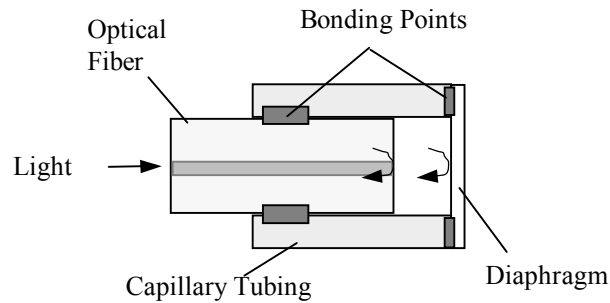


Fig. 7.1 Miniature diaphragm based fiber optic pressure sensor

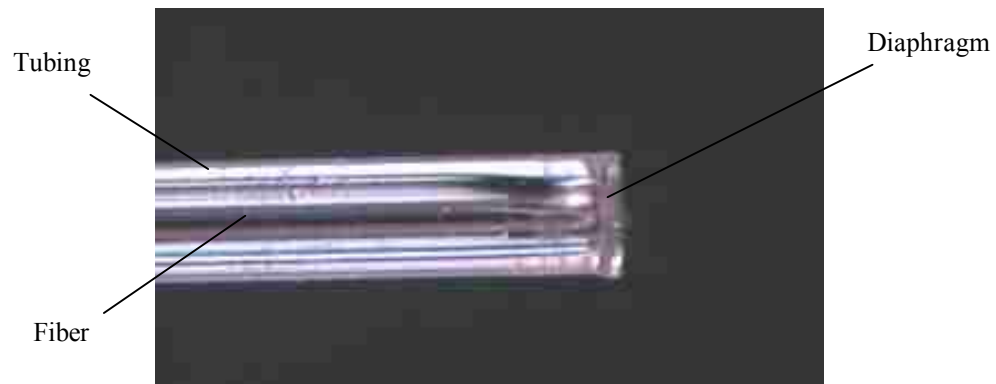


Fig. 7.2 Micrograph of the miniature sensor

7.2 Miniature sensor fabrication

Compared with the sophisticated processes involved in making a conventional MEMS sensor, this sensor fabrication is very simple in that only cleaving, splicing and etching

are required. A piece of silica glass capillary tubing with an inner diameter (I.D.) of 158 μm and an outer diameter (O.D.) of 323 μm was cleaved to obtain a flat end face. A cleaved silica optical fiber with 330 μm O.D. was spliced to the end of the tubing by a fiber fusion splicer (Sumitomo, Type-36) and was cleaved to retain a thin layer about 10-30 μm thick (shown in Fig. 7.3). A cleaved lead-in single mode optical fiber (SMF-28) was inserted into the tubing and a CO₂ laser bonding technique was used to realize a fusion bond. The lead-in fiber can also be a multi-mode fiber (MMF), depending on application requirements. Since the dimensional changes of the fiber and tubing are slightly different during laser fusion, the sensor air-gap can be precisely controlled with a precision of about 3 nm [75]. This feature can provide excellent flexibility in sensor design, fabrication and signal demodulation. For example, in the Self-Calibrated Interferometric-Intensity-Based (SCIIB) sensor system [8], the air-gap must be set in the linear range of a half fringe. In the white light interferometry system, the air-gap should be set so that the sensor can work efficiently in the range having good interference fringes.

Since it is hard to get a cleaved diaphragm thinner than 10 μm , a hydrofluoric acid (HF) etching process was used to reduce the diaphragm thickness down to a few microns. Since the two surfaces of the diaphragm are not very parallel after cleaving and the HF etching will also make the outside surface rough, the reflection from the outside surface can be neglected.

Since the large core ($\geq 200\mu\text{m}$) fiber has a pure fused silica core, the diaphragm will keep flat shape after etching, which will greatly simplify the sensor design and theoretical analysis. According to the deflection model of a rigidly clamped flat diaphragm, the sensor sensitivity is proportional to its radius to the fourth power and inversely proportional to its thickness to the third power.

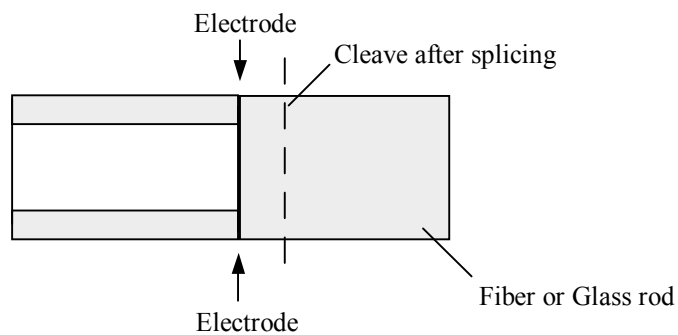


Fig. 7.3 Fabrication of the miniature diaphragm

An optical fiber, which can be single-mode or multimode, is inserted in the tubing and hermetically sealed by a laser as shown in Fig. 7.4. When temperature increases, the tubing expansion and the thermal induced inside air pressure rise will increase the F-P cavity, so choosing fiber with higher CTE than that of the tubing can compensate the sensor temperature dependence.

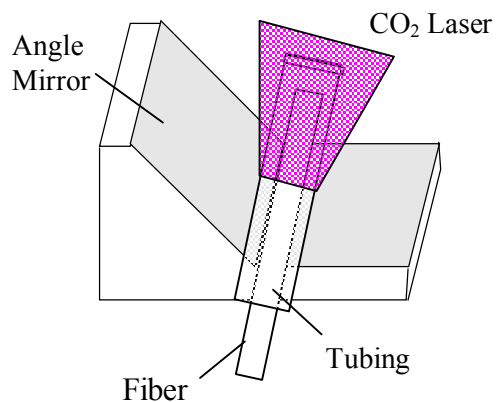


Fig. 7.4 Fiber to tubing bonding

7.3 Performance analysis and testing

Usually, we define the ratio between the deflection and the pressure difference as the diaphragm pressure sensitivity (Y). Since only the diaphragm center deflection is of interest, the sensitivity Y_c (for fused silica material at 25°C) is given by:

$$Y_c = \frac{3(1-\mu^2)}{16Eh^3} = 1.71 \times 10^{-5} \frac{r^4}{h^3} \quad (\text{nm/psi}) \quad (7-1)$$

where r and h are the radius and thickness of the diaphragm in microns respectively. E is the Young's Modulus and μ is the Poisson's Ratio.

Using Eq. (7-1), the analytical prediction of the sensor pressure sensitivity was derived and is shown in Fig. 7.5; the sensor's experimental static pressure response is shown in Fig. 7.6.

The measured sensor pressure sensitivity is about 3.98 nm/psi. Based on the diaphragm initial thickness, HF etching rate and time, the diaphragm final thickness is about 5.5-6 μm , which is consistent with the theoretical calculation. In the experiment, a Component Test System (CTS, MicronOptics, Inc) and a spectrum analysis algorithm [47] was used to calculate the F-P cavity length L as shown in Eq.(7-2).

$$L = \frac{\lambda_1 \lambda_2}{2(\lambda_2 - \lambda_1)} \quad (7-2)$$

where λ_1 λ_2 are the wavelengths of two adjacent valley points in the spectrum

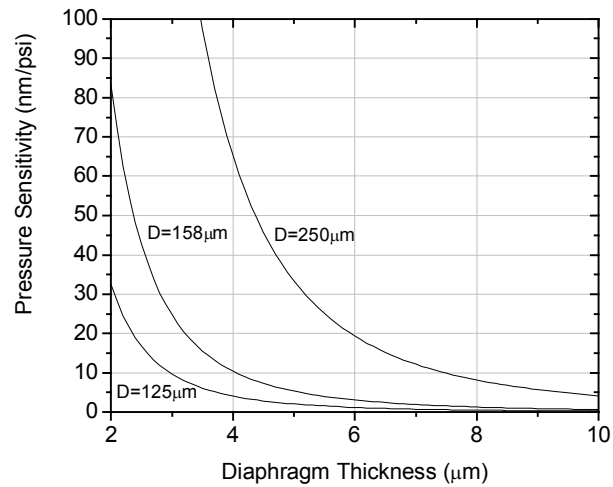


Fig. 7.5 Theoretical pressure sensitivities of the sensor with several diaphragm diameters.

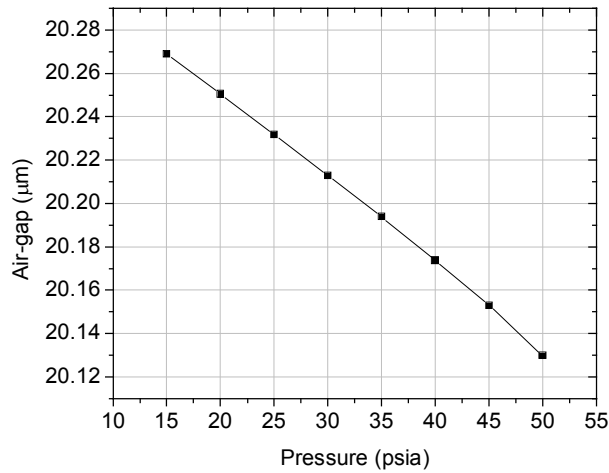


Fig. 7.6 Sensor static pressure response (15-50psi) at room temperature

In addition, the one valley tracking method [47] improves the measurement resolution to be about 1 ppm of the initial air-gap length, or about 0.02 nm [81]. Therefore, the pressure measurement resolution is about 0.005 psi (34.5 Pa or 0.26 mmHg). Additionally, the sensor pressure sensitivity can be exponentially increased by etching the diaphragm down to 2 - 4 μm thick (refer to Fig. 7.5.).

Since the diaphragm has the capability of detecting dynamic pressure, the sensor is also suitable for acoustic applications such as medical imaging and diagnosis. Based

on the properties of fused silica, the lowest natural frequency of the diaphragm can be theoretically calculated as follows and the curves are shown in Fig. 7.7.

$$f_{00} = \frac{\alpha_{00}}{4\pi} \sqrt{\frac{E}{3w(1-\mu^2)}} \left(\frac{h}{r^2} \right) = 2.742 \times 10^9 \frac{h}{r^2} \text{ (Hz)} \quad (7-3)$$

where α_{00} is a constant related to the vibrating modes, which is 10.21 for the lowest natural frequency, w is mass density of the diaphragm and r , h , E and μ are the same as the parameters in Eq. (7-1)

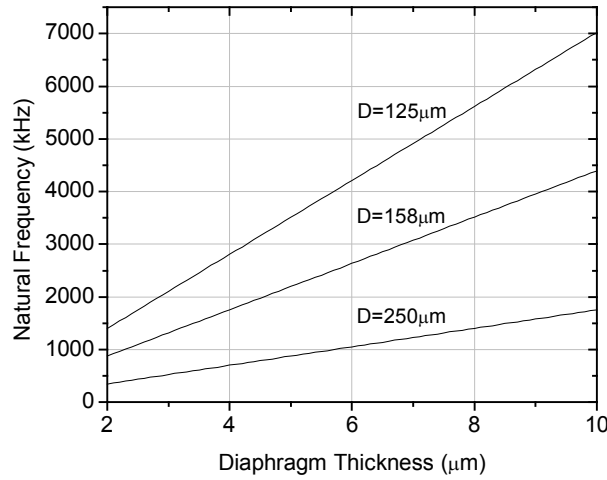


Fig. 7.7 Theoretical natural frequency of the sensor for varying diaphragm diameters.

In order to faithfully respond to dynamic pressures, the sensor's natural resonant frequency should be at least three to five times higher than the highest applied frequency. This sensor, having a natural frequency of about 2.5 MHz according to the calculation, should thus be capable of detecting acoustic waves 500~800 kHz. For specific applications, the sensor can also work near its resonant frequency as a narrow band high sensitivity acoustic sensor.

The sensor was connected to the SCIIB system in an acoustic experiment and the results are shown in Fig. 7.8. The acoustic source generated a 46.9 kHz acoustic wave

with about 0.1 psi dynamic pressure. The sensor output signal showed a frequency of 46.9 kHz, which was consistent with the acoustic source and the signal-to-noise (SNR) of the signal was about 19dB. For applications where the acoustic frequency is roughly known, a narrow band filter and amplifier can be used to considerably improve the system performance.

In addition, this sensor configuration has a passive temperature self-compensation capability because the optical fiber normally has a higher CTE than that of the fused silica tubing due to the germanium doping inside the fiber, whose expansion in the cavity will compensate that of the tubing when temperature is increased. As shown in Fig. 7.9, the sensor's temperature dependence is about 0.083 nm/°C, which will lead to a pressure measurement error of about 0.02 psi/°C. This temperature dependence was partly caused by the inner pressure changes of the trapped air. Since multi-mode fiber (MMF, Corning 50/125) has a higher CTE than SMF-28, by using a MMF lead-in fiber or splicing a short section of MMF to the lead-in SMF, this sensor temperature dependence can be mostly compensated. Since the cladding of the fiber is made of pure fused silica, the bonding between the cladding and the tubing will not introduce thermal expansion stress.

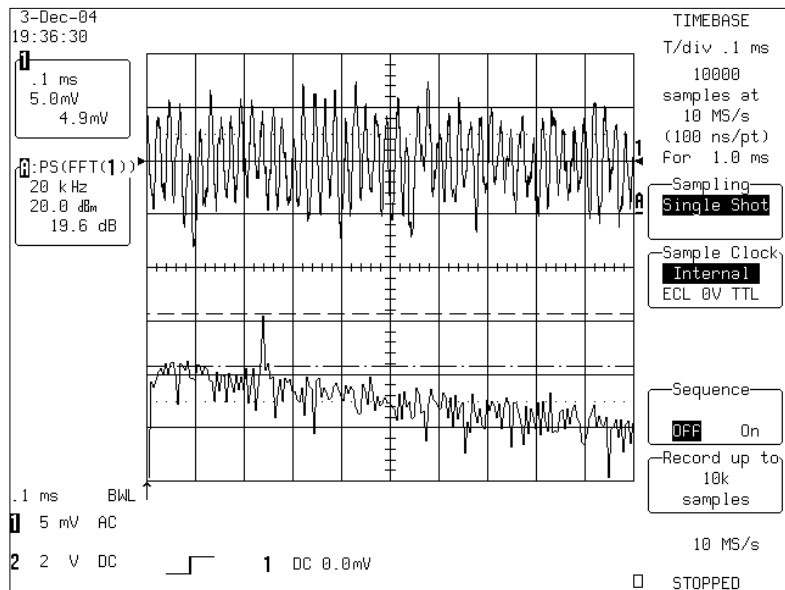


Fig. 7.8 Sensor dynamic pressure (acoustic wave) response at room temperature

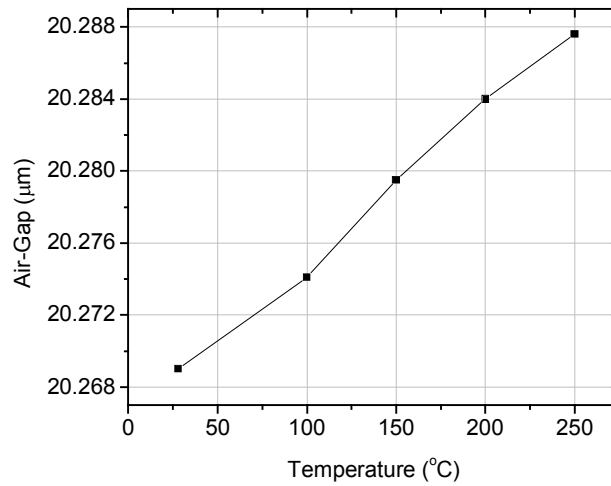


Fig. 7.9 Sensor temperature dependence at room pressure

In addition to the ferrule-diaphragm based sensor, we have described a novel tubing-diaphragm based miniature fiber optic pressure and acoustic sensor, which preserves the advantages of ferrule-based sensors while offering miniature size, which could be attractive in applications where the operating space is restricted, such as biomedical uses. The precisely controlled F-P cavity length allows flexibility in choosing signal demodulation schemes. In addition, the all-silica sensor structure temperature self-compensation capability can operate in a wide temperature range, which is ideal for harsh environment applications.

Chapter 8 Summary and Suggestions for Future Work

This chapter will draw some conclusions in the research, summarize the achievements and give suggestions for future work to improve the sensor and system performance.

8.1 Summary and conclusions

Based on the overview on the state-of-the-art of fiber optic sensors, the current commercially available pressure and acoustic sensors have limitations in temperature capabilities and bandwidth, which are typically lower than 450°C and 20 kHz respectively. However, many industrial or biomedical applications require either higher temperature capabilities or higher bandwidth. For example, pressure measurement in a gas turbine engine may experience temperatures higher than 500°C and the acoustic detection of partial discharge in high voltage transformers requires a bandwidth larger than 100 kHz. These limitations have remained unsurmountable for years. In this research, we developed novel fiber optic pressure sensors with much higher temperature capabilities, higher bandwidth and more flexibility in selection of sensor sizes and interrogation methods.

8.1.1 Sensor modeling and the principle of operation

Among the fiber optic sensing techniques, the Fabry-Perot cavity is one of the simplest optical structures, involving only two optical reflection surfaces. A commercially available polished glass wafer whose surface is adequate for sensor fabrication was used as the diaphragm, saving a great deal of time in parts preparation. The other reflection surface, the fiber end face, can easily be obtained by cleaving.

The theory of fiber optic interferometric fringes is based on the principle of two-beam interference, and is universally applicable to any kind of Fabry-Perot interferometric sensor. The diaphragm configuration was chosen for the pressure sensor construction

after investigation of many other configurations such as tubing based structures because the diaphragm can transfer the applied outside pressure to the deflection with high sensitivity. Also its frequency response is much higher than tubing based sensors. The clamped circular flat diaphragm model has been well investigated, including its mechanical properties such as deflection analysis, natural frequency and stress distribution.

8.1.2 Sensor fabrication

Several novel diaphragm based fiber optic sensors were designed and developed in this research. Sensor fabrication is the most important step in the sensor development, and will determine the sensor performance, survivability and reliability. Thermal fusion bonding techniques were proposed and developed to join the sensor parts hermetically with high mechanical strength. Since the sensors are composed entirely of fused silica, there is no mismatch of CTEs among the sensor parts, which is a common problem in sensor construction. The epoxy-free design allows the sensor to work in environments with temperatures up to the limit of the optical fiber itself, which is typically 700~800°C. In addition, this thermal bonding technique can control the air-gap in the sensor to realize good repeatability in production. Using the white-light system, the sensor's signal can be monitored during the fabrication.

8.1.3 Signal interrogation systems

Two major signal demodulation methods, intensity- and spectrum analysis-based techniques were investigated and used in the sensor systems. The intensity-based technique mentioned here is a hybrid intensity/interferometric method and is not the same as those described in the early fiber optic sensor literature, which has no interferometric component. This technology, called the self-calibrated intensity/interferometric based (SCIIB) method, used a self-calibrating mechanism to eliminate

the error from light source fluctuations. It has high sensitivity and large bandwidth, which is best for high frequency measurement such as acoustic wave detection.

A white-light based interrogation system, which uses a light source with spectral width more than 40nm, was investigated. Multiple or single fringe position trace methods achieved an absolute measurement with both high resolution and large measurement range. In addition, a tunable laser based spectrometer was also investigated and used in the sensor testing. Although the sensor spectrum fringes are generated with a different way, the white-light signal processing techniques are still applicable and obtained very good results.

8.1.4 Sensor testing

Comprehensive experiments were performed to systematically evaluate the performance of the diaphragm sensor and sensing system, including static pressure testing, capability for aerodynamic pressure, temperature dependence, frequency response measurement and high frequency acoustic wave detection. The evaluation of the sensor confirmed that the sensor can work above 600°C without considerable performance degradation.

The behavior of the sensor at elevated temperatures was also investigated. The results indicated that the glass diaphragm has both elastic and viscous properties, which should be considered and is useful in future sensor design and test.

An engine sensor field test was performed with very good results. The field test result confirms that the fiber optic sensor design can function safely and reliably near the engine fan. During the two-hour engine sensor field test, the fiber optic sensors' package was robust enough for the engine operation. In addition, the optical sensor was able to measure the acoustic pressure near the engine fan and its performance was better than that of the commercial Kulite sensor.

8.2 Summary of Contributions

This section outlines the significant contributions of this dissertation and related work as follows:

- Proposed and developed the all-silica diaphragm based fiber optic pressure and acoustic sensors.
- Designed and implemented a novel diaphragm based sensor fabrication method and system, which can be used for other laser bonding purposes.
- Designed and developed a miniature tubing-diaphragm based pressure and acoustic sensor.
- Directed the design and implemented the packaging of engine sensors for the engine sensor field test.
- Directed the design and implementation of sensor testing and calibration system.
- Programmed and implemented the oscilloscope-computer based sensor data acquisition system.
- Directed and organized the field test of engine sensors for dynamic pressure measurements in a gas turbine engine at the Virginia Tech Airport on June 24th 2004.

8.3 Suggestions for Future work

This dissertation work exploits the new areas of research in diaphragm based sensor technology. Suggestions for future work springing from this research are as follows:

- Investigate more techniques for dynamic calibration.
- Investigate the mechanical properties of the diaphragm sensor by finite element methods.

- Minimize the temperature dependence of the pressure sensor.
- Investigate the characteristics and performance achieved by coating metal or dielectric films on diaphragm and fiber end.
- Study the signal processing techniques and improve the sensor system performance
- Improve the turbine engine simulation system for high temperature and high background pressure dynamic testing.
- Investigate the feasibility of using the sensor for other applications, such as hydrophones, acoustic imaging and partial discharge detection.

References

- [1] A. Wang, et al., "Optical fiber pressure sensor based on photoelastic effect and its applications," *Journal of Lightwave Technology*, **10**, pp. 1466-1472, 1992.
- [2] B.C.S. Chou, J.-S. Shic, and Y.-M. Chen. "A Highly Sensitive Pirani Vacuum Gauge," in *Solid-State Sensors and Actuators: Eurosensors IX. Transducers '95. The 8th International Conference*, 1995, 2. 167-170.
- [3] A.A. Ned, et al. "Dynamic pressure measurements using silicon carbide transducers," in *Instrumentation in Aerospace Simulation Facilities, 9th International Congress on ICIASF*, 2001, 240-245.
- [4] B. Qi, et al. "Fiber optical pressure and temperature sensors for oil down hole applications," in *Proceedings of SPIE*, 2002, Vol, 4578. 182-190.
- [5] W.F. Cullinane and R.R. Strange. "Gas Turbine Engine Validation Instrumentation: Measurements, Sensors, and Needs," in *Proc. of SPIE, Harsh Environment Sensors II*, 1999, 3852.
- [6] E. Udd, *Fiber optic sensors: an introduction for engineers and scientists*: John Wiley & Sons, Inc, 1991.
- [7] K.A. Murphy, et al., "Quadrature phase shifted extrinsic Fabry-Perot optical fiber sensors," *Opt. Lett.*, **16**, pp. 273-275, 1991.
- [8] A. Wang, et al., "Self-Calibrated Interferometric-Intensity-Based Optical Fiber Sensors," *J. Lightwave Technol.*, **19**, pp. 1495-1501, 2001.
- [9] J. Deng, et al., "Optical Fiber Sensor-based detection of Partial Discharges in Power Transformers," *Optics and Laser Technology*, **33**, pp. 305-311, 2001.
- [10] M.J. Gander, et al., "Embedded micromachined fiber-optic Fabry-Perot pressure sensors in aerodynamics applications," *IEEE Sensors Journal*, **3**, pp. 102-107, 2003.
- [11] B. Yu, et al., "Fiber Fabry-Perot Sensors for Detection of Partial Discharges in Power Transformers," *Applied Optics*, **42**, pp. 3241-3250, 2003.
- [12] J. Zhou, et al., "Optically Interrogated MEMS Pressure Sensors for Propulsion Applications," *Opt. Eng.*, **40**, pp. 598-604, 2001.
- [13] D.C. Abeysinghe, et al., "Novel MEMS Pressure and Temperature Sensors Fabricated on Optical Fibers," *Journal of Micromechanics and Microengineering*, **12**, pp. 229-135, 2002.
- [14] H. Xiao, *Self-Calibrated Interferometric/Intensity Based Fiber Optic Pressure Sensors*. 2000, Ph.D. Dissertation of Virginia Tech.
- [15] G. Fowles, *Flow, level and pressure measurement in the water industry*: Butterworth-Heinemann Ltd, 1993.
- [16] K. Peterson and e. al. "Silicon fusion bonding for pressure sensors," in *Technical Digests, IEEE Solid-State Sensors and Actuator Workshop, Hilton Head Island, South Carolina, U.S.A*, 1988, 144.
- [17] B. Kloech and e. al, "Study of electrochemical etch-stop for high precision thickness control of silicon membrane," *IEEE Transaction on Electron Devices*, **36**, pp. 663-669, 1989.
- [18] H. Jansen, M. deBoer, and M. Elwenspoek. "The black silion method VI: high aspect ration trench etching for MEMS applications," in *Proceedings of IEEE*

- international Workshop Micro Electro Mechanical Systems*, San Diego, CA, U.S.A, 1996, 250-257.
- [19] C. linder, T. Tschan, and N.F. deRooij. "Deep dry etching techniques as a new IC compatible tool for silicon micromachining," in *Proceeding of Transducers'91*, 1991, 524-527.
- [20] G. Engelmann, et al. "Fabrication of high depth-to-width aspect ratio microstructure," in *MEMS '92, Proceedings. An Investigation of Micro Structures, Sensors, Actuators, Machines and Robot. IEEE*, 1992, 93-98.
- [21] D.R. Sparks, S.C. Chang, and D.S. Eddy. "Application of MEMS Technology in automotive sensors and actuators," in *Proceedings of the 1998 International Symposium on Micromechatronics and Human Science, MHS '98*, 1998, 9-15.
- [22] D.R. Kerr and A.G. Milnes, "Piezoresistance of diffused layers in cubic semiconductors," *Journal of Applied Physics*, **34**, pp. 727-731, 1963.
- [23] C.S. Smith, "Piezoresistance in germanium and silicon," *Physics Reviews*, **94**, pp. 43-49, 1954.
- [24] S. Marco, et al., "High-performance piezoresistive pressure sensors for biomedical applications using very thin structured membranes," *Measurement science and technology*, pp. 1195-1203, Sept. 1996.
- [25] S. Clark and K. Wise, "Pressure sensitivity in anisotropically etched thin-diaphragm pressure sensor," *IEEE Transactions on Electronic Devices*, **ED-26**, pp. 1887-1896, 1979.
- [26] R. Puers, "Capacitive sensors: When and how to use them," *Sensors and Actuators A*, **37-38**, pp. 93-105, 1993.
- [27] W. Kao, M. Bao, and Y. Hong, "A high sensitivity integrated circuit capacitive pressure transducer," *IEEE Transaction on Electronic Devices*, **ED-29**, pp. 48-56, 1983.
- [28] M. Mehregany, et al. "Silicon Carbide MEMS for Harsh Environments," in *Proc. of the IEEE*, Aug. 1998, 86. 1594-1610.
- [29] I. Ayerdi, E. Castano, and a.J.G. A. Garcia-Alonso, "High-temperature ceramic pressure sensor," *Sensors and Actuators A*, **60**, pp. 72-75, 1997.
- [30] J. Xu, et al., "A Novel Temperature-Insensitive Optical Fiber Pressure Sensor For Harsh Environments," *IEEE Photonics Technology Letters*, **17**, pp. 870-872, 2005.
- [31] B.G. Clarke, *Pressuremeters in geotechnical design*: Blackie Academic & Professional, 1995.
- [32] Y.J. Rao and D.A. Jackson, "Prototype fiber optic based pressure probe with built-in temperature compensation with signal recovery by coherence reading," *Applied Optics*, **32**, pp. 1993.
- [33] W.B. Spillman, "Multimode fiber-optic pressure sensor based on the photoelastic effect," *Opt. Lett.*, **7**, pp. 388-390, 1982.
- [34] I.P. Giles, S. McNeill, and B. Culshaw, "A stable remote intensity based fiber sensor," *Journal of physics*, **18**, pp. 1124-1126, 1985.
- [35] A. Arie, B. Lissak, and M. Tur, "Static fiber-Bragg grating strain sensing using frequency-locked lasers," *Journal of Lightwave Technology*, **17**, pp. 1849-1855, 1999.

- [36] M.G. Xu, H. Geiger, and J.P. Dakin, "Fiber grating pressure sensor with enhanced sensitivity using a glass-bubble housing," *Electronics Letters*, **32**, pp. 128-129, 1996.
- [37] D.J. Hill and G.A. Cranch, "Gain in hydrostatic pressure sensitivity of coated fiber Bragg grating," *Electronics Letters*, **35**, pp. 1268-1269, 1999.
- [38] U. Sennhauser, et al. "Reliability of optical fiber bragg grating sensors at elevated temperature," in *Proceedings of 38th Annual 2000 IEEE International Symposium on Reliability Physics*, 2000, 264-269.
- [39] J.W. Berthold, "Historical review of microbend fiber-optic sensors," *Journal of Lightwave Technology*, **13**, pp. 1193-1199, 1995.
- [40] G. HERHANDEZ, *Fabry-Perot Interferometers*: Cambridge University Press, 1986.
- [41] M.B. Ben, *High-finesse/Small Gap Extrinsic Fabry-Perot Interferometer and Applications*: Master Thesis of Virginia Tech, 1995.
- [42] B.P. Samoriski. "Fabry Perot Interferometers Theory," in <http://www.burleigh.com/Pages/opticalTech.htm>, 2000,
- [43] J. Dakin and B. Culshaw, *Optical Fiber Sensors: Principles and Components*: Artech House, Inc, 1988.
- [44] Y.J. Rao, et al., "Development of prototype fibre-based Fizeau pressure sensors with temperature compensation," *J. Lightwave Technol.*, **12**, pp. 1685-1695, 1994.
- [45] M.I. Belovlov, M.M. Bubnov, and S.L. Semjonov. "High Sensitive Fiber Interferometric Pressure Sensor," in *Lasers and Electro-optics Europe*, 1996, 192.
- [46] F.L. Pedrotti and L.S. Pedrotti, *Introduction to Optics*: Englewood Cliffs, NJ, Prentice-Hall, 1987.
- [47] B. Qi, et al., "Novel data processing techniques for dispersive white light interferometer," *Opt. Eng.*, **42**, pp. 3165-3171, 2003.
- [48] J.C. Hartl and et al. "Fiber optic temperature sensor using spectral modulation," in *Proc. of SPIE*, 1988, vol. 838. 257-261.
- [49] C.E. Lee and e. al, "Performance of a fiber optic temperature sensor for -200 to 1050°C," *Opt. lett.*, **13**, pp. 1038-1040, 1988.
- [50] Bhatia and e. al, "Recent developments in optical-fiber-based extrinsic Fabry-Perot interferometric strain sensing technology," *Smart materials and structures*, **4**, pp. 246-251, 1995.
- [51] R.O. Claus and e. al, "Extrinsic Fabry-Perot sensor for strain and crack opening displacement measurements for -200 to 900°C," *Smart material and structure*, pp. 237-242, 1992.
- [52] M.A. Chan and e. al, "A micromachined pressure sensor with fiber optic interferometric readout," *Sensors and Actuators, A*, **43**, pp. 196-201, 1994.
- [53] T.Y. Liu, M. Berwick, and D.A. Jackson, *Rev. Sci. Instrum*, **63**, pp. 2164, 1992.
- [54] J.X. Fang and e. al, "Fiber-optic Fabry-Perot flow sensor," *Microwave and optical technology letters*, **18**, pp. 209-211, 1998.
- [55] S. Webster, et al., "Passive signal-processing technique for Monomode fiber optic vortex shedding flowmeters," *Measurement Science and Technology*, **2**, pp. 223-228, 1991.

- [56] M. Di Giovanni, *Flat and corrugated diaphragm design handbook*. New York: M. Dekker, 1982.
- [57] J. Xu, et al. "Epoxy-free high temperature fiber optic pressure sensors for gas turbine engine applications," in *Proceedings of SPIE, Sensor for Harsh Environments*, Oct. 2004, vol. 5590. 1-10.
- [58] S. Temoshenko, *Vibration Problems in Engineering*. Vol. New York: John Wiley & Son, 1974.
- [59] J. Deng, *Development of Novel Optical Fiber Interferometric Sensors with High Sensitivity for Acoustic Emission Detection*: Ph.D. Dissertation of Virginia Tech, 2004.
- [60] R.G. Fneser, "A Review of Solder Glasses," *Electro-Component Science and Technology*, **2**, pp. 1975.
- [61] D.W.A. Forbes, "Solder Glass Seals in Semiconductor Packaging," *Glass Technology*, **8**, pp. 1967.
- [62] T.H. Ramsey. "Thermal and X-Ray Analysis of Some Electronic Package Sealing Glasses," in *American Ceramic Society Bulletin*, 1971, 50.
- [63] C.E. Lee and e. al, "Performance of a fiber optic temperature sensor for -200 to 1050°C," *Opt. lett*, **13**, pp. 1038-1040, 1988.
- [64] McLellan and Shand, *Glass Engineering Handbook*. Third Edition ed., New York: McGraw Hill, 1984.
- [65] A.D. McLachlan and F.P. Meyer, "Temperature dependence of the extinction coefficient of fused silica for CO₂ laser wavelengths," *Applied Optics*, **26**, pp. 1728-1731, 1987.
- [66] T. Li, "Optical fiber communications," *Fiber Fabrication*, **1**, pp. 1985.
- [67] M. Esashi, et al. "Vacuum-sealed silicon micromachined pressure sensors," in *Proceedings of the IEEE*, 1998, 86. 1627-1639.
- [68] K. Totsu, Y. Haga, and M. Esashi. "Vacuum sealed ultra miniature fiber-optic pressure sensor using white light interferometry," in *Transducers, Solid-State Sensors, Actuators and Microsystems, 12th International Conference*, 2003, 1. 931-934.
- [69] M. Hart, D.G. Vass, and M.L. Begbie, "Fast surface profiling by spectral analysis of white-light interferograms with Fourier transform spectroscopy," *Appl. Opt.*, **37**, pp. 1764-1769, 1998.
- [70] U. Schnell, R. Dañdliker, and S. Gray, "Dispersive white-light interferometry for absolute distance measurement with dielectric multilayer systems on target," *Opt. Lett*, **21**, pp. 528-530, 1996.
- [71] J. Schwider and L. Zhou, "Dispersive interferometric profilometer," *Opt. Lett*, **19**, pp. 995-997, 1994.
- [72] M. Hart, D.G. Vass, and M.L. Begbie, "Fast surface profiling by spectral analysis of white-light interferograms with Fourier transform spectroscopy," *Appl. Opt.*, **37**, pp. 1764-1769, 1998.
- [73] H. Xiao, *Self-Calibrated Interferometric/Intensity-Based Fiber Optic Pressure Sensors*, in *Ph.D. Dissertation of Virginia Tech*. 2000.
- [74] B. Rawat, et al., "Optical fiber sensor for variable pressure measurement with temperature compensation," *Lasers and Electro-Optics Society (LEOS)*, **1**, pp. 65-66, 1996.

- [75] J. Xu, et al. "Precise Cavity Length Control in Fiber Optic Extrinsic Fabry-Perot Interferometers," in *Conference on Lasers and Electro-Optics (CLEO)*, Baltimore, MD, 2005,
- [76] W.F. Hosford, *Mechanical behavior of materials*. New York: Cambridge University Press, 2005.
- [77] H. Kobayashi, T. Leger, and J.M. Wolff, "Experimental and theoretical frequency response of pressure transducers for high speed turbomachinery," Int. J. Turbo and Jet Engines, **AIAA Paper**, pp. 98-3745,
- [78] B. Yu, et al., "Tunable-optical-filter-based white-light interferometry for sensing," *Opt. Lett*, **30**, pp. 1452-1454, 2005.
- [79] "http://atlas.usafa.af.mil/dfan/research_centers/aero_research_center/facilities/fl09.htm,"
- [80] D.C. Abeysinghe, et al., "A Novel MEMS Pressure Sensor Fabricated on an Optical Fiber," *IEEE Photon. Technol. Lett*, **13**, pp. 993-995, 2001.
- [81] F. Shen, et al. "UV-induced intrinsic Fabry-Perot interferometric fiber sensors," in *Proc. SPIE*, Philadelphia, PA, 2004, vol. 5590. 47-56.

List of Related Publications, Patents, and Presentations

- **Journals**

1. **J. Xu**, X. Wang, K. L Cooper, G. R. Pickrell and A. Wang, "Miniature temperature-insensitive fiber optic pressure sensor," *IEEE Photonics Technology Letters*. (accepted).
2. **J. Xu**, X. Wang, K. L Cooper and A. Wang, "Miniature All-Silica Fiber Optic Pressure and Acoustic Sensors," *Optics Letters*, vol. 30. No. 24. 2005.
3. **J. Xu**, G. R. Pickrell, X. Wang, W. Peng, K. L Cooper and A. Wang, "A Novel Temperature-Insensitive Optical Fiber Pressure Sensor For Harsh Environments," *IEEE Photonics Technology Letters*, vol.17, pp.870-872, 2005.
4. X. Wang, **J. Xu**, Y. Zhu, K. L Cooper, and A. Wang, "An all fused silica miniature optical fiber tip pressure sensor," *Optics Letters* (in press).
5. F. Shen, **J. Xu** and A. Wang, "Frequency Response Measurement of Diaphragm-Based Optical Fiber Fabry-Perot Interferometric Pressure Sensor By Using Radiation Pressure of an Excimer Laser Pulse," *Optics Letters*, vol. 30, pp. 1935-1937, 2005.
6. B. Yu, A. Wang, G. Pickrell, **J. Xu**, "Tunable-optical-filter-based white-light interferometry for sensing," *Optics Letters*, Vol. 30, pp. 1452-1454, 2005.
7. B. Qi, G. R. Pickrell, **J. Xu**, P. Zhang, Y. Duan, W. Peng, Z. Huang, W. Huo, H. Xiao, R. G. May, and A. Wang, "Novel data processing techniques for dispersive white light interferometer," *Opt. Eng.*, vol. 42, pp. 3165-3171, Nov. 2003.
8. Z. Huang, W. Peng, **J. Xu**, G. R. Pickrell, and A. Wang, "Fiber temperature sensor for high-pressure environment," *Opt. Eng.* Vol. 44, 104401, 2005.
9. W. Peng, G. R. Pickrell, Z. Huang, **J. Xu**, D. W. Kim, B. Qi, A. Wang, "Self-Compensating Fiber Optic Flow Sensor System and its Field Applications," *Applied. Optics*. Vol. 43, pp. 1752-1760, 2004.
10. M. Han, X. Wang, **J. Xu**, K. L. Cooper, and A. Wang, "Diaphragm-based extrinsic Fabry-Perot interferometric optical fiber sensor for acoustic wave detection under high background pressure," *Opt. Eng.*, vol. 44, 060506, 2005.

- **Conferences**

11. **J. Xu**, G. R. Pickrell, K. L Cooper, P. Zhang, and A. Wang, "Precise Cavity Length Control in Fiber Optic Extrinsic Fabry-Perot Interferometers," Conference on Lasers and Electro-Optics (CLEO), Baltimore, MD, May, 2005.
12. **J. Xu**, G. R. Pickrell, X. Wang, B. Yu, K. L Cooper, A. Wang, "Vacuum-sealed high temperature high bandwidth fiber optic pressure and acoustic sensors," Proceedings of SPIE, vol. 5998, Optics East, Boston, MA, Oct. 2005.
13. **J. Xu**, G. R. Pickrell, K. L Cooper, X. Wang and A. Wang, "High-temperature thermometer with fiber optic readout," Proceedings of SPIE, vol. 5998, Optics East, Boston, MA, Oct. 2005.
14. **J. Xu**, X. Wang, K. L Cooper, G. R. Pickrell and A. Wang, "Miniature fiber optic pressure and temperature sensors," Proceedings of SPIE, vol. 6004, Optics East, Boston, MA, Oct. 2005.
15. **J. Xu**, G. R. Pickrell, B. Yu, M. Han, Y. Zhu, X. Wang, K. L Cooper, A. Wang, "Epoxy-free high temperature fiber optic pressure sensors for gas turbine engine applications," Proceedings of SPIE, vol. 5590, pp. 1-10, Optics East, Philadelphia, PA Oct. 2004.
16. **J. Xu**, G. R. Pickrell, Z. Huang, B. Qi, P. Zhang, Y. Duan, and A. Wang, "Double-Tubing Encapsulated Fiber Optic Temperature Sensor," 8th Temperature Symposium, Chicago, Illinois, Oct. 2002. AIP Conference Proceedings, vol. 684(1), pp. 1021-1026. Sept. 2003.
17. Z. Huang, G. R. Pickrell, **J. Xu**, Y. Wang, Y. Zhang, A. Wang, "Sapphire temperature sensor coal gasifier field test," Proceedings of SPIE, Optics East Oct. 2004.
18. X. Wang, **J. Xu**, Y. Zhu, B. Yu, M. Han, K. L. Cooper, G. R. Pickrell, A. Wang, A. Ringshia, and W. Ng, "Verifying an all fused silica miniature optical fiber tip pressure sensor performance with turbine engine field test," Proceedings of SPIE, vol. 5998, Optics East, Oct. 2005.
19. X. Wang, **J. Xu**, B. Yu, K. L. Cooper, and A. Wang, "Implementation of nondestructive Young's modulus measurement by miniature optical sensors," Proceedings of SPIE, vol. 5998, Optics East, Boston, MA, Oct. 2005.
20. Y. Zhu, G. Pickrell, X. Wang, **J. Xu**, B. Yu, M. Han, K. L. Cooper, A. Wang, A. Ringshia, and W. Ng, "Miniature fiber optic pressure sensor for turbine engines," Proceedings of SPIE, vol. 5590, pp. 11-19, Optics East, Philadelphia, PA Oct. 2004.

21. W. Peng, G. R. Pickrell, **J. Xu**, Z. Huang, D. Kim, and A. Wang, “Novel single-phase fiber optic flow sensor system,” Proceedings of SPIE vol. 5272, pp. 223-229 Mar. 2004.

Patents and Disclosures

1. **J. Xu** and A. Wang, “Optical Fiber Pressure Sensors For Harsh Environments”, VTIP Intellectual Property Disclosure No. 03-032, Filed Feb. 2003. US Patent application no. 10/791,842. (Patent Pending)
2. **J. Xu** and A. Wang, “Novel Mini-size Optical Fiber Fabry-Perot Sensors”, Virginia Tech Intellectual Property (VTIP) Disclosure No. 03-126, Filed Sept. 2003.
3. **J. Xu** and A. Wang, “A Novel Optical Fiber and Ferrule Hermetic Thermal Bonding Method”, Virginia Tech Intellectual Property (VTIP) Disclosure No. 03-148, Filed Dec. 2003.
4. X. Wang, **J. Xu**, Y. Zhu and A. Wang, “Miniature Fabry-Perot Structure”, Virginia Tech Intellectual Property (VTIP) Disclosure No. 04-001a, Filed Jan. 2004. (Patent Pending)
5. **J. Xu**, X. Wang and A. Wang, “Miniature Multiplex Fabry-Perot Structure”, Virginia Tech Intellectual Property (VTIP) Disclosure No. 04-001b, Filed January 2004.
6. **J. Xu** and A. Wang, “A Novel Temperature Transducer for Harsh Environments”, VTIP Intellectual Property Disclosure No. 04-010, Filed Jan. 2004.
7. **J. Xu**, X. Wang and A. Wang, “A Novel Miniature High Sensitive Fiber Optic Pressure Sensor”, Virginia Tech Intellectual Property (VTIP) Disclosure No. 04-093, Filed Sept. 2004.
8. X. Wang, **J. Xu** and A. Wang, “Novel Open Miniature Fabry-Perot Structures” Virginia Tech Intellectual Property (VTIP) Disclosure No. 05-010, Filed Feb. 2005.
9. **J. Xu** and A. Wang, “Vacuum-Sealed Miniature Optical Fiber Pressure and Acoustic Sensors”, Virginia Tech Intellectual Property (VTIP) Disclosure No. 05-041, Filed May 2005.
10. X. Wang, J. Xu and A. Wang, “Miniature Fabry-Perot structure with a micrometric tip” Virginia Tech Intellectual Property (VTIP), Filed Sept. 2005.

Presentations

“Testing of Fiber Optics Pressure Sensors in Aircraft Engines,” in CTPR conference, Blacksburg, Virginia, Oct. 19, 2004.

“Fiber Optic Pressure Sensors For Harsh Environments,” in the 51st ISA International Instrumentation Symposium, May 11, 2005.

Appendix: Visual Basic Programs for High Speed Sensor Data Acquisition

```
Private Sub Command1_Click()  
    ActiveDSO1.RefreshImage  
End Sub
```

```
Private Sub Command2_Click()  
    Dim blocks As Long
```

```
    ' Dim waveform  
    ' Dim NumSamples  
    ' Dim i As Long  
    ' Dim lfl As Long  
    ' Dim aFilename As String  
    ' Dim Amplitude As Integer  
    ' Dim fnum As Integer
```

```
    If Command2.Caption = "StopLogging" Then  
        Command2.Caption = "StartLogging"  
        Command3.Enabled = True  
        Timer1.Enabled = False  
        Label2.Caption = "Ready"
```

```
        Exit Sub  
    End If  
    If Command2.Caption = "StartLogging" Then  
        Command2.Caption = "StopLogging"  
        Command3.Enabled = False  
        Label2.Caption = "Start Logging"
```

```
        Timer1.Enabled = True
```

```
        blocks = 0
```

```
        Timer1_Timer  
        blocks = blocks + 1  
        Debug.Print NumSamples, blocks
```

```
    ' ActiveDSO1.SetupWaveformTransfer 0, 0, 0  
    '  
    ' aFilename = Format(Date, "yymmdd") + Format(Time, "hhmmss")  
    '  
    ' fnum = FreeFile
```

```

'   Open aFilename For Binary Access Read Write As #fnum
'   lfl = FileLen(aFilename)
'   Seek fnum, lfl + 1
'
'   Label2.Caption = "Logging to" + aFilename + "..."
'   Do
'       DoEvents
'       If Command2.Caption = "StartLogging" Then
'           Exit Do
'       End If
'       waveform = ActiveDSO1.GetIntegerWaveform("C1", 10000, 0)
'
'       ' Determine the number of samples read
'       NumSamples = UBound(waveform)
'       blocks = blocks + 1
'       Debug.Print NumSamples, blocks
'
'       For i = 0 To NumSamples
'           Amplitude = waveform(i)
'           Put #fnum, , Amplitude
'       Next i
'       ActiveDSO1.RefreshImage
'   Loop While True
'   Close #fnum
'   Label2.Caption = "Ready"
End Sub

Private Sub Command3_Click()
    ActiveDSO1.Disconnect

    Timer1.Enabled = False
    Unload Me
End Sub

Private Sub Form_Load()
    ActiveDSO1.MakeConnection ("GPIB: 5")
    ActiveDSO1.SetRemoteLocal 1

'   ActiveDSO1.WriteString "*RST", 1
'   ActiveDSO1.WriteString "MSIZ 100000", 1
'   ActiveDSO1.WriteString "TRMD NORM", 1
'   ActiveDSO1.WriteString "TDIV 1ms", 1
'   ActiveDSO1.WriteString "C1:VDIV 50mV", 1
'   ActiveDSO1.WriteString "C1:OFFSET 0mV", 1

```

```
ActiveDSO1.RefreshImage  
End Sub
```

```
Private Sub Timer1_Timer()  
    Dim waveform  
    Dim NumSamples  
    Dim i As Long  
    Dim blocks As Long  
    Dim lfl As Long  
    Dim aFilename As String  
    Dim Amplitude As Integer  
    Dim fnum As Integer  
  
    ActiveDSO1.SetupWaveformTransfer 0, 0, 0  
    aFilename = Format(Date, "yymmdd") + Format(Time, "hhmmss") + ".dat"  
  
    fnum = FreeFile  
    Open aFilename For Binary Access Read Write As #fnum  
    lfl = FileLen(aFilename)  
    Seek fnum, lfl + 1  
  
    Label2.Caption = "Logging to " + aFilename + "..."  
  
    waveform = ActiveDSO1.GetIntegerWaveform("C1", 100000, 0)  
  
    ' Determine the number of samples read  
    NumSamples = UBound(waveform)  
  
    For i = 0 To NumSamples  
        Amplitude = waveform(i)  
        Put #fnum, , Amplitude  
    Next i  
    ActiveDSO1.RefreshImage  
    Close #fnum  
  
End Sub
```

Vita

Juncheng Xu was born in Beijing, China, in 1975. He received his B.S. degree in Precision Instrument Engineering and M.S. degree in Optical Engineering from Tsinghua University, Beijing, China, in 1998 and 2000, respectively. He expects to obtain his Ph.D. degree in Electrical Engineering from Virginia Polytechnic Institute and State University (Virginia Tech) in Spring 2006.

From 1997 to 2000, he was with the National Key Laboratory on Precision Measurement Technology and Instruments, Tsinghua University, China, where his research scope covered image processing, laser interferometry and optical sensors. At Virginia Tech, his research was focus on fiber optic, optical and MOEMS sensors.

He is the author or coauthor of 27 journal and conference papers. He is also the inventor or co-inventor of more than 12 patent or patent disclosures.

He was the key researcher in developing oil well pressure and temperature sensors, which have been proven in field tests in California and won the 2004 R&D 100 Award. He was the leading researcher in turbine engine sensor project and the engine sensor was successfully tested in a F-109 turbofan engine in 2004.

He is a member of the IEEE and OSA.